Lehrstuhl E15

Univ.-Prof. Dr. F. von Feilitzsch

Institut für Astro-Teilchenphysik

der Technischen Universität München

Development of a New Composite
Cryogenic Detection Concept for a
Radiochemical Solar Neutrino Experiment

Jean-Côme Lanfranchi

Vollständiger Abdruck der von der Fakultät für Physik der Technischen Universität München zur Erlangung des akademischen Grades eines

Doktors der Naturwissenschaften

genehmigten Dissertation.

<div>

Vorsitzender: Univ.- Prof. Dr. P. Ring

Prüfer der Dissertation: 1. Univ.- Prof. Dr. F. von Feilitzsch

                            2. Univ.- Prof. Dr. P. Böni

</div>

Die Dissertation wurde am 22.09.2005 bei der Technischen Universität München eingereicht und durch die Fakultät für Physik am 5.10.2005 angenommen.

Abstract

Experimental as well as theoretical research concerning neutrino properties have experienced a tremendous boost in the last few years leading eventually to a revision of the standard model of particle physics. A brief historical sketch, as well as the latest results concerning solar neutrino physics followed by an outlook on future experimental tasks are given in chapter 1.

The fundamental energy production mechanism inside the sun, where each nuclear fusion of 4 protons into helium produces an energy of 26.73MeV, can occur via several sub-cycles, the pp, ^{7}Be, pep, ^{8}B, hep and CNO cycle (Bethe-Weizsäcker-cycle). Radiochemical gallium experiments are especially attractive since they provide information on the low-energy and predominant part of the solar neutrino spectrum, the pp-neutrinos. At the beginning of the 1990s two gallium detectors each operated by an international collaboration, started solar neutrino data taking: GALLEX in Gran Sasso, Italy, later in 1998 to become **GNO**, the **G**allium **N**eutrino **O**bservatory and **SAGE**, the **S**oviet **A**merican **G**allium **E**xperiment in Bhaksan, Russia. For more than 12 years these two detectors have been monitoring the solar core, confirming both the presence of pp-neutrinos and an important lack in the measured neutrino interaction rate on earth, as we know now, due to the oscillatory behaviour of neutrinos. Radiochemical gallium detectors are the only solar neutrino experiments so far that can give an upper limit for the contributions by the CNO-cycle to the total energy production in the sun. The latest results from GALLEX/GNO are presented in chapter 2.

In the past few years low-temperature detectors have become a state of the art detection technique in many different fields of physics and especially astrophysics. A considerable amount of work has been invested at our institute into the development of highly-efficient cryogenic detectors, designed to suppress statistical as well as systematic error contributions in a gallium experiment like GNO. A description of the basics of cryogenic detectors using superconducting phase transition thermometers, so-called transition edge sensors (TESs), is given in chapter 3.

The fabrication and processing of a TES based on iridium-gold bilayers, as well as the construction steps of the complete cryogenic detector are described in chapter 4. In order to gain further knowledge on various possibilities to produce superconducting/non-superconducting bilayers for a great variety of applications and to ensure the production of reproducible high-quality low-temperature detectors, a new magnetron sputtering system has been set up and is described in this chapter, too.

In order to achieve a high detection efficiency, i.e. close to 100%, the cryogenic detector

has to exhibit a full absorption in 4π solid angle, a feature realized by using two individual detectors placed on top of each other. As outlined in chapter 5, both detectors consist of a 10 x 20 x 1 mm^3 sapphire substrate with a 1 x 3 mm^2 iridium-gold bilayer serving as a superconducting phase transition thermometer (TES). However, the high temperatures ($\sim$400°C for 3-4h) necessary to deposit germanium onto the sapphire substrate, see next paragraph, cause destruction of the TES bilayer. To overcome this problem, the Ge-deposition and the fabrication process of the TES had to be decoupled, which can be realized by using a silicon substrate bearing the TES that can later easily be glued onto the sapphire substrate. These composite detectors prove to be extremely satisfactory and due to their flexibility they have a high potential of applicability in other fields of cryogenic detection and also neutrino physics (e. g. β-endpoint measurements, neutrinoless $\beta\beta$-decay). Special care has also been given to the design of the 4π detector holder, since the implementation in a gallium experiment like GNO requires maximum redundancy in order not to lose a solar run and at the same time to ensure easy and straightforward handling. In addition to that a further cylindrical shielding made of ultrapure copper and low-activity lead, to be operated in a cryostat at temperatures of $\sim$100mK, was conceived and successfully realized to shield the 4π detector from the inner parts of the cryostat itself. Apart from the first results obtained with a composite detector, also radiopurity aspects concerning the material selection for the detector and its surroundings are presented in chapter 5.

In order to introduce low-temperature detectors in the experimental procedure of a gallium experiment, a suitable interface is needed. Using the dissociation process of germane gas (GeH$_4$) at temperatures higher than 280°C, it is possible to deposit the neutrino-produced germanium (^{71}Ge; T$_{1/2}$ = 11.43d) within a metallic film onto a sapphire substrate (Al$_2$O$_3$), later to become the absorber of the cryogenic detector. This process has to be highly efficient. In our experiments it has been performed up to a level of $\geq 91\%$ thus meeting the requirements of the GALLEX/GNO experiment. This procedure is briefly described in chapter 6.

With the aim to show the feasibility of using cryogenic detectors in a gallium experiment (GNO), a ^{3}He/^{4}He dilution refrigerator (Oxford: Kelvinox 150) was installed in the underground laboratory (UGL) of the Maier-Leibnitz-Laboratorium in Garching. The shielding of the experimental setup has been improved progressively. The cryostat is now completely surrounded by 15cm of lead equipped with a muon-veto that can be operated in anticoincidence with the cryogenic detector. Background and long-term ^{71}Ge measurements using composite detectors have been performed. As a last step, to show the long-term stability of the cryogenic measuring system, the decay curve of reactor activated ^{71}Ge was measured in the UGL for a total of 35 days without interruption. The results of

these measuring campaigns as well as results from composite detectors using macroscopic lead absorbers are presented in chapter 7.

In a collaborational work with the cryogenic detector group of the I.N.F.N (Istituto Nazionale Di Fisica Nucleare) Genova, a strive for high energy resolution with microcalorimeters using the technique of composite detectors was performed. The results of first measurements using iridium-gold TESs, produced in our laboratory in Garching, and tin as an absorber are presented in chapter 8. An energy resolution of 5.9eV (FWHM) at 5.9keV has been achieved. This represents a world-wide record for cryodetectors relying on TES sensors.

Contents

Chapter 1

Introduction

1.1 History of the Neutrinos

Neutrinos first appeared on the elementary particle stage in 1930 when W.Pauli postulated the existence of a so called 'neutron' [1]. Pauli introduced this new particle, later baptized neutrino by E. Fermi, in order to explain the continuous shape of the β-spectrum without violating conservation of energy and angular momentum (spin). It was not until 26 years later that Cowan and Reines measured for the first time neutrinos directly [2], [3], [4]. Using a $CdCl_2$-solution as target, they were able to detect antineutrinos via the reaction

$$\bar{\nu}_e + p \longrightarrow e^+ + n \tag{1.1}$$

The antineutrinos were produced in nuclear fission processes in the nearby Savannah River (USA) nuclear reactor. To view positron annihilation γ's as well as γ's due to the delayed capture of the neutron on Cd, the experimental setup was based on liquid scintillator detectors. A detection technique for neutrinos used to present day only on larger and more complicated scale, liquid scintillator detectors in the kiloton-range like KamLAND, Borexino, LENS, LENA, can be expected to further contribute to our understanding of such an elusive particle. Further highlights in neutrino physics were the discovery of parity violation in the electroweak interaction by the Wu experiment [5], and the measurement of the neutrino's helicity by Goldhaber in 1958 [6]. The muon neutrino was discovered in 1961 at the Brookhaven Proton Synchrotron by Ledermann, Schwarz und Steinberger [7]. The first direct measurement of the tau neutrino was made in the year 2000 by the DONUT experiment at Fermilab [8].

The number N_ν of active neutrino flavours can be deduced from the decay width of Z_0. Measurements of the total Z_0 decay width and the widths of the visible decay channels at LEP yield an experimental value of N_ν=2.984±0.008, which is close to the expected number of 3 [9].

In the standard model of particle physics neutrinos are mass and chargeless and described by the theory of electroweak interaction. The model assumes three left-handed neutrinos, which reside in left-handed lepton doublets:

$$L_\alpha = \begin{pmatrix} \nu_{L\alpha} \\ \alpha_L \end{pmatrix} \quad \alpha = e, \mu, \tau \tag{1.2}$$

As described in more detail in section 1.2.4, experiments involving solar, atmospheric and reactor neutrinos demonstrate the existence of flavour transitions by means of neutrino oscillations. However, neutrino oscillations imply that at least two neutrinos have non-zero mass, which requires an extension of the standard model of particle physics.

In this context it is clear that the determination of the masses of the neutrinos is of great importance. Up to now, only upper limits from various experiments are given for the neutrino mass. The Mainz and Troitsk [10] experiments [11], which both are based on the precise measurement of the endpoint of the tritium decay, give a limit of $\leq$2.2eV/c^2 at 95% confidence level (see also chapter 8). KATRIN, an upcoming experiment also based on the measurement of the tritium endpoint, is designed to have a sensitivity of 0.2eV/c^2 [12]. As described in more detail in chapter 8 high-resolution cryogenic detectors can be used as well for high precision measurements of the endpoint of a β-spectrum, e.g. of ^{187}Re [13], [14].

Another way to determine an upper mass limit of the neutrinos is the cosmological approach. Using a combination of WMAP (Wilkinson Microwave Anisotropy Probe) data on the cosmic microwave background as well as results from galaxy redshift measurements [15], it is possible to give a limit for the total mass of all neutrinos of $\leq$1.0eV/c^2. This value can be regarded as conservative in the context of interpreting cosmological data which, however, is highly model dependent.

A possibility to investigate the nature of the neutrino, that is to determine whether it is a Majorana or Dirac particle, is the neutrinoless double beta decay ($0\nu\beta\beta$). In the case of the neutrino being a Majorana particle, i.e. particle and anti-particle are identical, a mass

limit can be deduced from these measurements, too. Collaborators from the Heidelberg-Moscow experiment, which uses ^{76}Ge, claim to have observed $0\nu\beta\beta$-decay for the first time [16]. If these measurements are correct they will have proven that the neutrino is indeed a Majorana particle. Also an upper mass limit of $0.35\text{eV}/\text{c}^2$ at 90% confidence level has been derived [16]. Other experiments, based on the same or different isotopes are presently underway or already measuring, like CUORICINO, CUORE (TeO$_2$). Also a new generation germanium experiment is under preparation: GERDA. A promising approach would also be the use of cryogenic detectors to detect $0\nu\beta\beta$ in ^{150}Nd [17]; preliminary efforts in this direction have been made at our institute and will be continued in the future.

1.2 Solar Neutrino Physics

The field of solar neutrino research was initiated by the question of how the energy in the sun is generated. The goal was to see if the predicted rate of neutrinos produced in the sun during various fusion reactions would agree with their measured number on earth. It was the experimental search for those solar neutrinos that started a whole new era of particle physics, namely neutrino and astroparticle physics.

1.2.1 The Solar Neutrino Spectrum

The energy production inside the sun is based on the thermonuclear fusion of hydrogen to helium, the sum reaction can be written as

$$4\text{p} \longrightarrow^4 \text{He} + 2\text{e}^+ + 2\nu_e + 26.73\text{MeV} \tag{1.3}$$
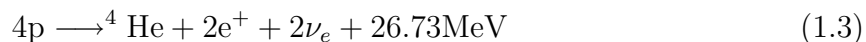
Indeed, the fusion processes follow several branches which are depicted in figure 1.1. Based on the pioneering works of Bethe and Weizsäcker [18], [19], who first proposed thermonuclear fusion to be responsible for the energy production in the sun, more detailed and complex models were conceived, notably the various so-called standard solar models (SSMs)[20]. A SSM allows to calculate neutrino fluxes on earth originating from the different fusion branches shown in figure 1.1.

The main contribution to the energy production inside the sun is due to the pp-cycle. As can be seen in figure 1.1 the fusion of two protons to deuterium can occur directly (pp-reaction) or with a reduced probability together with an electron (pep-reaction). Since

(pp) $\boxed{\text{p} + \text{p} \rightarrow {}^2\text{H} + \text{e}^+ + \nu_\text{e}}$ $\qquad$ $\boxed{\text{p} + \text{e}^- + \text{p} \rightarrow {}^2\text{H} + \nu_\text{e}}$ (pep)

99,8% $\qquad\qquad\qquad$ 0,2%

$\boxed{{}^2\text{H} + \text{p} \rightarrow {}^3\text{He}}$

85% $\qquad\qquad\qquad\qquad\qquad$ 10^{-8}

$\boxed{{}^3\text{He} + {}^3\text{He} \rightarrow {}^4\text{He} + 2\text{p}}$ $\qquad$ 15% $\qquad$ $\boxed{{}^3\text{He} + \text{p} \rightarrow {}^4\text{He} + \text{e}^+ + \nu_\text{e}}$

pp-chain I $\qquad\qquad\qquad\qquad\qquad\qquad\qquad$ pp-chain IV $\quad$ (hep)

$\boxed{{}^3\text{He} + {}^4\text{He} \rightarrow {}^7\text{Be}}$

99,98% $\qquad\qquad\qquad\qquad\qquad$ 0,02%

(⁷Be) $\boxed{{}^7\text{Be} + \text{e}^- \rightarrow {}^7\text{Li} + \nu_\text{e}}$ $\qquad$ $\boxed{{}^7\text{Be} + \text{p} \rightarrow {}^8\text{B}}$

$\boxed{{}^7\text{Li} + \text{p} \rightarrow {}^4\text{He} + {}^4\text{He}}$ $\qquad$ $\boxed{{}^8\text{B} \rightarrow {}^8\text{Be} + \text{e}^+ + \nu_\text{e}}$ $\quad$ (⁸B)

pp-chain II $\qquad\qquad\qquad\qquad\qquad$ $\boxed{{}^8\text{Be} \rightarrow {}^4\text{He} + {}^4\text{He}}$

pp-chain III
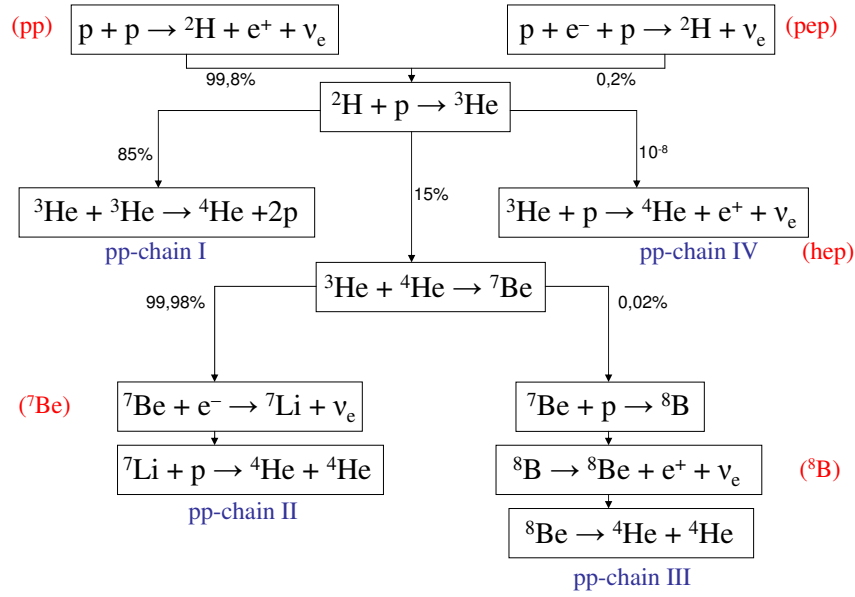
Figure 1.1: Fusion branches in the sun. The pp-fusion chain is responsible for ∼98.5% ([21]) of the energy production in the sun as calculated by present SSMs. The figure illustrates the various contributing reactions as well as their branching ratios; the names used to identify the neutrinos from the different reactions are marked in red.

the pp-reaction results in a three body process, it is of continuous shape, whereas the pep-reaction with finally two particles, leads to a monoenergetic line in the solar neutrino energy spectrum depicted in figure 1.2. Once deuterium is produced it 'acquires' a further proton forming ^{3}He. From this point on the fusion can be terminated in 4 different ways. These chains are labelled pp-chain I to IV (see figure 1.1) and have different probabilities of occurrence. These probabilities are related to the cross-sections of the individual nuclear reactions, the solar density profile, the element abundances and the temperature. In three of the four fusion branches neutrinos are produced leading to two monoenergetic ^{7}Be lines and continuous ^{8}B and hep neutrino spectra as shown in figure 1.2. The by far predominant component is the pp-flux. Since it is directly related to the luminosity of the sun it can be predicted with high accuracy ($\pm 1\%$) which is largely independent of SSM calculations. According to the SSMs, the CNO cycle, illustrated by dotted lines in figure 1.2, contributes only 1.5% [21] to the overall energy production in the sun. In the CNO-cycle, the elements C, N, O and F act as catalysts for the fusion of 4 protons into helium. Solar neutrino experiments allow to give an upper limit for the CNO contribution to the energy production. The neutrino spectra shown in figure 1.2 give the various contributions with the individual precisions as calculated by the SSM [21]. The predictions made by the SSMs have been cross-checked by means of helioseismology and largely confirmed [22].

1.2.2 Solar Neutrino Detection: Homestake and Kamioka Experiments

With the intention to measure solar neutrino fluxes down to energies of ~ 0.8MeV as shown in figure 1.2, Ray Davis Jr. in the 1960s conceived the first solar neutrino detector on earth. It was the so called Homestake Chlorine Experiment located in Lead, South Dakota. In 2002, Ray Davis was awarded the Nobel Prize in physics for his pioneering effort in trying to understand, whether the interior of the sun was functioning according to the way theorists predicted it in their standard solar models.

The experiment was set up underground to avoid undesired contributions to the measurement by cosmic radiation. The target consisted of 615 tons of perchlorethylene C_2Cl_4 contained in a huge tank. The idea was to expose the C_2Cl_4 solution to the ν_e flux from the sun using the following reaction to detect the ν_e

$$\nu_e + {}^{37}\text{Cl} \longrightarrow {}^{37}\text{Ar} + \text{e}^- \qquad (1.4)$$

The energy threshold for this reaction is 814 keV, thus covering one branch of the ^{7}Be neutrinos, however, inhibiting the detection of the dominant lower energy part of
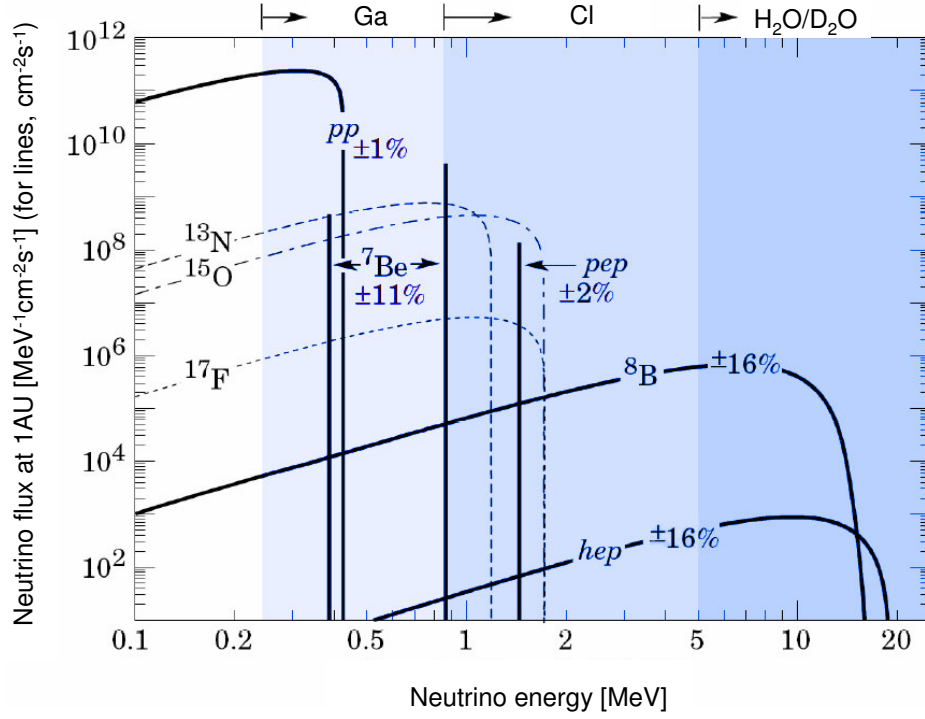
Figure 1.2: The solar neutrino energy spectrum on earth as predicted by the current standard solar model [21]. Contributions from the pp-chain branches (see figure 1.1) are plotted as solid lines, the CNO contributions as dotted lines. The precisions indicated for the various branches are derived from SSM calculations. The top part of the diagram illustrates from left to right the energy thresholds for the gallium (GALLEX/GNO/SAGE), chlorine (Homestake), as well as the water (SuperKamiokande) and heavy water (SNO) experiments.

the solar neutrino spectrum, the pp-neutrinos. After a typical exposition of 60 to 100 days literally a handful of ^{37}Ar had to be extracted from the tank in a highly efficient chemical procedure and then to be measured in low-background proportional counters. The number of decaying ^{37}Ar atoms (half-life: $\sim$35d) thus reflected the neutrino flux to which the target had been exposed. The measured event rate was only $\approx 1/3$ of the value that was predicted by solar models. This result led to two consequences: a) the SSM was wrong, or b) unknown properties of the ν_e were responsible.

The Kamioka detector [23] in the Kamioka mine (2700m.w.e.) 300km west of Tokyo, Japan, was a water Cerenkov detector constructed in 1983 aiming at measuring solar neutrinos via elastic neutrino electron scattering:

$$\nu + e^- \longrightarrow \nu + e^- \tag{1.5}$$

The Cerenkov light emitted by the recoil electron in water (fiducial volume, 680t) is detected by a large number of photomultipliers surrounding the water target. In comparison to a radiochemical experiment like the Homestake chlorine experiment, Cerenkov detectors offer the possibility of real-time detection at the cost of a higher energy threshold (see figure 1.2). The energy threshold (for recoil electrons) was 9.3MeV at first, and could later be improved to 7.5MeV. Nevertheless, the detector was only sensitive to the high-energy part of the solar neutrino spectrum (see figure 1.2), the ^{8}B and hep neutrinos. The neutrino flux measured was only $\sim$50% of the predicted value by the SSM [24]. Just like in the chlorine experiment, the measured neutrino flux did not correspond to the predictions made by solar theories, even though the errors were smaller. In 2002 Masatoshi Koshiba, from the Kamiokaande collaboration, was awarded the nobel prize for pioneering contributions to astrophysics, in particular for the detection of cosmic neutrinos.

1.2.3 Present Status of Solar Neutrino Detection

In the early 1990s two radiochemical experiments, GALLEX in Italy and SAGE in Bhaksan, Russia, started to investigate the low-energy part of the neutrino spectrum. Both experiments are based on electron-neutrino capture on^{71}Ga:

$$\nu_e + {}^{71}\text{Ga} \longrightarrow {}^{71}\text{Ge} + e^- \tag{1.6}$$

GALLEX/GNO used a liquid gallium chloride solution as a target, whereas SAGE first used 30t and later 57t of metallic gallium [25]. The energy threshold of both exper-

iments is 233keV, thus allowing to investigate pp-neutrinos (see figure 1.2). In analogy to the chlorine experiment the few neutrino-produced instable ^{71}Ge atoms were measured in miniaturized low-background proportional counters. A detailed description of the experimental procedure, as well as a summary of the results of GALLEX/GNO is given in chapter 2. However, also these two experiments measured only ∼60% of the predicted signal. The overall result of these two experiments after more than a decade of measuring is:

$$(69.3 \pm 4.1[\text{stat.}] \pm 3.6[\text{syst.}])\text{SNU (GALLEX/GNO)} \tag{1.7}$$

$$(66.9 \pm 3.9[\text{stat.}] \pm 3.6[\text{syst.}])\text{SNU (SAGE)} \tag{1.8}$$

Both results agree well within the error margins.

In 1996 an enlarged version of the Kamioka water Cerenkov detector was built with a fiducial volume of 22500t and an energy threshold of ∼5MeV, Super-Kamiokande. Apart from the detection of the solar neutrinos, this detector was also conceived to measure atmospheric neutrinos, as well as to search for proton decay. Since this type of detectors exhibits a directional sensitivity, it proved that the neutrinos measured did indeed originate from the sun. Again this detector measured only ∼40.6% of the predicted solar neutrino event rate. Further details are given in [26].

The SNO (Sudbury Neutrino Observatory) detector located in the Creighton mine (6000m.w.e) close to Sudbury, Canada, is also a real-time Cerenkov detector with an energy threshold of ∼5MeV (see figure 1.2). The target in this case is provided by 1000t of heavy water (D_2O) contained in an acrylic vessel, monitored by ∼9500 8-inch-photomultipliers and surrounded by 1700t of ultrapure water. Neutrinos crossing the D_2O volume can be detected via three different reactions:

$$\nu_e + D \longrightarrow p + p + e^- \ (CC) \tag{1.9}$$

$$\nu_x + D \longrightarrow \nu_x + p + n \ (NC) \tag{1.10}$$

$$\nu_x + e^- \longrightarrow \nu_x + e^- \ (ES) \tag{1.11}$$

Flavour transitions from ν_e to ν_μ or ν_τ can be determined by comparing the interaction rates measured by the charged current reaction (CC) and the neutral current reaction (NC).

$$\frac{CC}{NC} = \frac{\Phi(\nu_e)}{\Phi(\nu_e + \nu_\mu + \nu_\tau)} \tag{1.12}$$

Since only electron neutrinos are produced in the sun, an excess in the neutral current rate can only be attributed to a ν_μ or ν_τ component in the solar neutrino flux originating from flavour transitions on their way to earth. The electron scattering process (ES) allows a further measurement of neutrino interaction and a cross-check of the other two reactions CC and NC , however, with less statistic significance. The latest results reported by the SNO collaboration [27] in units of $10^6 \text{cm}^{-2}\text{s}^{-1}$ are:

$$\Phi_{CC} = 1.68 \pm 0.06(\text{stat.})^{+0.08}_{-0.09}(\text{syst.}) \tag{1.13}$$

$$\Phi_{NC} = 4.94 \pm 0.41(\text{stat.})^{+0.38}_{-0.34}(\text{syst.}) \tag{1.14}$$

$$\Phi_{ES} = 2.35 \pm 0.22(\text{stat.})^{+0.15}_{-0.15}(\text{syst.}) \tag{1.15}$$

Results of the measurements by the SNO experiment are shown in figure 1.3. The diagram exhibits the flux of non-electron flavour active neutrinos ($\nu_{\mu\tau}$) versus the flux of electron neutrinos (ν_e). The error ellipses shown are the 68%, 95% and 99% joint probability contours for $\Phi_{\mu\tau}$ and Φ_e. The measured value of $\Phi_{\mu\tau}$ shows that $\sim$2/3 of the electron neutrinos have undergone flavour transition.

These results include also data from SNO's saltphase where 2.7t of NaCl were added to the D_2O to improve the n-detection efficiency of the NC reaction. For further details see [27]. The SNO experiment has hereby proven that part of the electron neutrinos produced inside the sun alter their flavour due to the oscillation scenario described in section 1.2.4 below. The favoured explanation for the neutrino deficit measured so far by every solar neutrino experiment except for the NC reaction in SNO, was first proposed in 1968 by Gribov and Pontecorvo [30], [31], who introduced the idea of neutrino oscillations. The theoretical assumptions on which this theory is based, involving non standard properties of the neutrinos, are presented at the end of next section (1.2.4).

1.2.4 Physics beyond the Standard Model - Neutrino Oscillations

Figure 1.4 shows the measured lack of the neutrino interaction rate compared to the predictions by SSMs (colour); from left to right the results are given from the experiments mentioned in the sections above, together with the individual predictions of the SSM. This diagram exhibits clearly the non-standard nature of neutrinos. All experiments based on
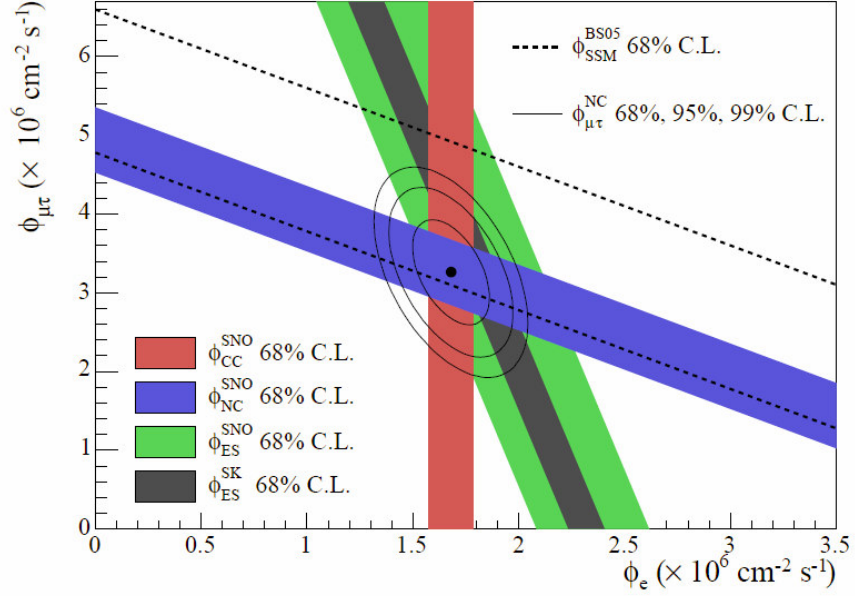
Figure 1.3: Flux of $\mu + \tau$ neutrinos versus flux of electron neutrinos. CC, NC and ES flux measurements are indicated by the filled bands [27]. The total ^{8}B solar neutrino flux predicted by the SSM [28] is shown as dashed lines, and that measured with the NC channel is shown as the solid band parallel to the model prediction. The narrow band parallel to the SNO ES result corresponds to the Super-Kamiokande result in [29]. The intercepts of these bands with the axes represent the $\pm 1\sigma$ uncertainties. The non-zero value of $\Phi_{\mu\tau}$ provides strong evidence for neutrino flavour transformation. The point represents Φ_e from the CC flux and $\Phi_{\mu\tau}$ from the NC-CC difference with 68%, 95% and 99% C.L. contours included.

Figure 1.4: Comparison of neutrino interaction rates as predicted by SSMs with results of measurements performed by different experiments relying on individual detection techniques [32].
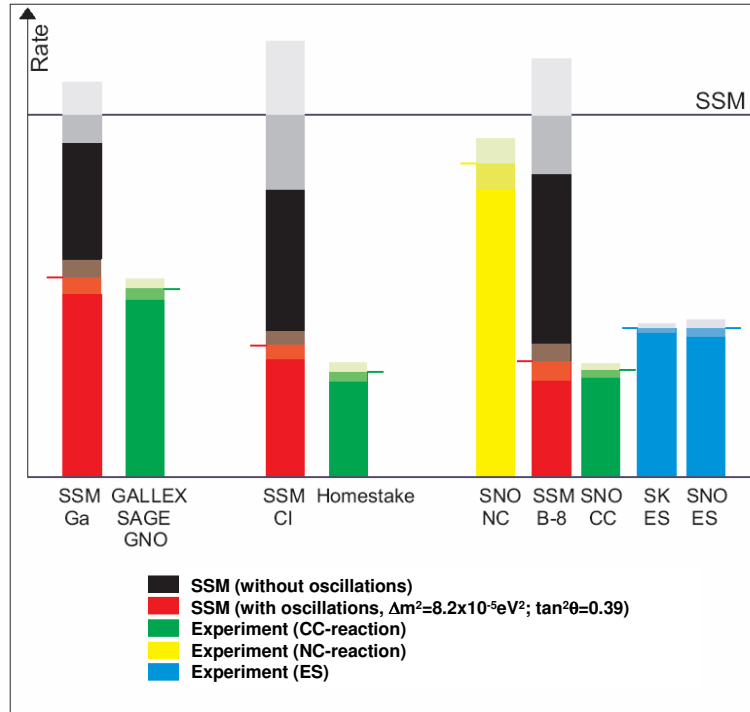
CC and ES detection exhibit a clear deficit which has been referred to in literature as the 'solar neutrino puzzle'. Today it seems solved, assuming neutrino oscillations as the main reason for this non-standard-particle behaviour. Also theoretical predictions (MSW-effect, see below) treating energy-dependent suppression of the neutrino flux on earth due to interaction of electron neutrinos with solar matter have proven to be right.

Neutrino oscillations are a quantum mechanical effect:

A neutrino of flavour ν_α produced in a weak process is described by a coherent linear superposition of mass eigenstates

$$|\nu_\alpha\rangle = \sum_i U_{\alpha i} |\nu_i\rangle \tag{1.16}$$

In an extended standard model in which neutrinos have mass and the lepton numbers L_e, L_μ and L_τ are not conserved, the electron, muon and tau neutrinos in the lepton doublets (see equation 1.2) are flavour eigenstates which relate to the mass eigenstates ν_1, ν_2 and ν_3 with the eigenvalues m_1, m_2 and m_3 via the unitary mixing matrix U. The evolution in time of the stationary mass eigenstates $|\nu_i\rangle$ with the phase factors $e^{-iE_i t}$ and energy E_i follows the Schrödinger equation. After a certain time t, $|\nu_i\rangle$ has evolved to

$$|\nu_i(t)\rangle = e^{-iE_i t} |\nu_i\rangle \tag{1.17}$$

In the 'simple' case where only two states are involved the mixing matrix can be parameterized by one mixing angle θ

$$U = \begin{pmatrix} \cos\theta & \sin\theta \\ -\sin\theta & \cos\theta \end{pmatrix} \tag{1.18}$$

It is the non-diagonal structure of the matrix that leads to oscillations. Assuming the ultra-relativistic limit ($m_i << E_\nu$) the oscillation probability, i.e. the probability of a neutrino produced as $|\nu_\alpha\rangle$ to be detected as $|\nu_\beta\rangle$ is

$$P_{\nu_\alpha \longrightarrow \nu_\beta} = \left| \langle \nu_\beta | e^{-iE_i t} | \nu_\alpha \rangle \right|^2 = \sum_{ij} U_{\alpha i} U_{\alpha j}^* U_{\beta i}^* U_{\beta j} exp(-i\frac{\Delta m_{ij}^2 L}{2E}) \tag{1.19}$$

where $\Delta m_{ij}^2 = m_i^2 - m_j^2$ are the mass-squared differences, L the distance from the production point and E the neutrino energy. Therefore neutrino oscillations do not depend

on absolute masses, but on the differences Δm_{ij}^2. The oscillation probability $P_{\nu_\alpha \longrightarrow \nu_\beta}$ and the survival probability $P_{\nu_\alpha \longrightarrow \nu_\alpha}$ can be expressed as

$$P_{\nu_\alpha \longrightarrow \nu_\beta} = sin^2(2\theta)sin^2 \left(\frac{\Delta m^2 L}{4E} \right) \tag{1.20}$$

$$P_{\nu_\alpha \longrightarrow \nu_\alpha} = 1 - sin^2(2\theta)sin^2 \left(\frac{\Delta m^2 L}{4E} \right) \tag{1.21}$$

When neutrinos propagate through matter they experience coherent elastic forward scattering [33], which, however, is different for ν_e (as compared to that for ν_μ and ν_τ) due to CC-interaction with the electrons. This so-called MSW-effect (named after Mikeyhev, Smirnov, and Wolfenstein [34], [33]), is essentially important when describing neutrinos leaving the solar core. Their oscillatory behaviour is affected by the interaction with electrons of the sun-plasma. To describe this behaviour the Schrödinger equation for electron neutrino propagation in matter is modified by a term containing an additional effective potential V:

$$V = \sqrt{2}G_F N_e \tag{1.22}$$

where G_F is the Fermi-constant and N_e the electron density. The consequence is a difference in the mass eigenstates in vacuum and in matter. Consecutively, the effective mixing parameters taking into account matter interaction, are referred to as θ_m and Δm_m^2, both depending on the neutrino energy as well as on the electron density. Since the sun is not of constant density along its radius, neutrinos emitted from the core to the outside can meet so-called resonant conditions when crossing a certain electron density. This then can lead to an effective mixing angle of $\theta_m = 45°$, causing maximum mixing.

Taking into account the results of all solar neutrino experiments, one can deduce limits in the parameter space for Δm_{21}^2 and $tan^2\theta$. Figure 1.5a shows the allowed parameter region at different C.L.s. This favoured region is referred to as the Large Mixing Angle (LMA) solution. Figure 1.5b shows the combined result of solar and KamLAND data. KamLAND measured for the first time an electron antineutrino disappearance signal and cross-confirmed, independently from solar neutrino measurements, the hypothesis of neutrino oscillations. The KamLAND experiment is located in Japan and measures electron antineutrinos from several nuclear power reactors with an average distance of a ~200km to the detector (for details, see [35], [73]). In fact, the experiment was the first to favour the LMA solution [35], which was later confirmed by other experiments like

SNO and Super-Kamiokande. The impact of this experiment is clearly visible in figure 1.5b, where the parameter space for Δm_{21}^2 and $\tan^2\theta_{12}$ is further constrained. The best fit point gives a value of $7.9^{+1.0}_{-0.8} \cdot 10^{-5}\text{eV}^2$ for Δm_{21}^2, and a value of $0.40^{+0.18}_{-0.13}$ for $\tan^2\theta_{12}$ [37].
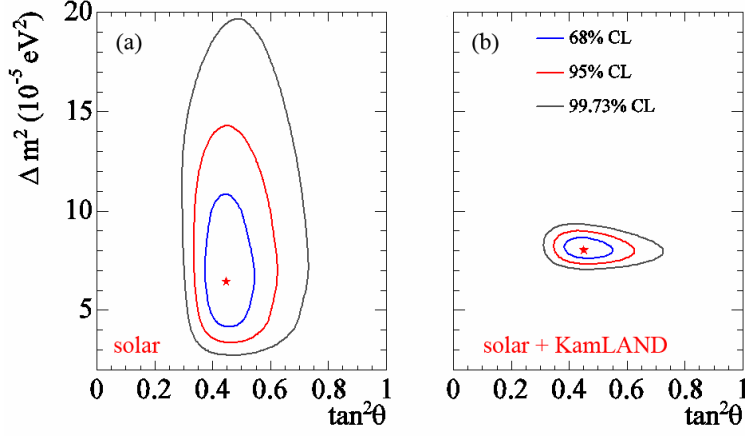
Figure 1.5: a) Global neutrino oscillation analysis [27] using only solar neutrino data, and b) including KamLAND 766 ton-year data. The solar neutrino data include SNO's pure D_2O phase day and night spectra, SNO's salt phase extracted day and night CC spectra and ES and NC fluxes, the rate measurements from the Cl, SAGE, GALLEX/GNO, and SK-I zenith spectra. The stars represent the best-fit parameters.

As an example with slightly different values for the oscillation parameters [38] figure 1.6 illustrates the energy dependence of the survival probability $P_{\nu_e \longrightarrow \nu_e}$. For smaller energies it is like for the vacuum oscillation scenario, at higher energies it is dominated by the MSW-effect. The transition region between $\sim$0.8 and $\sim$4MeV has not yet been investigated experimentally. Experiments like BOREXINO (for further details, see [39]) and KamLAND (for further details, see [73]), but also a new generation of solar neutrino experiments (LENA, LENS) could probe this region. Deviations from the LMA-I curves (e. g. the curves LMA-O and LMA-D) would demonstrate that LMA(MSW) oscillations are not the dominant effect and rather additional interactions (e. g. via possible magnetic transition moments of the neutrino) would be important.
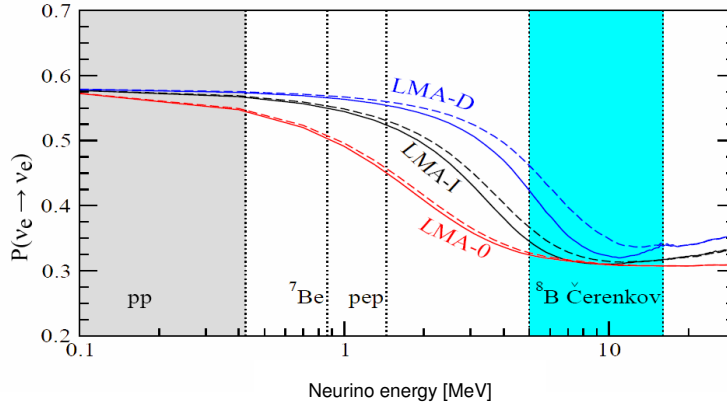
Figure 1.6: Energy-dependent survival probability for the large mixing angle solution (LMA). The LMA-I solution is defined by the parameters $\Delta m_{21}^2 = 8.3 \cdot 10^{-5} \text{eV}^2$ and $\tan^2\theta$ = 0.43 (best fit point) [38]. LMA-0 and LMA-D are the solutions assuming non-standard-model interactions between neutrinos and matter. The solid and dotted lines correspond to different production points in the sun. The neutrino energy distributions originating from the various fusion cycles in the sun (pp in grey, ^{7}Be and pep in dotted lines and ^{8}B in green) are depicted on the x-axis [38].

1.3   Future Tasks in Neutrino Physics

The progress in neutrino physics, especially in the last few years, has been tremendous (and has already earned several nobel prizes). Triggered by solar neutrino spectroscopy, the non-standard-model behaviour of the neutrino has become a field of great interest and intense research, pointing in many different directions. Evidence for neutrino mixing and oscillations has been obtained by various experiments probing solar, atmospheric, reactor-generated and accelerator-generated neutrinos. Oscillation experiments have produced a picture where the three known neutrino flavours are mixtures of three mass eigenstates, the relations of which is described by the PMNS (= Pontecorvo-Maki-Nakagawa-Sakata) matrix [42]

$$
\begin{pmatrix} \nu_e \\ \nu_\mu \\ \nu_\tau \end{pmatrix} = \begin{pmatrix} 1 & 0 & 0 \\ 0 & c_{23} & s_{23} \\ 0 & -s_{23} & c_{23} \end{pmatrix} \begin{pmatrix} c_{13} & 0 & s_{13}e^{i\delta} \\ 0 & 1 & 0 \\ -s_{13}e^{-i\delta} & 0 & c_{13} \end{pmatrix} \begin{pmatrix} c_{12} & s_{12} & 0 \\ s_{12} & c_{12} & 0 \\ 0 & 0 & 1 \end{pmatrix} \begin{pmatrix} \nu_1 \\ \nu_2 \\ \nu_3 \end{pmatrix}
$$
(1.23)

with $s_{ij}=\sin\theta_{ij}$ and $c_{ij}=\cos\theta_{ij}$ and a CP violating phase δ. Equation 1.23 shows the PMNS matrix broken down into 3 components each handling a mass eigenstate pairing and its associated Δm^2:

- the 23-sector, measured by atmospheric oscillation experiments and by the K2K ([40]) long baseline measurement

- the 12-sector, describing solar neutrino oscillations and the KamLAND result

- and the 13-sector, which will be the main focus for next generation experiments.

Our understanding of the elusive neutrino is growing, however, only a large-scaled scientific strategy can bring forth the details of the neutrinos' physical properties. They are needed if the neutrinos are to give further information on stellar interiors or insights into supernovae or into the density profile of the earth. The results required can originate not only from already running experiments, but also from forthcoming detectors. To determine the properties of the neutrinos a variety of experimental techniques are required:

- Endpoint measurements to determine the absolute mass of the electron neutrino. β-endpoint measurements of ^{187}Re with cryogenic detectors [13] or β-endpoint measurements of tritium with a spectrometer like the upcoming KATRIN experiment [12] will give new upper limits of the neutrino mass.

- Future precision measurements of the cosmic microwave background (CMB) combined with galaxy surveys will yield limits perhaps as low as 0.04eV for the sum of the neutrino masses [41].

- Neutrinoless-double-beta-decay experiments to determine the nature of the neutrino, i.e. whether the neutrino is its own antiparticle or not (Majorana or Dirac particle) and to investigate the mass hierarchy. Since there is already evidence from one experiment [16] to have observed neutrinoless-double-beta decay, it will be the task of already existing or upcoming experiments like CUORICINO, CUORE and GERDA [43] to cross-check the above mentioned results. Also an experiment using the isotope ^{150}Nd together with cryogenic detectors might help to shed light on these questions.

- Precise determination of the mixing parameters by means of various detectors, sources and baselines. The 12-sector is probed by solar neutrino experiments (see section 1.2.3), however, there is still need for measurements yielding higher statistics and precision. Solar neutrino experiments have a good sensitivity to θ_{12}, KamLAND, on the other hand, a reactor experiment, is sensitive to the oscillation effect on the energy spectrum and can therefore make better restriction on Δm_{12}^2. SNO, Super-Kamiokande and future experiments like the proposed LENA (Low Energy Neutrino Astronomy) detector (for more details, see[44]) will also allow to further constrain the uncertainties in the 12-sector. Also other astrophysical neutrinos like from supernovae, as well as relic and geo neutrinos could be measured and investigated with a kilo-ton liquid scintillator detector like LENA, time and directionally resolved [48].

- Atmospheric neutrino oscillations, described by the 23-sector, have been measured by Super-Kamiokande and have recently been confirmed on a 3.9σ level by the K2K long baseline experiment [41] that observed the oscillation effect in both the reduction of flux and the energy shape distortion.

- θ_{13} can be investigated with reactor-neutrino experiments like Double CHOOZ [45] or accelerator neutrino experiments. These experiments may be able to settle the question of neutrino mass hierarchy and to investigate the CP violating phase δ (see equation 1.23).

- With a neutrino beam from CERN to Gran Sasso, experiments like ICARUS [46] and OPERA [47] are aimed at confirming the oscillation behaviour by detecting the appearance signal of ν_τ via $\nu_\mu \longrightarrow \nu_\tau$ oscillations.

Chapter 2

GNO - Monitoring Solar Neutrinos

The Gallium Neutrino Observatory (GNO), the successor experiment of GALLEX, was a radiochemical detector located in Hall A of the Laboratori Nazionali del Gran Sasso (L.N.G.S.) with a rock overburden of 3600 m.w.e. The experiment measured solar neutrinos for ~12 years (1991-2003) thus monitoring one solar cycle (~11y). Electron neutrinos with energies above 233 keV were detected via the inverse electron capture reaction

$$\nu_e + {}^{71}\text{Ga} \longrightarrow {}^{71}\text{Ge} + \text{e}^- \tag{2.1}$$

in a target consisting of 101 tons of a $GaCl_3$ solution in water and HCl, containing 30.3 tons of natural gallium. This amount corresponds to $\approx 10^{29}$ ^{71}Ga nuclei. Data taking was started by the international GALLEX collaboration in 1991, interrupted in 1997 for modifications in the data acquisition electronics and maintainance work concerning the chemical system and continued in May 1998 under the collaboration name, GNO. Measurements were stopped in April 2003 for external non-scientific reasons.

Not only did GALLEX recordings establish the presence of pp-neutrinos [49] until then only predicted by standard solar models, but also a significant deficit, the so-called solar-neutrino puzzle, in the sub-MeV neutrino induced rate [50], [51], [52]. At that time, this was the strongest indication for deviations of neutrino properties from the predictions of the standard model of particle physics, e.g. for neutrino transformations on the way between the solar core and the earth, implying non-zero neutrino mass [55], [56], [57] and [58]. The subsequent GNO, as well as similar measurements of the gallium experiment SAGE in Bhaksan (see [25]) observations have improved the quality of the data, added important restrictions on the presence of possible time variations, and substantially reduced the total error on the charged current reaction rate for pp-neutrinos as measured by

the inverse beta decay on gallium [74]. Most important, together with the Cl-experiment [59] and the real-time measurements by Superkamiokande [26], and SNO [27], it has been established that neutrino flavour oscillations (the so-called LMA (MSW) solution, see section 1.2.4) are by far the dominant mechanism responsible for the solar neutrino deficit. Without radiochemical gallium detectors, the majority (93%) of all solar neutrinos would still have remained unobserved.

GALLEX/GNO have provided a long time record of low energy solar neutrinos and determined the bulk production rate with an accuracy of 5.5 SNU. This is based on 123 solar runs (SRs), 65 from GALLEX and 58 from GNO. The results of GALLEX/GNO and SAGE and their precision will remain without competition from eventually upcoming low-threshold real-time experiments for many years to come. The gallium experiments have recorded a fundamental astrophysical quantity, the neutrino luminosity of the sun. Lack of these basic data would have a very negative impact on the interpretation of the results from forthcoming second generation (real-time and low threshold) solar neutrino experiments such as BOREXINO (aiming at ^{7}Be neutrino detection). In the astrophysical context, the gallium results shed light also on the relative contributions of the PPI, PPII and CNO cycles to the solar luminosity and on the agreement of the energy production derived from the photon and neutrino luminosities.

2.1 Experimental Setup

The neutrino produced ^{71}Ge is radioactive, and decays via electron capture (EC) to ^{71}Ga:

$$e^{-} + ^{71}\mathrm{Ge} \longrightarrow ^{71}\mathrm{Ga} + \nu_e \tag{2.2}$$

The half-life of this decay is of $\sim$11.4d; the meanlife $\sim$16.4d: thus ^{71}Ge accumulates in the solution, reaching equilibrium when the number of ^{71}Ge atoms produced by neutrino interactions is just the same as the number of the decaying ones. When this equilibrium condition is reached, about a dozen ^{71}Ge atoms are present inside the chloride solution of GNO. The solar neutrino flux above threshold is then deduced from the number of ^{71}Ge atoms produced, using theoretically calculated cross sections as e.g. in [21]. The ^{71}Ge atoms are identified by their decay after chemical extraction from the target.

The experimental procedure for the measurement of the solar neutrino flux, referred to as 'a solar run' (SR), is the following (see figure 2.1): The solution is exposed to solar neutrinos for about 4 weeks; at the end of this time $\sim$10 ^{71}Ge nuclei are present in the
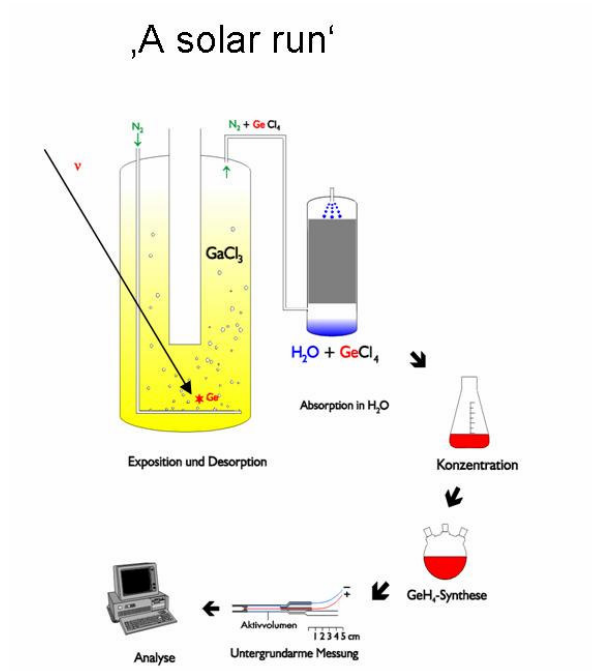
Figure 2.1: Performing a solar run (SR) in GNO: After an exposure of 3-4 weeks, the neutrino-produced ^{71}Ge is extracted by flushing the GaCl$_3$ solution with nitrogen and by absorption in water. After concentration of the obtained liquid and synthesis of GeH$_4$ (germane gas), the latter is mixed with xenon and filled into miniaturized proportional counters. The ^{71}Ge decay is then measured in a low background environment, followed by the analysis of the data.

solution, due to solar neutrino interactions on ^{71}Ga. ^{71}Ge, present in the solution in the form of volatile GeCl$_4$, is chemically extracted [49] into water by pumping $\approx$2000 m^3 of nitrogen through the target solution. The extracted ^{71}Ge is then converted into GeH$_4$ (germane gas), mixed with Xenon as counting gas and finally introduced into miniaturized proportional counters. The overall chemical extraction procedure is a highly efficient one: a mean value of 95.7% (yields range from 91.2% to 98.7%) for the transfer of the ^{71}Ge into the counter has been reached; extraction and conversion efficiencies are under constant control using non-radioactive germanium isotopes, such as ^{70}Ge, ^{72}Ge, ^{74}Ge, and ^{76}Ge alternately as carriers. The overall efficiency is not of a desirable 100% since there are unavoidable loss processes such as germanium atoms escaping the chemical extraction out of the target solution or losses that occur during the conversion of GeCl$_4$ into the counting gas component GeH$_4$ (germane gas) and in the counter filling procedure. ^{71}Ge electron-capture decay is observed for a period of 6 months, allowing the complete decay of ^{71}Ge and a good determination of the counter background. The intrinsic counter background is minimized by application of low-level-radioactivity technology in counter design and construction. The residual background is mostly rejected through application of amplitude and shape analysis to the recorded pulses. ^{71}Ge decays produce pulses originating from X-rays corresponding to an energy around 10.4 keV ('K peak') or 1.2 keV ('L peak') and Auger electrons (see chapter 7, table 7.1). In the late measuring periods of GNO the 'classical' pulse shape analysis has been replaced by a neural network analysis [66]. Counters have been calibrated by an external Gd/Ce X-ray source, in order to carefully define amplitude and pulse shape cuts with known efficiency for each measurement. The event amplitude and shape selection reduces the mean background rate to less than 0.1 counts per keV and day. The selected data are analyzed with a maximum likelihood method to obtain the most probable number of ^{71}Ge nuclei at the beginning of counting, which (after correcting for counting, extraction and filling efficiencies) gives the number of ^{71}Ge nuclei produced in the solution during the exposure and, therefore, the ^{71}Ge production rate. A correction is applied to account for contributions to the observed signal from processes other than solar neutrino capture, producing ^{71}Ge as well (so called 'side reactions'), mainly due to interactions in the solution generated by high-energy muons from cosmic rays and by natural radioactivity. Another correction is made to account for background signals in the counter that can be misidentified as ^{71}Ge decays. The total subtraction is typically of the order of a few percent of the signal [74].

2.2   Results of GALLEX/GNO

In this section a summary of the results from the GALLEX/GNO experiments [74] and their implications concerning both particle and astrophysics are presented.

2.2.1   12 Years of Data-Taking

In total seven measuring campaigns were performed, GALLEX I-IV and GNO I-III, resulting in a number of 123 solar runs.
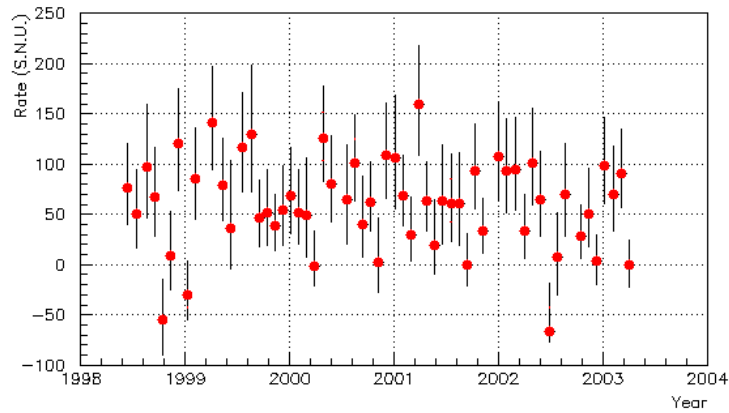

Figure 2.2: GNO results, electron neutrino induced production rate versus time of measurement of GNO (1998-2003).

The results from the three measuring campaigns GNOI-III are shown in figure 2.2. Altogether 58 solar runs were performed in the time between May 1998 and April 2003. After subtraction of 4.55SNU to account for side reactions, the overall result is:

$$62.9^{+5.5}_{-5.3}(\text{stat}) \pm 2.5(\text{syst.}) \ \text{SNU} \tag{2.3}$$

The systematic error, compared to GALLEX, was reduced by a factor of $\sim$2 and is in the order of 4%. The different error contributions are listed in table 2.1. The main

GNOI-III	in %	in SNU
^{71}Ge detection efficiency (energy cuts)	$\pm2.2\%$	±1.4
^{71}Ge detection efficiency (pulse shape cuts)	$\pm1.3\%$	±0.8
extraction yield	$\pm2.1\%$	±1.3
target mass	$\pm0.8\%$	±0.5
side reactions subtraction error	$\pm2.1\%$	$\pm1.3\%$
total systematic error	$\pm4.0\%$	±2.5

Table 2.1: Main contributions to the overall systematic uncertainty in GNO.

	GNO I-III	GALLEX I-IV	GNO + GALLEX
Time period	20/05/98-09/04/03	14/05/91-23/01/97	14/05/91-09/04/03
Net exposure time [d]	1687	1594	3281
Result [SNU]	$62.9^{+6.0}_{-5.9}$	$77.5^{+7.6}_{-7.8}$	69.3 ± 5.5

Table 2.2: Results from GALLEX and GNO. Statistical and systematic errors are combined in quadrature. Errors quoted are 1σ.

contributions ($\sim\pm2.6\%$) to the total error ($\pm4\%$) are due to uncertainties generated by the limited detection efficiency of the miniaturized proportional counters (65-75%).

Table 2.2 gives the time periods when the experiments GALLEX and GNO were in operation, the net exposure times and the final results in solar neutrino units (SNU). The combined data sets of GNO I-III and GALLEX I-IV lead to a result of 69.3±5.5SNU for the neutrino capture rate on ^{71}Ga. The updated result of the SAGE experiment of $66.9^{+5.3}_{-5.0}$SNU (1σ) [60], agrees well with this result. Figure 2.3 shows the result of all the 123 SRs covering a measuring period of 12 years. Already GALLEX alone with a result of $77.5^{+7.6}_{-7.8}$ SNU (corresponding to $\sim60\%$ of the rate predicted by SSMs) indicated non standard model properties of the neutrino and confirmed that the idea of thermonuclear fusion being the source of energy inside the sun, was correct.

2.2.2 Implications for Particle Physics and Astrophysics

- **Particle physics context:** Concerning both particle physics as well as astrophysics, low-energy solar neutrino experiments are of high importance also in the years to come (see, [61]). The electron neutrino capture rate on ^{71}Ga could be measured with an accuracy of 8%. Since the combined experimental results of GALLEX and GNO without taking into consideration neutrino oscillations diverge clearly (on a 5σ level) from theoretical predictions made by standard solar models, the results
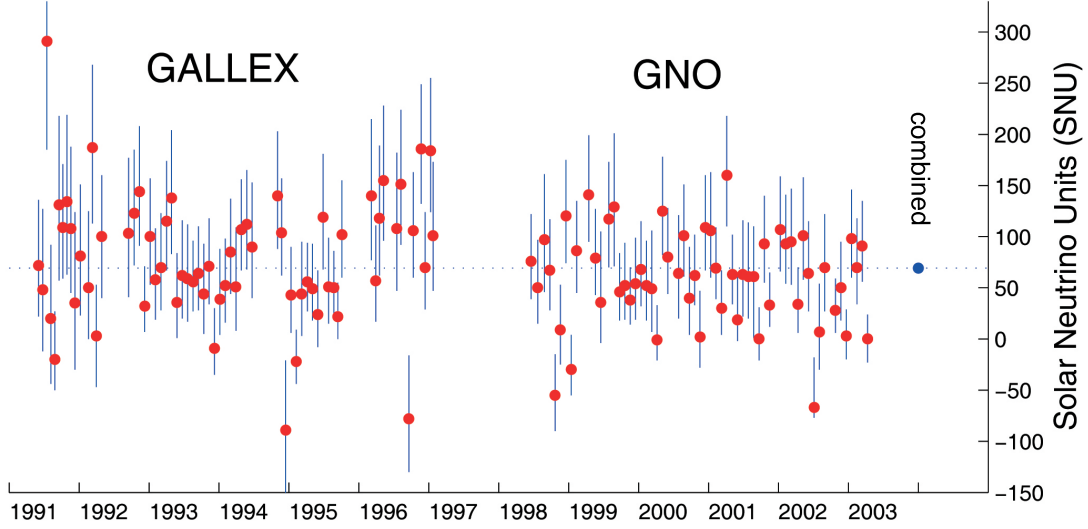
Figure 2.3: Combined GALLEX/GNO results of 3281 days (123 solar runs) of net exposure time from 1991 to 2003. The solar neutrino induced production rate is shown after subtraction of contributions due to side reactions. The error bars are 1σ. The blue point shows the combined result of 69.3±5.5SNU; the diameter of the point indicates the precision (stat. and syst. errors combined) achieved by the experiment.

obtained by GALLEX were confirmed on a higher precision level. GALLEX had shown that the energy production mechanism inside the sun is indeed nuclear fusion. Furthermore, as was already the case in the Homestake experiment, GALLEX and now also GALLEX/GNO indicated neutrino properties beyond the standard model of particle physics to account for the measured deficit. Today, the results are well in agreement with the LMA(MSW) oscillation scenario. If this oscillation solution is correct, the basic oscillation mechanism changes at a neutrino energy of about 2 MeV from the MSW matter mechanism (above 2 MeV) to the vacuum oscillation mechanism (below 2 MeV). If the ^{8}B neutrino contribution as measured by SNO [67] is subtracted from the gallium signal and the suppression factor P is calculated with respect to the BP04 SSM [68], the result is P = 0.556±0.071. Assuming vacuum oscillations, P is given by: P = 1-0.5 $\sin^2(2\theta)$. This yields θ= $35.2^{+9.8}_{-5.4}$ degrees. Although such an estimate is quite approximate, it is in good agreement with the latest determination (32.0±1.6 degrees [61]), which essentially comes from ^{8}B neutrinos (i.e. matter effects dominate). Furthermore, in addition to the dominant LMA(MSW) conversion mechanism the possible existence of a sterile neutrino and/or flavor-changing neutrino matter interactions other than the MSW effect ([69], [70], [64]) can be investigated using low-energy solar neutrinos.

24

- **Astrophysical context:** The results provided by solar neutrino gallium experiments allow to extract an upper limit of the CNO cycle contribution to the solar luminosity. The CNO-cycle (also referred to as the Bethe-Weizsäcker cycle [19]) as well as the pp-cycle lead to the fusion of four protons to Helium, however much less frequently and with the nuclei C, N, O and F acting as catalysts. It is the low energy threshold of gallium experiments that allows to gain experimental information about sub-MeV solar neutrinos (especially pp-neutrinos). The experiments are able to test the consistency of the (electromagnetic) solar luminosity with the observed neutrino fluxes. The luminosity constraint is defined by

$$L_{Sun} = \sum_i \Phi_i \cdot \alpha_i \tag{2.4}$$

where $L_{Sun} = 8.53 \cdot 10^{11} \mathrm{MeVcm}^{-2}\mathrm{s}^{-1}$ is the solar luminosity. Φ_i and α_i are, respectively, the neutrino flux and the energy release in form of electromagnetic radiation per emitted neutrino of type i (i = pp, pep, ^{7}Be, ...). This assumes that nuclear fusion reactions are the only energy production mechanism inside the sun. Apart from this basic assumption, the luminosity constraint does not depend on the solar model. The fractional CNO luminosity is defined by :

$$\frac{L_{CNO}}{L_{Sun}} = \frac{\Phi_O \cdot \alpha_O + \Phi_N \cdot \alpha_N}{\Sigma_i \cdot \alpha_i} \tag{2.5}$$

It can be calculated from the measured gallium rate

$$R^{Ga} = \sum_i \int \sigma_i(E)\phi_i(E)P(E)dE \tag{2.6}$$

where $\sigma_i(E)$ is the neutrino capture cross section on Ga, $\phi_i(E)$ is the differential flux of solar neutrinos of species i, and P(E) is the electron neutrino survival probability. The integration covers the energy interval from 233keV (energy threshold) to $\sim$20MeV. In performing this calculation the following assumptions have been made:

  - The ^{8}B electron neutrino flux, and the electron neutrino survival probabilities are measured with a precision of the order of 12% by SNO [67].

  - The ^{7}Be neutrino flux is as deduced in BP04 SSM [68], with an uncertainty of 12%. It has not yet been measured directly up to now.

– The neutrino flux ratios pep/pp and ^{13}N/^{15}O are fixed from nuclear physics and kinematics with negligible uncertainties (see [61]).

– The neutrino capture cross section (and its uncertainty) on ^{71}Ga is theoretically calculated as in [63].

With these assumptions an upper limit can be extracted from the gallium capture rate as measured by GALLEX/GNO [74]: $L_{CNO}/L_{Sun} < 6.5\%$ (3σ) (best fit: 0.8%). The result is in good agreement with the predictions of the solar models [68], L_{CNO} = 1.6±0.6%. This can be seen as a self-consistency test of the observed solar luminosity, the predicted neutrino fluxes, and the oscillation scenario. An upper limit on the CNO luminosity from all currently available solar neutrino and reactor antineutrino experimental data is discussed in more detail in [61].

To obtain the above results the ^{7}Be neutrino flux is assumed to be as predicted from the SSM, with an uncertainty of 12%. In this context the high importance of the BOREXINO [62] and/or KamLAND [73] experiments, both aimed at measuring ^{7}Be neutrinos become obvious. Once this will be done, the gallium rate will become a completely model independent test of the solar neutrino luminosity.

2.3 Motivation for Cryogenic Detectors in Gallium Experiments

In order to determine the intensities of the individual neutrino fluxes as well as a possible variation with time, the measurement of the integral solar neutrino signal on a level $\leq 4\%$ is essential. This can be viewed as the main motivation for reducing the systematic and statistical uncertainties in gallium experiments. Statistical uncertainties can be reduced by continuing gallium measurements with high target mass. Further looking at the error contributions in the overall experiment, it is quite obvious (see table 2.1) that the number of tunable parameters, i.e. sources of uncertainties are basically reduced to the detection efficiency. Here, miniaturized proportional counters exhibit an overall efficiency of 65-75%, whereas well designed low-temperature detectors have efficiencies of 98% to 100% . To understand the impact of this different detection method one can also express the gain in efficiency in terms of additional target mass: using cryogenic detectors is equivalent to a target-mass increase by 40% [65]. Due to their intrinsical physical properties cryogenic detectors seem to be the ideal candidate to replace the miniaturized proportional counters. A low energy threshold allowing detection of the M-capture at 160eV, as well as a

more efficient background rejection due to a better energy resolution and the fact that in comparison to proportional counters no escape effects are present in well designed cryo-detectors lead to a significant improvement in the detection of ^{71}Ge. Also in the case of a calibration experiment using an artificial neutrino source like ^{51}Cr in order to determine the capture cross section of ν_e on ^{71}Ga more accurately, cryogenic detectors could help. Their high detection efficiency corresponds basically to a higher neutrino source activity. The development of such a highly efficient cryogenic detection concept for a gallium experiment like GNO or SAGE is described in the following chapters.

In Ref. [32] a projection was made for the continuation of gallium experiments assuming a total gallium target mass of 90t (GNO 30t + SAGE 60t) along with cryogenic detectection exhibiting 100% efficiency. Figure 2.4 starts with the present situation of the gallium experiments: 123 solar runs from GALLEX/GNO and 121 solar runs recorded by SAGE. The combined relative statistical uncertainty of these 244 solar runs is 4.2% and the total uncertainty is 5.6%. The graph shows that after another 120 solar runs the total error could be reduced to 4.1%. This calculation was made under the assumption that the systematic error of each of these additional solar runs is decreased to ∼3.1% if cryogenic detectors with 100% detection efficiency are introduced. Thus the total systematic uncertainty would be reduced with each single solar run resulting in an overall uncertainty of 3.4% after 120 additional solar runs.

With a view to reducing the uncertainty connected to the capture cross section of ν_e on ^{71}Ga, which is crucial for the separation of the individual neutrino fluxes, man made neutrino sources have been used in GALLEX/GNO as well as in SAGE for calibration. For an efficient calibration, e.g. in GNO a ^{51}Cr source of several MCi is required. However the technical production of such high activity sources is very challenging and only realizable to a certain extent. In this context, the use of highly efficient cryodetectors would be beneficial, since it would correspond to using a neutrino source with higher nominal activity. A combination of a new detector concept for solar runs, as well as a calibration with a high activity source, then also measured with cryodetectors, could enhance the already operated gallium experiments for an extremely profitable use in future solar neutrino spectroscopy.
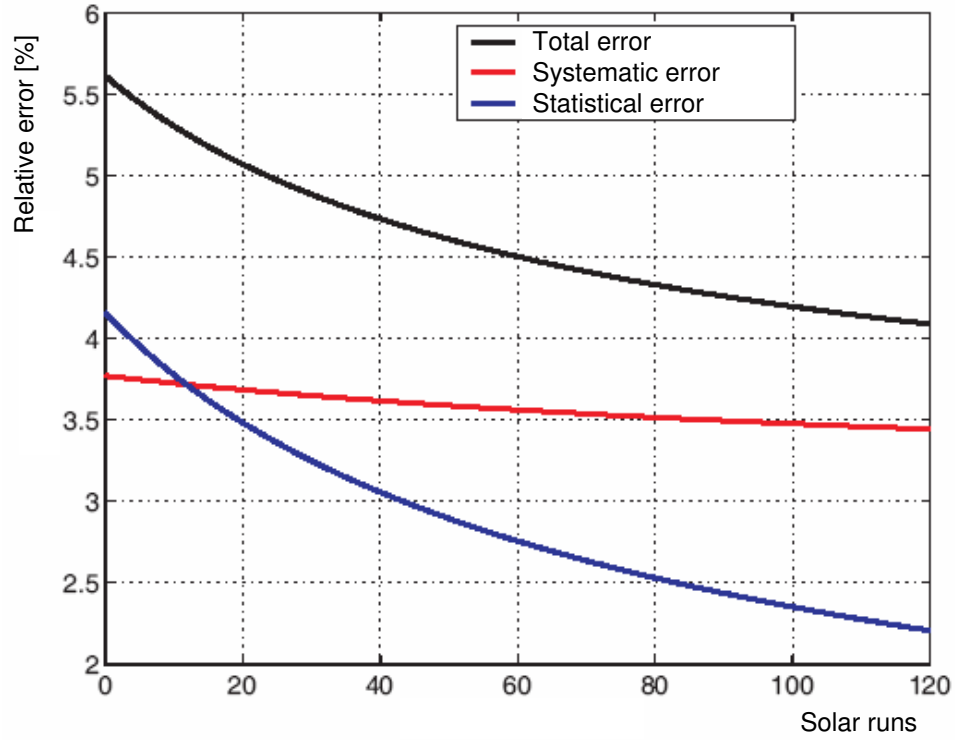
Figure 2.4: [32] Evolution of the total, systematic and statistical errors over another 120 solar runs assuming a 90t gallium target and 100% detection efficiency as achievable with cryogenic detectors.

Chapter 3

Basics of Cryogenic Detectors with Transition Edge Sensors (TESs)

3.1 Fields of Application for Cryogenic Detectors

Cryogenic detectors are a 'new' and exciting tool in atomic, nuclear, particle and astroparticle physics. Nowadays, cryogenic detectors, due to their excellent features concerning energy threshold, energy resolution, efficiency and applicability to different tasks, are employed in many fields of physics. According to the experiment they are designed for, the detectors are adapted to a special purpose, which can result in different size, mass, number or location of the devices. From tons to micro-gramms, from one to arrays of thousands, cryogenic detectors offer the possibility to achieve energy thresholds of less than 100eV and allow detection over several orders of magnitude in energy (up to several MeVs). The following list of applications gives an idea of how versatile and successful low-temperature devices have become in modern physics.

- Dark Matter Search (e.g. CRESST, EDELWEISS, CDMS)

- Determination of neutrino properties: direct neutrino mass search by means of β-endpoint analysis (e.g. using ^{187}Re), neutrinoless double-beta decay (e.g. CUORICINO, CUORE), determination of the neutrino's nature: Majorana or Dirac particle, determination of mass hierarchy as a 'by-product' of $0\nu\beta\beta$-experiments

- Solar Neutrinos: replacement of proportional counters inducing an important gain in sensitivity for radiochemical solar neutrino experiments (e.g. SAGE, GNO)

- Astrophysics, X-Ray Astronomy, IR Astronomy

- Cosmic Microwave Background (e.g. BOOMERANG [75])

- Material Science and Analysis (e.g. 'Polaris', [108])

- Metrology (absolute activity measurements) [109]

However, the basic set-up of low temperature detectors is always rather similar and will be described in the next section.

3.2 Working Principle of a Cryogenic Detector with a TES

The essential components of a cryogenic TES detector are: the absorber, that is responsible for the interaction of radiation with the detector, and a superconducting film operated in the region of transition between normal and superconducting state, which serves to produce a signal after energy absorption. In addition to that, a weak thermal coupling to a heat bath is required to allow thermal relaxation of the superconducting film. As can be understood from figure 3.1 the energy deposition in the absorber causes a temperature rise which is translated to a change in the superconducting film's resistance. The thin film can be regarded as a thermometer converting deposited energy, i.e. heat into an electrical signal.

In order to obtain an important change in resistance (ΔR) compared to a relatively small change in temperature (ΔT), the ideal transition curve of the thermometer film is steep and desirably linear between the normal and superconducting phase. Figure 3.2 shows one such model curve. The height of the signal produced by a defined energy deposition (ΔE) in the absorber, is also strongly correlated to the heat capacitiy C of the thermometer and the absorber material itself. Equation 3.1 formulates this first order approximation:

$$\Delta\text{T} = \frac{\Delta E}{C} \tag{3.1}$$

In an easy approach to describe the physics of a phase transition thermometer, one would assume an instantaneously rising and exponentially decaying temperature signal.

heat bath

electrical contacts (Al)

thermal coupling to heat bath (Au)

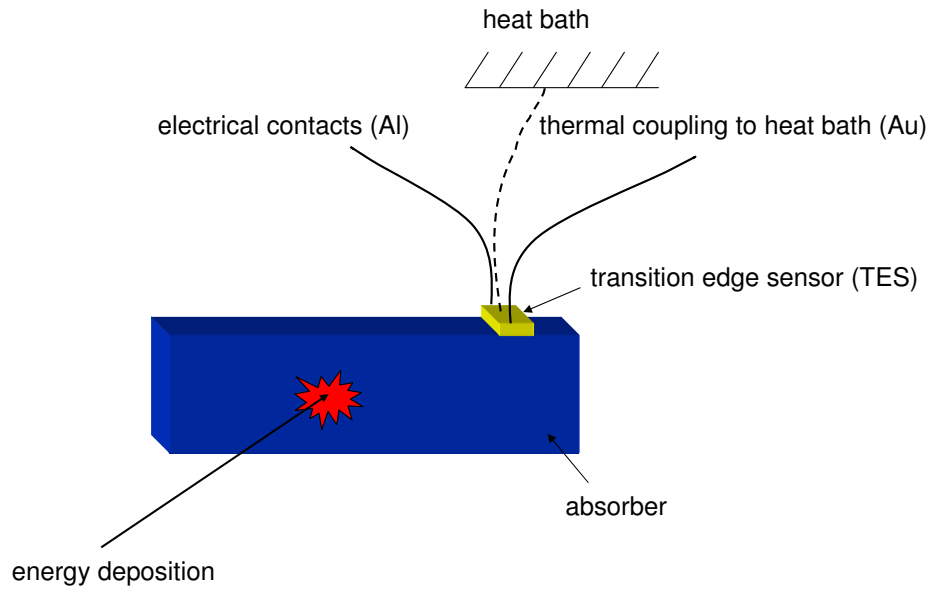transition edge sensor (TES)

absorber

energy deposition

Figure 3.1: Working principle of a cryogenic detector with a transition edge sensor TES. The energy deposition in the absorber leads to a temperature rise which is translated into a resistance change of the TES. The TES is weakly coupled to a heat bath via a gold bond wire allowing thermal relaxation of the TES.
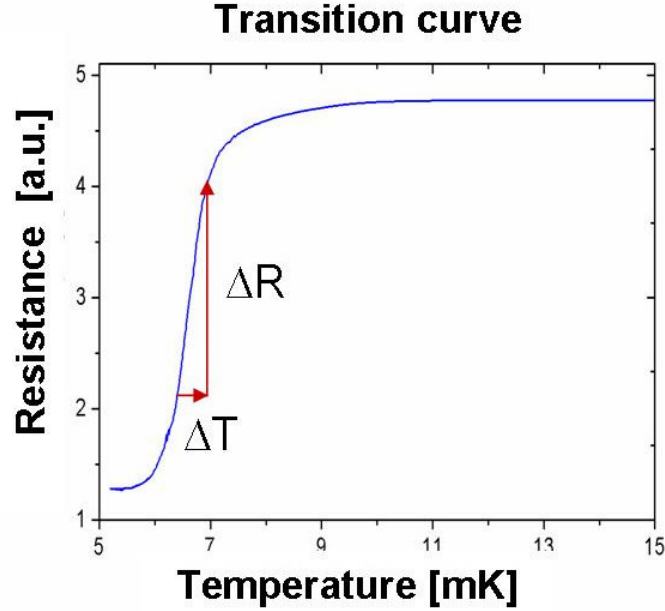
Figure 3.2: Transition curve between normal and superconducting state of the thermometer-film

The time constant τ of the decay in this picture would be defined again by the heat capacity of the thermometer and the thermal coupling G to the heat bath:

$$\tau = \frac{C}{G} \tag{3.2}$$

Analyzing real pulses as the one depicted in figure 3.3, it becomes evident that the accurate description of the signal requires a more thorough knowlegde of the physical processes occurring in the detector. An energy deposition in the absorber always creates a state far off thermal equilibrium, which results in various relaxation processes. In order to describe them properly, it is important to understand the solid state properties of the individual materials a cryogenic detector can be made of, and also their mutual thermal coupling that can sensibly influence the form of the signal. For this reason the following sections will deal with these contributions and with their physical and mathematical formulation.
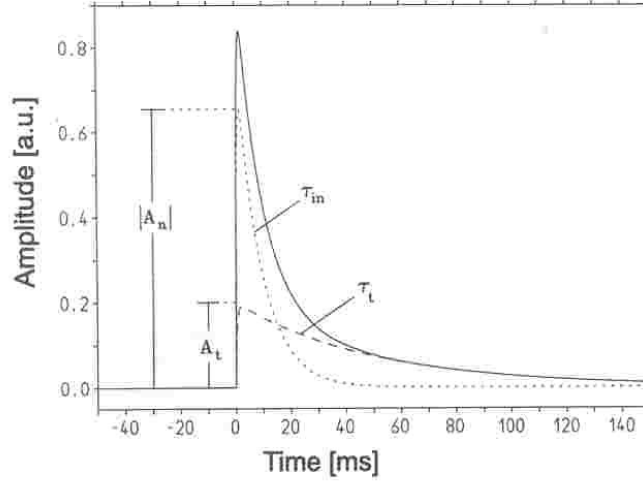
Figure 3.3: Modelled pulse of a cryogenic detector with calorimetric read out

3.3   Heat Capacities of Various Materials

In the previous section it was already made clear that the various contributions of the individual detector components to the overall heat-capacity play an important role concerning the detector's performance. The choice and the mass of the materials a detector will be made of, is crucial to achieve good energy resolution, low energy threshold or, for instance, the potential for high counting rates. In other words, the detector response to an energy deposition in the absorber and the resulting temperature signal are mainly related via the heat capacity of the total system. This is one of the reasons why the development of a new device must be planned very accurately, in order to achieve maximum sensitivity of a low temperature device for the task in question. Therefore the next passages will describe briefly the contributions of dielectrics, semiconductors, metals and superconductors to the heat-capacity.

- Dielectrics can only contribute to the heat capacity via the phonon system. This fact is reasonably well described by the Debye theory [76] which gives for the heat capacity at low temperatures ($T<<\Theta_D$):

$$C_D = \frac{12\pi^4}{5} N k_B \left(\frac{T}{\Theta_D}\right)^3 \tag{3.3}$$

33

3 Basics of Cryogenic Detectors with Transition Edge Sensors (TESs)

Where N is the number of atoms in the specimen, $k_B = 1.38 \cdot 10^{-23}$ J/K the Boltzmann constant, T the temperature and Θ_D the Debye temperature. The absence of conduction electrons explains why there is no other contribution to the heat capacity. Nevertheless, indications have been found pointing towards the existence of long-living excited states in dielectrics, especially in sapphire (Al_2O_3) [89].

- **Semiconductors** typically exhibit no electronic contribution to the heat capacity, since the working point of cryogenic detectors is normally in the order of a few mK. At these temperatures only the crystal lattice is responsible for the heat capacity.

- For metals however, the heat capacity at low temperatures is governed by the electronic contribution. In addition to that, there is also a phononic part that should be added to the heat capacity, but is virtually of no influence due to its T^3-dependence. For a free electron gas the heat capacity is given by

$$C_{el} = \frac{\pi^2}{2} N_e k_B \frac{T}{T_F} \tag{3.4}$$

where N_e is the number of electrons. T_F, the Fermi temperature, is defined by the Fermi energy $E_F = k_B T_F$. For a real metal the heat capacity may be written as the sum of electronic and lattice contributions (for T<<Θ_D and T<<T_F):

$$C = \gamma T + A T^3 \tag{3.5}$$

where γ and A are constants characteristic of the metal. For cryogenic detectors only the term $C = \gamma T$ plays a role.

- The electronic part, normally contributing to the heat capacity of a metal, varies from the normal to the superconducting state due to Cooper-pair formation of the electrons. According to the BCS theory, the electronic heat in the region of transition can be described as [76]:

$$\frac{C_{es}(T_c) - \gamma T_c}{\gamma T_c} = 1.43 \tag{3.6}$$

Where C_{es} is the electronic contribution to the heat capacity of the superconductor, γ a material constant and T_c the critical temperature of the superconductor in question. Regarding the superconducting state where the material is below the critical temperature, the heat capacity can be approximated by the following equation:

$$C_{es} = \widetilde{a}\gamma T_c e^{-\frac{\widetilde{b}T_c}{T}} \tag{3.7}$$

Where T_c is again the critical temperature of the superconducting material, γ a material constant, and $\tilde{a}$ and $\tilde{b}$ are theoretical parameters.

3.4 Phonon Excitation and Propagation in the Absorber

In the case of cryogenic detectors fabricated for the ^{71}Ge measurements described in chapter 5 and chapter 7, the main absorber made from dielectric sapphire (Al$_2$O$_3$) with a smaller semiconductor (Si) substrate bearing the TES. Both kinds of absorbers can be treated equally since their behaviour at low temperatures does not differ significantly; only their gap energies differs by $\sim$1 order of magnitude. For dielectric absorbers like sapphire, the energy gap is in the order of $\sim$10eV, for silicon it is $\sim$1eV. The absorption of radiation generates highly excited electrons, which lose their energy by transferring it to other electrons and/or electron hole pairs. For the excitation of an electron hole pair, the electron has to have an energy greater $2\epsilon_g$. Electron hole pairs excited well above the energy gap, relax to the band edge where they finally recombine. The relaxation process occurs via electron-electron interaction, via optical phonon or photon emission [77]. High energy optical phonons decay on a time scale of a few 100ps into two acoustic phonons with half the Debye frequency ω_D. The decay rate Γ_{dec} for longitiudnal acoustic phonons of a given frequency ω in an infinite isotropic medium is

$$\Gamma_{\text{dec}} = \gamma_{\text{dec}}\omega_{\text{D}}\left(\frac{\omega}{\omega_{\text{D}}}\right)^5 \tag{3.8}$$

where γ_{dec} is a material constant and ω_{D} the Debye frequency. In crystals exhibiting different isotopes, all phonon modes experience scattering at deviations from the periodic lattice. The resulting scattering rate Γ_{iso} is described by

$$\Gamma_{\text{iso}} = \omega_{\text{D}}\left(\frac{\omega}{\omega_{\text{D}}}\right)^4 \tag{3.9}$$

where η_{iso} is a material constant. The strong frequency dependence of both processes results in a rapid decay of the average phonon frequency and a slow, relatively diffuse propagation of the phonons. On a time scale of a few μs this behaviour changes drastically: a 'phonon generation' with a frequency of roughly half the Debye frequency is stable

for a few ms and their mean free path length is in the cm range, thus corresponding to the dimensions of the absorber (10x20x1mm^3)[89]. In other words, on a timescale of a few ms this non-thermal phonon population does not change significantly, the propagation of these phonons is referred to as 'ballistic'. In order to thermalize, e.g. by surface scattering would take another several ms. However, in a real detector ballistic phonons can reduce their energy by absorption in the thermometer. This process will be discussed in section 3.4.1.

In superconducting absorbers like lead, as used in measurements presented in section 7.4, the absorption of radiation breaks up Cooper pairs and produces thereby quasi particles. These quasi particles relax under emission of phonons to the band edge where again Cooper pairs can be broken up - of course only as long as the energy is greater than the energy gap Δ of the superconductor in question. After $\sim$100ps the absorbed amount of energy resides at 40% in the form of quasiparticles and at 60% in the form of sub-gap phonons [79]. The lifetime of the quasiparticles near the band edge depends mainly on the density of the quasiparticles, which, however is exponentially decreasing with temperature resulting in ms long recombination times. If the recombination energy is released by the emission of a 2Δ phonon, further Cooper pairs can be broken up again and the process repeated, resulting in long lifetimes. Impurities or lattice defects contained in the superconducter can act as regions of diminished gap energy resulting in a higher recombination probability and therefore shorter than the above mentioned lifetimes.

3.4.1 Collection Time of Non-Thermal Phonons in a TES

As mentioned in section 3.4, in a simplified model the spectral density of phonons is reduced to thermal and non-thermal phonons. After several surface reflections, the non-thermal phonons fill the crystal uniformly. The time required can be estimated from the dimensions of the crystal and the sound velocity averaged over directions and modes. This time is usually a few ms long. When high frequency phonons enter the thermometer, they are efficiently absorbed by the free electrons of the metal film forming the TES. Assuming that all phonons are absorbed in the TES, the ideal collecting time τ_0 is given by

$$\tau_0 = \left(\frac{2V_\mathrm{a}}{A_\mathrm{th} \langle v_{\mathrm{g}\perp} \alpha \rangle} \right) \tag{3.10}$$

where V_A is the volume of the absorber, A_T the surface of the TES, $v_{\mathrm{g}\perp}$ the group velocity of the phonons perpendicular to the boundary, α the transmission probability

and $\langle ... \rangle$ the average over all modes and wave vectors of the incident phonons. If only a fraction η of phonons is absorbed in the TES, then $\tau_{\text{TES}} = \tau_0 / \eta$. Using the values for α from [77] for interfaces sapphire/iridium or sapphire/gold, $\tau_0 \approx 200\mu s$ when the dimensions of $10x20x1mm^3$ for sapphire and $1x3mm^2$ for the TES area are used.

The transmission of thermal phonons across the boundary between TES and absorber leads to a Kapitza thermal conductance $G_K \propto T^3$ between thermal phonons in the absorber and the TES. The temperature of the electrons in the TES determines the resistance of the TES and therefore the resulting signal. The electrons and thermal phonons in the TES are considered as subsystems thermally coupled by $G_{\text{ep}} \propto T^5$. These processes will be described in section 3.6.

3.4.2 Phonon Signal Evolution in a Composite Detector

In the course of this work, so called composite detectors, where a TES on a silicon substrate is glued via a cryo epoxy resin to a different absorber (Al_2O_3 and Pb) have been developed and tested. Pulse analysis, especially after irradiation of a Si+TES/Al_2O_3 composite detector with a ^{57}Co source indicated two different classes of events concerning the decay time of the pulses (see figures 5.6 and 5.7). They can be attributed to events originating from the silicon absorber and the sapphire absorber, respectively. In the context of a theoretical description of low temperture detectors, it is interesting to understand the impact of the glueing spot concerning the signal (phonon) evolution. In [32] a model is presented to describe the pulse shape behaviour observed:

To the point of production of non-thermal ballistic phonons the process is as described above in section 3.4.1. However, different scenarios are conceivable in the glue spot. First, assuming that the glue spot is transparent for ballistic phonons: in this case reaching the silicon absorber corresponds to phonon transmission through two boundaries. This process can be limited by the area of the glue spot, which is not yet fully reproducible regarding its size and shape. The phonons can be reflected and reenter the sapphire absorber only progressively thermalizing in the thermometer. According to the strength of coupling, i.e. the size of the glue spot, this process can vary and result in longer or shorter decay times of the signal produced.

In a second scenario, the glue spot can be regarded as a 'thermal bottleneck', in which the ballistic phonons produced in the sapphire absorber already thermalize in the cryo resin layer and thereby heat up the silicon substrate in a secondary effect, so that the eventual thermalization in the thermometer is delayed compared to a TES directly evaporated onto sapphire. It is highly probable that an overlap of both scenarios is the case for composite

detectors.

3.5 Thermal Coupling to the Heat Bath

The thermal coupling between TES and heat sink determines how fast energy can flow from the detector to the heat sink. The detectors used in this work were all coupled to the heat sink (base temperature of $\sim$10mK of a ^{3}He/^{4}He dilution refrigerator) via a 25μm thick gold bond wire. The gold wire is ultrasonically welded onto the structurized Ir/Au layer to allow its thermal relaxation after energy absorption. The strength of thermal coupling is ideally given by the length, diameter and temperature of the bonding wire following the Wiedemann Franz law, relating electric resistance R with thermal conductance G:

$$G = \frac{LT}{R} \tag{3.11}$$

where L is the Lorenz number and T the temperature. The bondpoint is realized in the middle of the TES to avoid effects due to non-uniform thermal conductance along the thermometer film.

3.6 Calorimetric Model of a Cryogenic Detector

The detector response, in this case meaning all relaxation-mechanisms in terms of solid state physics after the absorption of energy in form of particle or wavelike radiation is of great importance when designing a cryogenic detector. The theoretical understanding of cryogenic calorimeters is based on a model description first published by Pröbst et al.[77]. It accounts for the thermal couplings inside the calorimeter and the energy flow and relaxation processes.

A scheme of all components relevant for the thermal processes occurring in the calorimeter is depicted in figure 3.4. The model describes the detector as a system of thermally coupled subsystems: The phonon system of the absorber crystal, the phonon system of the superconducting thermometer film, the electron system of the superconducting thermometer film, a heat sink (heat bath) with infinite thermal capacity and distinct thermal couplings between these components. In this discussion the absorber crystal is treated as dielectric with only the phonon system carrying thermal energy. The discussion can be extended to other absorber materials [78]. The phonon system of the absorber crystal has the temperature T_a and the heat capacity C_a. It couples thermally to the phonon
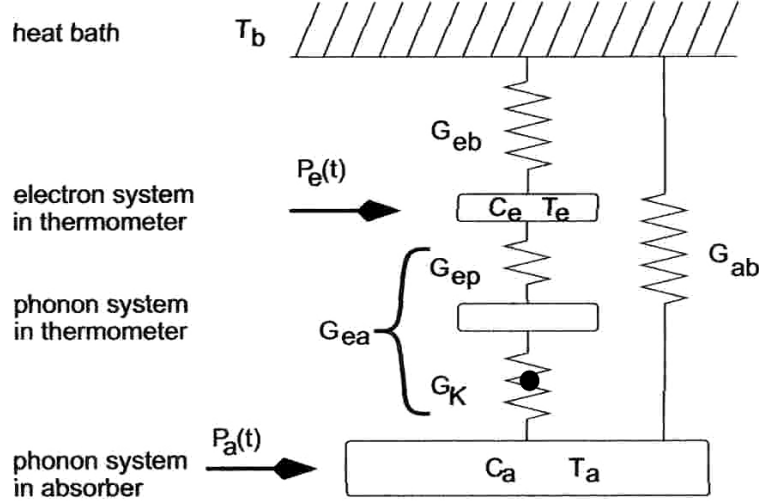
Figure 3.4: Calorimetric model of a cryogenic detector [77]. The black spot represents the glue spot in composite detectors.

system of the superconducting film, evaporated onto it with the Kapitza coupling G_K. For composite detectors like the ones developed for GNO in this work, the 'glue spot' and also the interface between deposited germanium and sapphire represent further components that have to be added to the Kapitza coupling as is depicted in figure 3.4. Via the mechanical mounting of the detector, the absorber crystal is also coupled directly to the heat bath by a parasitic coupling G_{ab} (see figure 3.4). The phonon system of the TES film is coupled to the electron system by the electron-phonon coupling G_{ep}. Since the heat capacity of the phonon system in the thermometer is very small compared to C_a and the heat capacitiy of the electron system C_e in the interesting temperature range, it can be neglected. The coupling of the absorber crystal to the electron system in the superconducting thermometer film is given as:

$$G_{ea} = \left(\frac{1}{G_K} + \frac{1}{G_{ep}} \right)^{-1} \tag{3.12}$$

The electron system of the thermometer has the temperature T_e. It is directly connected to the heat sink at the temperature T_b by the thermal coupling G_{eb}. An energy deposition ΔE in the absorber crystal creates high-energetic non-thermal optical phonons. They decay by inelastic scattering processes as described in section 3.4. On the timescale of interest of $\leq 100 \mu s$ the mean phonon frequency in an absorber like sapphire, which was used in this work, is still above 600GHz and the phonons are not thermalized. These

non-thermal phonons are effectively absorbed by the free electrons of the thermometer film causing a power flow $P_e(t)$ into the film. By this process the phonon density decays exponentially as does $P_e(t)$. Additionally, concurring inelastic phonon decay is likely to happen in the absorber crystal. It causes the energy of the non-thermal phonons to be thermalized, leading to a power flow $P_a(t)$ into the absorber. A fraction ϵ of the initial energy is deposited in the thermometer film, a fraction $(1-\epsilon)$ in the absorber crystal. $P_e(t)$ and $P_a(t)$ can then be written as

$$P_e(t) = \Theta(t)P_0 \exp \frac{-t}{\tau_n} \tag{3.13}$$

$$P_a(t) = \frac{1-\epsilon}{\epsilon} P_e(t) \tag{3.14}$$

with the step-function $\Theta(t)$, the time constant for the decay of non-thermal phonons τ_n and the initial power (with ΔE being the total energy deposited in the absorber)

$$P_0(t) = \frac{\epsilon \Delta E}{\tau_n} \tag{3.15}$$

The life time of the population of the non-thermal phonons is given by

$$\tau_n = \left(\frac{1}{\tau_{film}} + \frac{1}{\tau_{absorber}} \right)^{-1} \tag{3.16}$$

where τ_{film} is the phonon collection time of the thermometer film and $\tau_{absorber}$ is the life time of non-thermal phonons in the absorber without a thermometer film attached. In clean absorbers, $\tau_{absorber}$ is dominated by surface scattering. After a few of these reflections the non-thermal phonons fill the absorber uniformly.

The thermodynamic system depicted in figure 3.4 can be described by two coupled differential equations, where T_e is the temperature of the electron system and T_a the temperature of the phonon system of the absorber:

$$C_e \frac{dT_e}{dt} + (T_e - T_a)G_{ea} + (T_e - T_b)G_{eb} = P_e(t) \tag{3.17}$$

$$C_a \frac{dT_a}{dt} + (T_e - T_a)G_{ea} + (T_e - T_b)G_{ab} = P_a(t) \tag{3.18}$$

With the initial condition $T_a(t \leq t_0) = T_e(t \leq t_0) = T_b$, the thermometer signal $\Delta T_e = T_e(t) - T_b$ is given by the solution

$$\Delta T_e = \Theta(t - t_0) \left[A_n \left(e^{-\frac{t-t_0}{\tau_{in}}} - e^{-\frac{t-t_0}{\tau_n}} \right) + A_t \left(e^{-\frac{t-t_0}{\tau_t}} - e^{-\frac{t-t_0}{\tau_n}} \right) \right] \tag{3.19}$$

with the time constants

$$\tau_{in} = \frac{1}{\nu_{in}} = \frac{2}{a + \sqrt{a^2 - 4b}} \tag{3.20}$$

$$\tau_t = \frac{1}{\nu_t} = \frac{2}{a - \sqrt{a^2 - 4b}} \tag{3.21}$$

$$a = \frac{G_{ea} + G_{eb}}{C_e} + \frac{G_{ea} + G_{ab}}{C_a} \tag{3.22}$$

$$b = \frac{G_{ea}G_{eb} + G_{ea}G_{ab} + G_{eb}G_{ab}}{C_e C_a} \tag{3.23}$$

and the amplitudes

$$A_n = \frac{P_0 \left(\nu_{in} - \frac{G_{ab}}{C_a} \right)}{\epsilon \left(\nu_{in} - \nu_t \right) \left(\nu_n - \nu_{in} \right)} \left(\frac{\nu_t - \frac{G_{ab}}{C_a}}{G_{eb} - \frac{C_e}{C_a} G_{ab}} - \frac{\epsilon}{C_e} \right) \tag{3.24}$$

$$A_t = \frac{P_0 \left(\nu_t - \frac{G_{ab}}{C_a} \right)}{\epsilon \left(\nu_{in} - \nu_t \right) \left(\nu_n - \nu_t \right)} \left(\frac{\nu_{in} - \frac{G_{ab}}{C_a}}{G_{eb} - \frac{C_e}{C_a} G_{ab}} - \frac{\epsilon}{C_e} \right) \tag{3.25}$$

τ_{in} and τ_t are time constants of the homogeneous equations. τ_t is the life time of the non-thermal phonon population introduced by $P_e(t)$ and $P_a(t)$ and $\nu_n = \tau_n^{-1}$. In the case that $C_e \ll C_a$ the equations simplify and the physical relevance of τ_{in} and τ_t becomes more evident:

$$\tau_{in} \approx \frac{1}{a} \approx \frac{C_e}{G_{ea} + G_{eb}} \tag{3.26}$$

$$\tau_t \approx \frac{a}{b} = \frac{C_a}{\frac{G_{eb}G_{ea}}{G_{eb} + G_{ea}} + G_{ab}} \tag{3.27}$$

Now it can be seen more obviously that τ_{in} represents the intrinsic time constant of the electron system of the thermometer and is responsible for carrying heat out of the electron system via its temperature gradient to the environment. τ_t is the time constant of the

thermal relaxation of the phonon system of the absorber through all its thermal couplings. If the time constant for the decay of non thermal phonons $\tau_n \ll \tau_{in}$, the electron system is quickly heated up by non-thermal phonons. Its temperature relaxes slowlier (with time constant τ_{in} to the heat bath and the absorber crystal. On the longer scale of τ_t the absorber crystal and the thermometer film equilibrate to the temperature of the heat bath. The amplitude of the non-thermal component A_n measures the total absorbed heat. This operating mode is the 'calorimetric mode'. The signal rise time of the calorimeter is given by the life time of non-thermal phonons $\tau_n \approx \tau_{film}$ of equation 3.16, where τ_{film} is the phonon collection time of the thermometer film and $\tau_{absorber} \gg \tau_{film}$. In the case $\tau_n \gg \tau_{in}$ the detector is operated in the 'bolometric mode' and the signal rise time is given by τ_{in}. The detectors produced and measured in this work were operated as calorimeters.

3.7 Example: Iridium-Gold Transition Edge Sensors

The thermometer film of a calorimeter as described in the section above is the heart and therefore the most vital part of such a low-temperature device. All cryogenic detectors featured in this thesis are based on iridium-gold-bilayers used as Transition Edge Sensors (=TES). The great advantage offered by 'metal-sandwiches' made of a normal and a superconductor is their adjustability to a given physical environment or purpose. Defined for instance by the base temperature or cooling power of a cryostat, the size of the detector itself, aspects concerning radiopurity, or other issues influencing the detector's performance, a tunable critical temperature via the proximity effect discussed in section 3.7.1 is of tremendous advantage.

It has to be considered that the production of such thin layers, however trivial they may seem, can severely affect the overall performance of the detector. Reproducibility of the form and temperature of the phase transition region are of the utmost importance if devices of that kind are to be operated for instance in arrays (e.g. CRESST, CUORICINO) or on long time-scales. All TES produced and measured in this work had a size of at most $3mm^2$ and had an average thickness of $\sim 1000\mathring{A}$. The operation points of the films discussed here lay in the region between 10mK and 100mK. The TESs in this work were used under various circumstances and proved, in most cases, excellent performance according to the individual task. Some to a level that a use as sensors for β-endpoint measurements and thus determination of neutrino mass limits would be conceivable. Also other new 'cutting-edge' applications appear to be at hand.

3.7.1 Proximity Effect in Iridium-Gold Bilayers

The production of proximity-effect transition edge sensors requires the use of Ultra High Vacuum systems (=UHV), in which a selection of metals, like iridium and gold can be evaporated for instance using an electron gun. If the thin film deposition technique is well understood, it is possible to (re)produce a bilayer of iridium and gold. The normal conductor, in this case gold, will affect the superconducting properties of the iridium layer in such a way that the critical temperature of the whole film (Ir and Au) is lowered to a certain amount. There are several models that describe this behaviour by considering mainly functions of the respective thicknesses of the layers [80]. However, those models have their limits since they can only account for ideal thin films, not always achievable in reality.
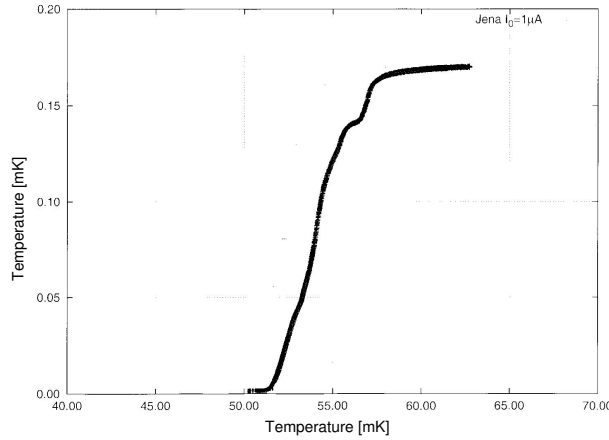
Figure 3.5: Example of a bad transition (si492a). The curve is not smooth over the whole transition width. As a consequence, non-linear detector behaviour as well as problematic working point stabilization can result.

Figure 3.6 depicts a measured transition curve which showed satisfactory behaviour, in comparison to that of figure 3.5, which exhibits 'bumps' and virtually no linearity at all. An explanation for this 'ugly' behaviour could be a wrongly chosen substrate temperature during the gold evaporation. Gold demonstrates a tendency to clusterize very rapidly, which leads to the conclusion that a higher surface energy is desirable when depositing gold onto the adhesion layer. The substrate heating in both cases differed by 50°C; the higher substrate temperature during evaporation leading to the better result. But also other factors can affect the behaviour of an iridium-gold-film. The use of cryogenic
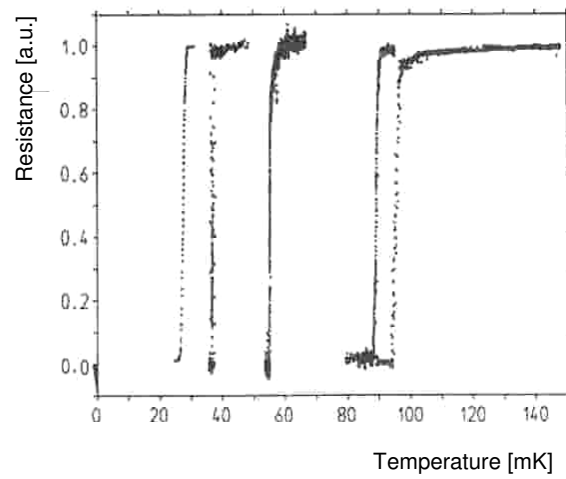
Figure 3.6: Examples of good transition curves [89].

detectors in GNO would have required thermal deposition of ^{71}Ge in the vicinity of the TES. Tests have been performed several times, always leading to the same conclusion: if exposed to high temperatures or temperature gradients the superconducting bilayer will suffer deterioration or more likely destruction of its desired properties. To avoid this problem, we developed a special method where the TES is produced separately on a silicon absorber and then attached by glueing to a sapphire absorber onto which the thermal vapour deposition has already been carried out. This procedure and its applicability to other tasks is described more accurately in section 5, 7 and 8.

3.7.2 Electronic Read-Out Circuit for a TES

A typical read-out circuit for transition edge sensors is shown in figure 3.7. The main components are: a reference resistor R_s, called 'shunt' resistor, an induction coil L_s with the thermometer resistance R_{th} in series and a SQUID (=Superconducting QUantum Interference Device). This circuit is biased by a constant current I_0 that splits into the two branches of the circuit in proportion to the value of the resistance of the individual branch.

$$I_t = \frac{I_0 R_s}{(R_s + R_t(T, I_t))} \tag{3.28}$$

If the resistance of the TES varies, the resulting change in current induces a change of the magnetic field that is then measured by the SQUID. It is the ratio of the shunt resistor R_s and the thermometer's resistance R_{th} that mainly determines whether the TES is in the so called current or voltage biased mode. In the case of this work, all TES were voltage biased since our shunt resistors R_s were of $\sim$10mΩ and the TES in the 1-5Ω range, i.e. if R_s<<R_{th}, then $I_{th} \approx \frac{I_0 R_s}{R_{th}} = \frac{U_s}{R_{th}}$ and therefore U_s=const.

The integration of this TES-SQUID read-out circuit into the overall data acquisition system is described in detail in section 7.1.2.
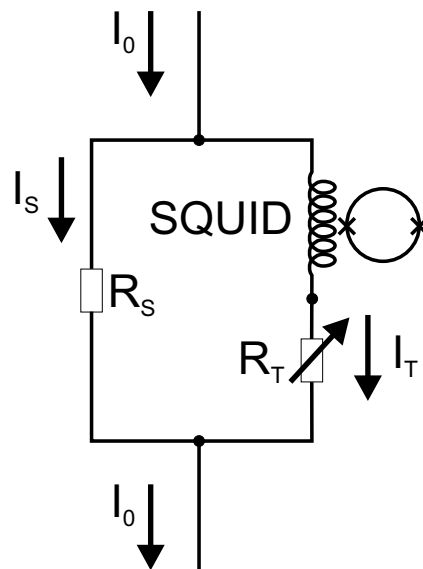
Figure 3.7: SQUID read out circuit

Chapter 4

Fabrication and Processing of Transition Edge Sensors (TESs)

4.1 Iridium-Gold Evaporation System

Most detectors featured in this work are based on iridium-gold phase transition ther-mometers, which are produced at our institute in Garching. The iridium-gold films are evaporated in an ultra high vacuum system (UHV) that reaches a final pressure of typ-ically $\sim$5x10^{-10}mbar. The system consists of two chambers separated by a gate-valve. The main chamber is used for the evaporation process itself, whereas a smaller crosslike recipient acts as a transfer chamber in order not to break the vacuum for every new thin film deposition. This prechamber, due to its small volume, can be pumped quite rapidly using a small turbo-molecular pump (Fa.VARIAN 696-9007). The main recip-ient is equipped with heating-bands that can reach temperatures up to 300°C serving to bake out the system in order to get rid of gas-atoms or molecules stuck in the walls or other parts of the chamber thus severely affecting the quality of the final pressure and hence the quality of the vacuum. The normal bake out procedure is performed at $\sim$180°C for 2-3 hours and is usually done after replacing evaporation material or for maintenance work. The overall system is pumped constantly by a turbo-molecular pump (Fa. PFEIFFER,TMU520). During evaporation a titanium-sublimation pump can be added to remove mainly hydrogen molecules very effectively. In addition to that the bell-like main chamber (height:$\sim$70cm, diameter:$\sim$30cm) has a so called nitrogen-shroud only filled with liquid nitrogen during the evaporation process. The cold surface on the inner side of the recipient acts as a 'cryopump' which very effectively adsorbs remaining atoms and molecules during the deposition process, resulting in pressures in the region of $\sim$10^{-11}mbar, a prerequisite for excellent and reproducible thin films. In order to monitor

the quality of the vacuum and the nature of remaining atoms and molecules, the system is further equipped with a mass spectrometer (Fa. INFICON QUADREX 200). To avoid undesired contaminations, the system is only used for the deposition of iridium and gold. The evaporation is performed with an electron-gun with which the iridium and gold targets, located in carbon-crucibles are heated up. The substrates to be evaporated are at a distance of ∼150mm from the iridium-gold-targets and can be heated up to temperatures of 700°C by a Boron-Nitride-Heater, which is regulated by a temperature control device (EUROTHERM). The maximum substrate size is ∼51mm corresponding to a common 2"-wafer used in the semiconductor industry. The substrate holder can be modified quickly in order to accommodate a great variety of substrate forms and sizes, simply by using different supports in the main 2"-holder. Most parts inside the system are made of tantalum which is one of the ideal materials to be used in UHV-systems since its physical properties are such that it does not 'gas out', exhibiting in addition very good features concerning rigidity, stability and maintainability. It is of great importance to know as precisely as possible the thicknesses of the deposited thin layers of iridium and gold. This is done using a resonant crystal read-out by a thin-film deposition monitor (Fa. INTELLEMET-RICS IL-820) that measures the thickness as well as the deposition rate of the evaporated material. A tantalum shutter allows regulation of the desired rate of the material to be evaporated, prior to the deposition onto the substrate. The evaporation material is produced by MATECK. The purity of gold is of 99.999%, whereas the iridium has a nominal purity of 99.95% out of which a single crystal is produced that, in principle, ought to have a higher purity than the polycrystalline metal. However, it is not quantified by MATECK.

The detectors measured in this work were produced according to the following procedure:

- The first important step in producing an iridium-gold bilayer is the evaporation of a 'cover'-layer of iridium that commonly has a thickness of $50\mathring{A}$. Past experience has proved that this layer guarantees on the one hand good adhesion of the following main iridium-gold-bilayer to the substrate's surface, and on the other hand it burries unwanted impurities or microscopic 'dirt' underneath. This iridium-layer is evaporated at a temperature of 300°C; at lower temperatures iridium or gold would not stick to the surface layer. The rate during the deposition of this first layer is of ∼0.3 $\mathring{A}$/s.

- After evaporation of the first iridium layer the temperature of the substrate(s) is ramped down to 150°C, which is the temperature required to deposit the second layer, gold. The typical rate at which gold is deposited is of ∼1.3-1.4$\mathring{A}$/s. Due

to its normal-conducting behaviour at low temperatures, gold lowers the transition temperature of a superconductor such as iridium via the 'proximity-effect' [80] described in section 3.7.1 Current experience has shown that the temperature chosen for the gold-layer evaporation is a crucial parameter. Gold was deposited by other experimentalists in our group at a temperature of 100°C: the transition curves exhibited bumps (see figure 3.5) leading to an extremely unlinear or uncontrolable behaviour of the detector and virtually no reproducibility at all. Of course such an unlinear transition slope can have various reasons, nevertheless the quality of a film evaporated then at 150°C showed again the desired smooth and thus rather linear behaviour. Apparently, gold atoms tend to form clusters if their kinetic energy on the surface during film growth is not sufficient, leading to undesired effects in the production of proximity bilayers.

- The last layer, iridium, is evaporated at room temperature, i.e. at $\sim$20-30°C. This, later superconducting part of the film, is again deposited at a rate of $\sim$0.3$\mathring{A}$/s. The typical thickness of this iridium layer is of the order of 300$\mathring{A}$.

All films produced in the above mentioned system, are named according to the substrate they are grown on, the substrate position with respect to the crystal resonator and by a consecutive number.

4.2 Cleaning of Substrates

The cleaning of substrates is normally performed prior and after the thin-film deposition. There are several ways of cleansing substrates depending on the substrate type and also on the type of thin film to be evaporated. In the case of this work, only silicon or sapphire substrates were used.

The cleanroom procedure is the following:

- The substrates are immerged in an aceton filled glass container that is placed in an ultrasonic bath for $\sim$10min.

- The substrates are then mounted onto a spinner revolving at 3000rpm.

- Again drops of ultrapure aceton (Fa. MERCK) are repeatedly poured onto the spinning substrate.

- The same procedure is then performed with methanol.

- Inbetween the methanol or aceton covered substrate is flushed with nitrogen gas, in order to get rid of microscopic dust particles.

Past experience has shown that if substrates are still inside their packages on arrival, direct introduction into the evaporation system can be performed, since the industrial production is very clean and allows direct thin film deposition with good results (see section 4.5.4).
In the case of superconducting monolayers (e.g. tungsten) as TES like in CRESST, a further cleaning has to be performed since residual magnetic impurities in the order of a part per million (ppm) can affect the critical temperature shifting the superconducting transition by 1mK to 10mK [81]. Here, a cleaning prior to evaporation is obligatory. It is done using a combination of H_3PO_4 and $HCl+HNO_3$ (aqua regia) removing surface contamination of Fe and Ni by more than an order of magnitude [81].

4.3   Photolithography and Structurization of the TES

After removing the evaporated substrates from the iridium-gold deposition system further treatment of the detectors-to-be is realized in a clean room (actual dust particle concentration 1000-2000 measured by monitor, cleanroom class 10000). In order to obtain a desired pattern out of the iridium-gold film, positive 'photolithography' is necessary. The process comprises the following steps:

- Photoresist has to be applied as thin and homogeneously as possible onto the evaporated film. This is done by rotating the substrate in a spinner at ∼1000rpm. Careful attention has to be given not to include microscopic dust particles on or in the liquid photoresist, since it can severely affect the desired structures, especially if they are in the μm range.

- After briefly having checked the quality of the applied photoresist under a microscope, the substrate is placed on a heating plate at 100°C for 5min, to bake the photosensitive layer for further processing.

- The exposure to ultra-violet light is performed in a mask-aligner (Fa. KARL SÜSS) using the hard contact mode and an exposure time of 30s ('soft' mode).

- The structure created in the photoresist is subsequently developed (ma-D330, Fa. MICRORESIST) for ∼30sec, or sometimes more, depending on the thickness of the photolithographic layer and the obtained result as judged by eye or microscope.

- Finally the substrate is cleansed for a couple of minutes with deionized and purified water (Fa. Millipore).

After termination of the cleanroom processes, the substrate is transferred again to the evaporation laboratory, where it is placed in an Ar-sputtering system for the eventual structurization of the iridium-gold film. The recipient is pumped to a pressure of $5x10^{-5}$mbar using a cryogenic adsorption pump that allows rapid and efficient pumping (∼10min). The subsequent argon atmosphere is auto-regulated at $3.2x10^{-4}$mbar. The typical acceleration voltage for Ar-ion-etching is 650V, whereas the ion current is ∼25mA. After setting the above mentioned values, it is recommended to wait until the 'Kaufmann-source' has reached stable operating condition (quite important changes in the ion current are likely to occur during the first minutes of operation, then it remains constant for most of the sputtering time). The substrate, which is mounted on a water-cooled copper target and additionally contacted with thermal paste, is only exposed to the argon plasma once a tantalum shutter is opened manually. The exposure time to the plasma is of the order of 15min to 20min depending on the thickness of the evaporated film. Most detectors in this work had to be etched for 18min. Over-exposures should be avoided, since the photoresist covering the structure to remain can not indefinitely resist the ion-bombardment. The result can be undesired deterioration of the film, which can easily generate problems concerning reproduction of a certain kind of detector. A mirror allowing direct view on the substrate's surface is a simple, but efficient tool to determine the right exposure time to the Ar plasma. If the detector in question requires a gold bond pad for more defined thermal contact or additional Al contact stripes etc., the sputtering system can also be operated in such a way that the argon plasma is used to detach e.g. Au atoms out of a desired target (the following targets are available for this system: Au, Ag, Al_2O_3, Ti, Nb, plus a variety of different metal alloys and insulators). If such a structure is needed, a so called negative photoresist structure has to be applied again on the substrate. The procedure (for which the substrate is taken back to the cleanroom) is the following:

- Application of negative photoresist (ma-N440; Fa. MICRORESIST) with a spinner rotating at 3000rpm for a duration of 30s.

- Bake out of the photoresist on a heating-plate for ∼5min at 100°C.

- UV-light exposure for 120s in the 'hard-contact' mode of the above mentioned mask-aligner.

- Development of the photolithographic structure for 60s (Developer: ma-D332S, Fa. MICRORESIST).

- Cleansing the substrate with deionized and purified water.

4.4 Thermal and Electrical Contacting

After termination of the cleanroom processes the detector has to be mounted in its holder and must be contacted thermally as well as electrically. Both types of contacts are effectuated with an ultrasonic bonding machine (Fa. Kulicke und Soffa). The electrical contacting of the TES is realized via 4 aluminium bond wires (Fa. Müller Feindraht) of 25 μm diameter. In principle 2 wires bonded at the two extremities of the TES would be sufficient; however experience has proved that doubling the wiring is advantageous since mounting the detector in the cryostat often causes bond wires to go off. Also during the cool down procedure bonding wires tend to go off leaving the detector uncontacted. Due to the fact that the electrical bonding wires are made of aluminium, which becomes superconducting at 1.14K, no parasitary heat capacity is introduced in the detector if bonded twice.

The thermal link to the heat bath (see section 3.5 for theoretical description), which in this case is the 'infinite' cooling power of a cryostat is realized via a gold bond wire of 25μm diameter. The gold bond wire was always attached in the middle of the thermometer in order to cool the TES as homogeneously as possible. Sometimes a gold bond pad can be used for easier bonding and more defined thermal contact. The gold bond wire most of the time is not bonded twice since it is normal conducting in the mK range and therefore contributes to the overall heat capacity of the detector. In the case of GNO detectors where redundancy plays an important role, the TES for the measurement described in section 7 both detectors were double bonded.

4.5 Construction and Design of a Magnetron Sputtering System for Low Temperature Detector Production

4.5.1 Motivation

Our institute has been equipped with a common 'Kaufmannquelle'-based sputtering system that was custom built, in order to provide a flexible system for the production of a broad variety of low-temperature and other devices. This system offers a great number of targets and mounting possibilities of the substrates. Unfortunately the use of many different materials inside such a vacuum system, leads to uncontrolable impurities in terms of material and radiopurity. For most applications, except magnetic impurities, this fact is of no relevance, but can, however, severly affect the performance of low-temperature detectors, designed for a defined low-background environment (e.g. in CRESST). Since present scientific involvement in experiments like CRESST, GNO or upcoming $0\nu\beta\beta$-experiments demand extremely low background, radiopurity is an overall important issue to consider. In order to control radiopurity to the best level achievable, it is necessary to establish an extremely clean production method of the detectors. This can for instance be guaranteed if a system is only equipped or filled with materials of determined radiopurity. Additionally, magnetron sputtering has become a state of the art technique for thin-film deposition and might even be used to produce Ir/Au proximity effect TESs. In this case all production processes necessary to fabricate a TES for a cryogenic detector could be performed in one single system.

4.5.2 Magnetron Sputtering

Observations of the phenomenon called sputtering, go back over one hundred years to early experiments which introduced electricity into a reduced pressure atmosphere [82]. Today, the inert gas argon is used to act as the sputtering medium, because it is a heavy noble gas with a low ionization potential and is plentiful. Furthermore, the inert nature of argon inhibits compounds from being formed at the target's surface. Target and cathode, which in the case of magnetron sputtering are identical, are bombarded by argon atoms progressively removing material from the target's surface e.g. Au, Ir, Si etc. When the ions strike the target, their primary electrical charge is neutralized and they return to the process as atoms. Once sputtered, the target atoms travel until they reach the substrate. The argon plasma however is confined by the magnetic field of the cathode. According

to the R.F. power input and the distance cathode-substrate, a thin film is growing at a desired rate on the substrate's surface influenced by such things as material, temperature and plasma structure.

Figure 4.1 depicts schematically the principle of planar magnetron sputtering. In the case of the realized system described in section 4.5.3 the substrate and the cathode are mounted upside down, i.e. the cathode is on the bottom and the target above.
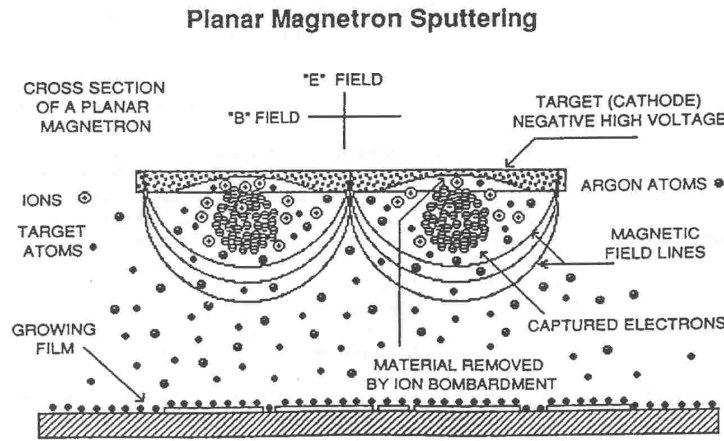

Figure 4.1: Planar magnetron sputtering principle [85]

To operate magnetron sputtering cathodes (e.g. Mighty MAK-Series) a vacuum system must be available. This system has to be pumped with a high-vacuum pump of the turbo or cryo type to achieve pressures in the 10^{-4}mbar range during sputtering, and in the 10^{-9}mbar range during presputter pump down. A suitable fixture for mounting and holding the substrate(s) during film deposition should be provided, in conjunction with a means of shuttering the source (target) from the substrate during precleaning of the target. To obtain ideal uniformity, the distance from source to substrate should be adjustable. The rate will decrease by the square of the distance between source and substrate, however, uniformity will be enhanced as this distance is increased.
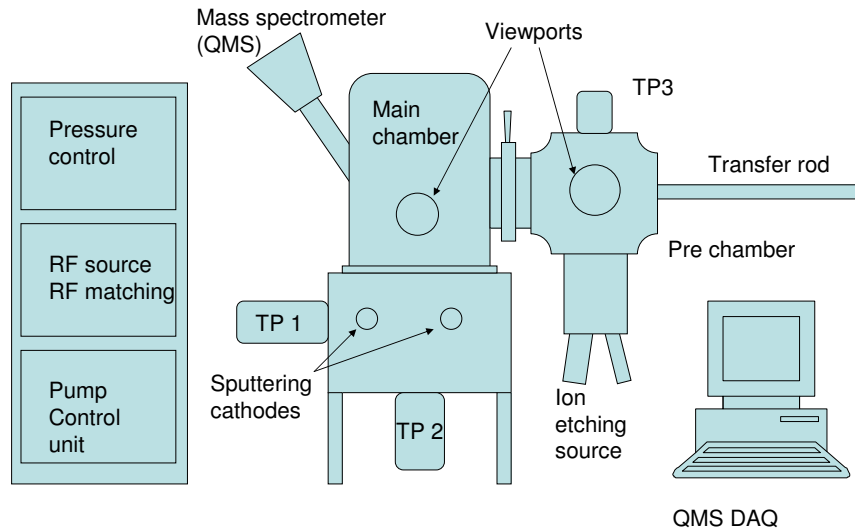
54

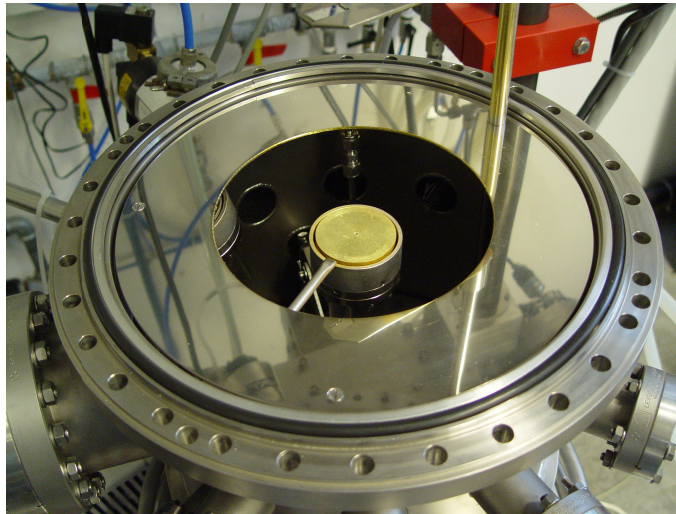Figure 4.2: Schematic drawing of the new magnetron sputtering

Figure 4.3: Picture of the opened main chamber equipped with 3 sputtering cathodes. In the picture only one magnetron cathode equipped with a gold target is visible.

4.5.3   Setup of the System

Figure 4.2 depicts the schematic setup of the newly built magnetron sputtering system located in the 'Physik II' building in Garching; figure 4.3 and 4.4 show the realized apparatus. The system can be divided into three main parts: the main evaporation chamber, the prechamber and the electronic and mechanical periphery. The following paragraphs will describe them in detail:

- **The main chamber** consists of a cylindrical recipient (diameter: $\sim$30cm, height: $\sim$90cm) that can be opened 'in the middle' in order to gain access to the interior of the evaporation chamber e.g. to change targets, for cleaning or for maintenance work. The main chamber is equipped with a viewport (diameter: 10cm) to allow surveillance of the evaporation process.
  The upper recipient of the main chamber including a mass spectrometer and its pumping unit as well as the prechamber and the transfer manipulator can be moved with a crane. For stability reasons the whole upper part of the system is mounted on a two-rail fixture that is attached to the floor and the ceiling of the laboratory as can be seen in figure 4.4. The lower part of the recipient is mounted on an iron chassis which is attached to the floor and also accomodates two rotary-pumps and one turbomolecular pump. To the left of the lower recipient a second turbomolecular pump (Fa. Balzers, TMH 180) is mounted for constant pumping of the main chamber. The lower turbomolecular pump (Fa. Leybold NT450) can be added via a gate-valve separating it from the recipient. Normally the second turbo pump is only added during sputtering to handle the higher pressures in the system due to the argon plasma of $\sim$3.2x10^{-4} mbar. Under normal conditions i.e. the lower pump is detached from the recipient, the system reaches a typical pressure of 6-9x10^{-9}mbar after 48h of pumping without heating out the recipient. The pressure in the main chamber can be monitored with a thermocouple gauge for coarse vacuum and an ion gauge for fine to ultra high vacuum, both are located at the backside of the system. The ion gauge also facilitates the ignition of the argon plasma without increasing the RF source's power too much since it can act like a spark and start the plasma. At the backside of the recipient a mass spectrometer (Pfeiffer QME200) was mounted in an individual small recipient that is equipped with a small turbomolecular pumping unit (Pfeiffer TMU 071T) of its own. The mass spectrometer can also be separated from the main chamber with a rotary valve since it is recommended to leave the spectrometer's sensor-head always under vacuum to avoid deterioration. During evaporation, when the valve between main chamber and spectrometer is open, the turbo pump allows differenial pumping. Instead of a normal 35mm copper seal, a

35mm copper plate with a 1.5mm hole in the middle was introduced. The small hole guarantees low pressure on the spectrometer side while the vacuum in the main chamber during deposition is at least 2 orders of magnitude higher. In order to control thickness and deposition rate, a water-cooled resonant crystal is mounted on the left side of the main recipient at about the same height as the viewport; it is read out by a deposition monitor (Fa. INFICON XTM-2).

The lower part of the main chamber is equipped with 3 magnetron sputtering cathodes (Mighty MAK 2") as depicted in figure 4.3, bearing presently iridium, gold and aluminium as targets (Fa. MATECK). The water cooling for the cathodes is located at the bottom of the recipient and connected to them via plastic hoses: two adjacent metal rings (one as an inlet, the other as an outlet) account for constant water flow through the cathodes. Each cathode can be shut off from the water supply by a valve. The bottom recipient still has free ports (diameter: 16 to 35mm) for mounting of manipulators or other vacuum equipment.

- **The prechamber** is a cross-like recipient (see figure 4.2) of which the main volume is ∼25x25x25cm³. It was added to the system with the intention to allow transfer of substrates into the main chamber without breaking its vacuum. The magnetic transfer manipulator (Fa. Huntington) is equipped with a removable substrate holder. In order to offer the possibility to ion etch already evaporated films in the same system, an argon plasma source (Ion Tech. INC. MPS 3000PBN) was mounted on the lower part of the prechamber. Substrates are introduced via a load lock which acts also as a viewport during ion etching. A turbo pump (Fa. Varian V250) is located on top of the recipient. Due to geometrical reasons the pump was mounted with a 'knee' adapter thus putting the pump in a horizontal position. Its upright positioning would mean a direct exposure to the etch plasma (due to the geometrical setup of the chamber and would lead to a rapid destruction of the turbo pump. In addition, the turbo pump has to be water cooled since the pressure regime (3-5x10^{-4}mbar) during ion etching causes a drastic increase in temperature. The vacuum is monitored with a thermocouple gauge and an ion gauge (Fa. Varian) located at the backside of the recipient, as is the inlet for the argon gas. The prechamber is separated from the main chamber by a gate-valve. The typical time for pumping the prechamber after insertion of substrates is 0.5h, then the valve to the main chamber can be opened for the substrate transfer. After successful transfer the gate-valve is shut again.

- **The periphery** can be split into two main parts: vacuum related electronics and electronics necessary for evaporation. All units for controlling the vacuum pumps

are located at the bottom of the rack depicted in figure 4.4. The RF source (Fa. Technics HFG500), necessary to drive the sputtering cathodes, is mounted in the middle of the rack and is equipped with powerful ventilation at the back. The matching controller is located just above. It is responsible for the right tuning of the RF matchbox fixed on top of the RF generator. The upper section of the rack is equipped with various pressure gauge read-out monitors, an argon gas inlet regulator and the deposition monitor.

Figure 4.4: Picture of the new magnetron sputtering system for future production and treatment of cryogenic detectors.

4.5.4   First Results and Further Potential

When the above mentioned sputtering facility was set up, a series of tests were performed aiming at optimizing various parameters of the system. First concern was given to the vacuum conditions that could be created in the recipient. It turned out that the vacuum that could be achieved in the main chamber with only turbo pump 1 (TP1) (see figure 4.2) and with no prior bake out, was $\sim$5x10^{-8}mbar after 12 hours of continuous evacuation. After 48 hours the system reached a best final pressure of $\sim$6x10^{-9}mbar, which is very satisfactory. When the second turbo pump is added to evacuate the main chamber virtually no improvement in end pressure is observed, but this pump is indeed needed during sputtering when the pressure inside the system increases to 3.2x10^{-4}mbar,

a regime at which one single turbo pump would suffer deterioration if used in frequent or long mode. With the small turbo pump on top of the pre chamber a vacuum of $\sim 5.5 \times 10^{-7}$ is achieved within 0.5h and can be decreased to $\sim 1.5 \times 10^{-7}$mbar after a few hours of pumping. Transfers are possible by opening the gate valve between pre and main chamber. Further experience has proved that one should stick to a time window of at least 2 hours in order not to deteriorate the (excellent) vacuum conditions in the main chamber; best results e.g. when producing 20050413 (see table 4.1) were obtained under the best vacuum parameters achievable.

The next step in characterizing the system was the test and calibration of the resonant crystal for determination of deposited film thickness and sputtering rate during evaporation. The calibration of the read-out module was performed for iridium, gold and aluminium, the only targets mounted presently in the system. They are the four main materials required to produce TESs for cryogenic detectors at our institute. Table 4.1 gives an overview of a series of test depositions performed on different substrates, at various rates and distances. To guarantee precise film thickness determination and to check the calibrations of the deposition monitor, some sputter depositions were analyzed with an α-stepper.

The first deposited layers were gold on silicon substrates. Various sputtering rates were tested: the rate of at maximum $2.2\overset{\circ}{A}/s$ achievable in our old 'Kaufmann-source' based system could easily be pushed to $5.0\overset{\circ}{A}/s$ under stable conditions; if R.F. power was further increased the rate could still be pushed even up to $\sim 10\overset{\circ}{A}/s$, but became more and more uncontrolable followed mostly by an extinction of the argon plasma. As a demonstration that the potential of high sputtering rates allows the production of thick layers of a specific material to act e.g. as a reflective or shielding coating, a watch, severely affected by corrosion was cleaned and then successfully coated with $\sim 0.5\mu$m of gold. Another investigation concerning the sputtering of shielding roman-lead layers with thicknesses in the μm range, is mentioned at the end of this chapter (see section 4.5.5.

A first test of gold deposited onto silicon as required in the production of gold bond pads for a defined thermal contact of TES based cryogenic detectors was performed. In this case a $200\times400\mu$m^2 bond pad on a light detector for the CRESST experiment was structurized out of the sputtered gold film. The deposition of the gold bond pad as well as the measurement of the detector were successful.

After the satisfactory deposition of gold, iridium was tested next. The depositions were performed on silicon as well as on sapphire substrates; parameters concerning these depositions are listed in table 4.1. Most of the depositions were followed by a residual resistance measurement: Using ge-varnish, the substrate was glued onto a holder mounted in a helium dip stick. The electrical contacting of the iridium film with the wiring of the

Sample	Thickness [$\mathring{A}$]	Rate [$\mathring{A}s^{-1}$]	Distance [cm]	Substrate	RRR
20050218	400	0.1	12	Si	1.47
20050221	400	0.1	12	Si	1.54
20050223	404	0.8	12	Si	1.46
20050322	400	0.1	32	Si	1.44
20050411	400	0.1	12	Al_2O_3	2.84
20050413	1233	0.1	12	Al_2O_3	22.58

Table 4.1: Results obtained from RRR measurements with 6 different samples (4 silicon substrates and 2 sapphire substrates). The thickness of the evaporated layers, as well as sputtering rates and distances between substrate and target are given.

dip stick was effectuated by 4 aluminium bonding wires of $25\mu m$ diameter ultrasonically welded. The resistance of the film was then measured with a LR-400 resistance bridge once at room temperature and then again at liquid helium temperature (4.2K)(see [86]). The ratio of resistance at room temperature and resistance at helium temperature is defined as the residual resistance ratio (RRR):

$$RRR = \frac{\rho(300K)}{\rho(4.2K)} \tag{4.1}$$

The first experiments exhibited RRR values of 1-4.5, which are in agreement with most results obtained in this field, also by other groups [87]. Nevertheless, deposition 20050413 (see table 4.1), in which special care was given to extremely good vacuum conditions and careful mechanical treatment of the substrate, proved to have a RRR value of 22.58. This is an exceedingly good value and comparable to best results achieved by other groups in this field [87]. The importance of such a good RRR ratio in terms of superconductivity is a high mean free path length for Cooper-pairs determining eventually the quality of the superconducting layer and thus also the performance e.g. of a TES.

4.5.5 A Desktop Magnetron Sputtering System for Roman Lead Coatings

Since low radioactivity level is often of great importance for cryodetectors, tests have been performed with a small magnetron desktop sputtering device depicted in figure 4.5 (Fa. POLARON) using normal and roman lead as targets as shown in and figure 4.6 (for properties and advantages in radiopurity see section 5.4). The idea was to demonstrate e.g. the feasibility of a sputtered $\sim10\mu m$ thick roman lead coating inside a copper detector

Figure 4.5: Polaron magnetron sputtering device
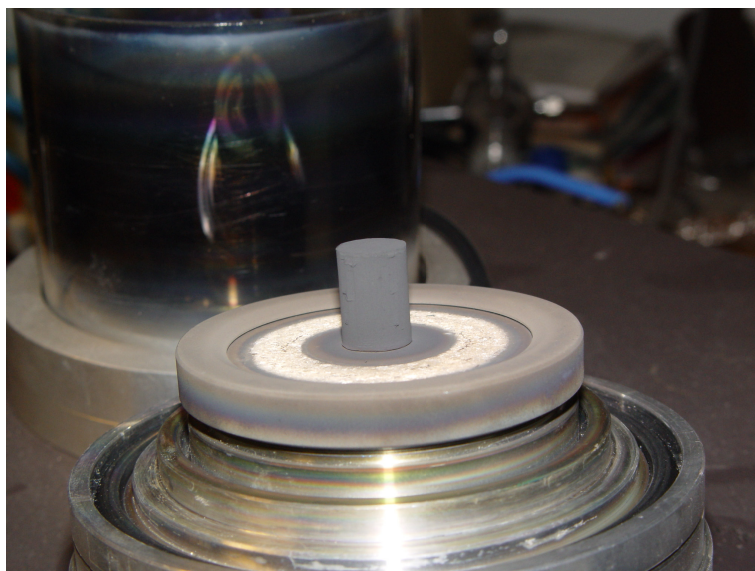
Figure 4.6: Roman lead target designed for the Polaron desktop magnetron sputtering device.

holder. Tests showed positive results after the lead target was adapted in geometry to the cylindrical holder.

Chapter 5

Design and Construction of Composite Cryogenic Detectors for GNO

5.1 General Aspects and Requirements

The aim of this section is to define the requirements that have to be met if a cryogenic detection concept is to be introduced in a radiochemical solar neutrino experiment like GNO. All the necessary experimental experience to keep a radiochemical detector going has been gained over numerous years, which is, for instance, reflected by high efficiencies concerning chemical extraction and further processing in the so called solar runs (see chapter2). In other words, no established procedure in the experiment must be altered which results in the fact that a suitable interface to the existing experiment has to be found. Germane gas (GeH_4) which is the final product of a solar run, containing the few neutrino-produced ^{71}Ge-atoms seems to be the ideal candidate. It is usually mixed with Xenon and then introduced into miniaturized proportional counters to be measured over a period of $\sim$6 months [54], [74]. The behaviour of germane gas on the other hand is such, that it can be dissociated at temperatures higher than 280°C following the equation:

$$GeH_4 \longrightarrow Ge + 2H_2 \tag{5.1}$$

This so called chemical vapour deposition (CVD) can be performed onto or into a substrate that will later act as the absorber of the cryogenic detector bearing the neutrino-produced ^{71}Ge on or in it. In the following sections it will become clear that the temperatures needed to perform a highly efficient chemical vapour deposition ought to be in

the temperature region between 400°C and 500°C, unfortunately affecting severely the superconducting properties of the transition edge sensor. To overcome this deterioration or destruction of the phase transition thermometer, a separation of the CVD and the fabrication of the TES becomes unavoidable. In addition, a post-CVD evaporation, structurization and testing of the TES would take too long in comparison to the half-life of ^{71}Ge ($T_{1/2}$= 11.43d).

Concerning the detection performance itself the main emphasis has to be put on the long-time stability of the cryogenic detector and the cryostat it is operated in. Along with the longterm measuring conditions, the detection must be highly efficient, i.e. ∼100% and therefore requires a 4π solid angle geometry. The detector(s) should have a reasonably good energy resolution, i.e. ∼200eV at 6 keV (FWHM), sufficient to account for an excellent resolution of the decay channels of ^{71}Ge via X-rays and Auger-electrons (see section 7.3): M-capture: 0.16keV, L-capture: 1.30keV, K-capture: 10.37keV. To allow detection of the M-capture, never achieved with miniaturized proportional counters in GNO, the energy threshold of the detector should not exceed ∼100eV, a parameter severely depending on the individual TES properties. Therefore reproducible production of the TESs is also an exceedingly important prerequisite. Further aspects for a new detection concept are the radiopurity of the various detector components and surroundings, redundancy concerning the overall handling, mounting and functioning of the cryo-detector as well as the cryostat in which it is operated.

5.2   Development of a Composite Detector

Driven by the development of low-temperature detectors for the solar neutrino experiment GNO, a way had to be found to avoid deterioration of the iridium-gold bilayer. This was realized by separating the deposition of germanium and the fabrication of the TES. The decoupling of these two processes was achieved by producing a 1x3mm^2 TES on an individual silicon substrate (5x7x0.25mm^3) that was later glued to a regular sapphire substrate (10x20x1mm^3) using a special cryo-resin (EPO-TEK 301-2) as described in section 5.2.1. Such a detector where the TES on an individual substrate is glued to the absorber we call composite detector.

Also other composite detectors were produced for this work: in section 7.4 a TES on a silicon substrate was attached to a 5x7x4mm^3 Roman lead absorber to investigate an alternative 4π design for GNO and the potential for radiopurity analysis in the mBq range; in section 8 another application is discussed where feasibility studies with iridium-gold TES for the MANU2 experiment [83] for neutrino mass determination were performed with great success. The separate treatment of detector components during fabrication

EPO-TEK 301-2 (optically transparent epoxy)	
index of refraction	1.564
color	transparent
specific gravity	0.95g/cm^3
curing temperature	80°C for 3h
application for mK use	yes
cyclability 300K to mK	yes
intrinsic radioactive impurities	clean, according to γ-spectroscopy

Table 5.1: Properties of EPO-TEK 301-2.

followed by a rapid coupling process of the individual parts is a most powerful tool for many applications of cryogenic detectors (see section 8).

5.2.1   Assembly of Composite Detectors

Obviously, the choice of the right 'glue', its subsequent treatment and its introduction into what is to become the cryogenic detector, is of great relevance. It has to exhibit certain qualities to allow thermal cycling of the device from room temperature to very low temperatures down to the mK range. Also aspects concerning intrinsic radiopurity were investigated (see section 5.4 for further detail). The 'glue' used in this work is a two component epoxy cryo resin 301-2 (Fa. EPO-TEK) which proved to be the right choice for our applications. Table 5.1 lists the various physical parameters and properties of the resin.

Experimental experience gained during the production of composite detectors lead to a recipe that proved both, satisfactory and reproducible results:

- Mixing of the two resin components at a ratio of 100:35 at room temperature using a small glass container.

- 'Baking out' of the resin at a temperature of 80°C for ∼2 hours; the baking procedure has to be stopped when the viscosity of the resin is increasing. From this point on the glue should be applied as soon as possible since it will now dry out quickly. Nevertheless there is a great advantage connected to the higher viscosity of the glue - it is much more stable when being applied and glue spots can be decreased to a size of ∼10μm.

- The epoxy resin itself is applied using a thin needle or for extremely small spots one can use a bonding wire of 17-25μm diameter. It is possible to create microscopic drops on the end of the wire by dipping it into the resin. They can then be deposited under a microscope where they can be measured in diameter giving a hint of how broad the glue surface will be when under pressure between the two substrates.

During the tuning of the above mentioned glueing procedure, where parameters as bake out temperature, time of the bake-out, different mixing ratios of the two epoxy components, photo exposition, glueing and then heating, etc. were tested it became clear that the liquid resin changes its viscosity while drying causing sometimes nonuniformities of the spot. Figure 5.1 shows four examples of glue spots after various treatments, only one, d), is satisfactory and reproducible with respect to energy resolution and decay time of the pulses (see figures 5.6 and 5.7). It was obtained according to the recipe just described.
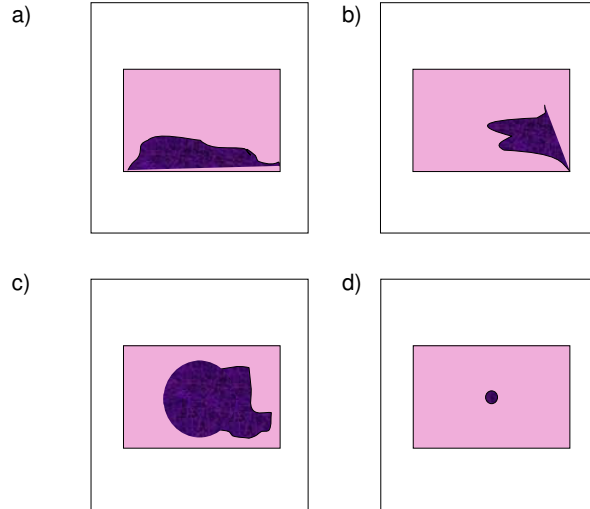
Figure 5.1: Illustrations of 4 silicon substrates differently glued to the sapphire substrate, d) being the best spot.

5.2.2 First Results

Figure 5.2 shows the setup of the first composite detector si405c. In fact four 1x3mm^2 TESs were produced out of the original si405c 10x20x0.25mm^3 silicon substrate: After the photolithographic processes and structurization via ion etching, four individual TESs ($\sim$5x7x0.25mm^3) were cut out of the initial substrate in our crystal laboratory in Garching. The transition temperature of TES si405c was $\sim$28mK with a phase transition width of $\sim$2mK. The sapphire substrate is thermally decoupled from the copper holder by three sapphire spheres (diameter: 1.0mm). The silicon substrate bearing the Ir/Au TES was glued asymmetrically taking into account the germanium layer that would normally be deposited onto the remaining surface of the sapphire substrate. The gluespot could be seen through the transparent sapphire absorber and was $\sim$100μm in diameter. The copper holder in which the detector was mounted was open at the bottom thus allowing irradiation of the detector from below. The ^{55}Fe-source was thermally decoupled from the detector holder by a 30mm long cylindrical plastic rod (Fa. SINTIMID). The idea behind this configuration of measurement was to give rise to pulses only in the sapphire substrate, in order to 'simulate' a source as e.g. ^{71}Ge that would later be deposited onto this absorber. The whole setup was mounted below the mixing chamber of a ^{3}He/^{4}He dilution refrigerator (see section 7.1) and operated at the transition temperature of the TES ($\sim$28mK).
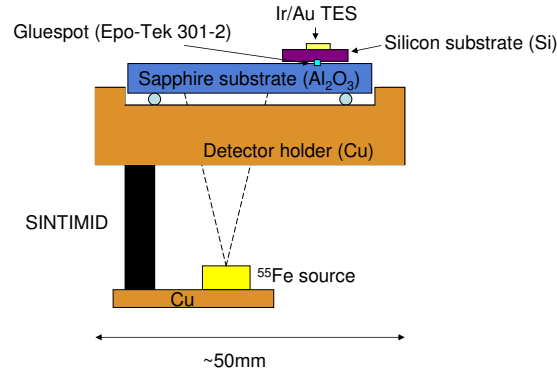

Figure 5.2: Schematic positioning and setup of the first composite detector.

Figure 5.4 shows a picture of the first realized composite detector. The sapphire absorber, as well as the silicon substrate bearing the 1x3mm^2 Ir/Au TES can be seen. An amazingly good result was achieved concerning energy threshold, which was about 100eV. Such a low energy threshold, as pointed out in section 5.1 is especially attractive in the case of ^{71}Ge-measurements where the M-capture with an energy release of 160eV would be detectable. The energy resolution of 187eV (FWHM) at 5.89keV, as depicted in figure 5.3, was obtained when the detector was irradiated from below with an ^{55}Fe-source and thus only illuminating the sapphire absorber.
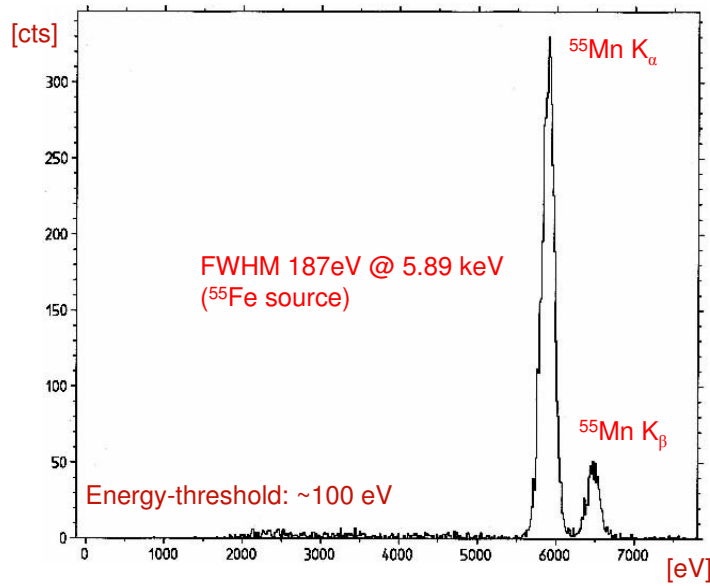
Figure 5.3: ^{55}Fe spectrum recorded with the first composite detector.

In a later cool down, the detector was irradiated from outside the cryostat with a ^{57}Co source. The main γ-lines (at higher energies) emitted by this source are at 122.1keV and 136.5keV. The intention was to study the behaviour of the detector at higher energies and rates and to have the possibility to illuminate both the sapphire and the silicon substrates at the same time. Figure 5.5 shows the energy spectrum obtained with the ^{57}Co source placed outside the cryostat (see section 7.1 for setup details). Due to the low
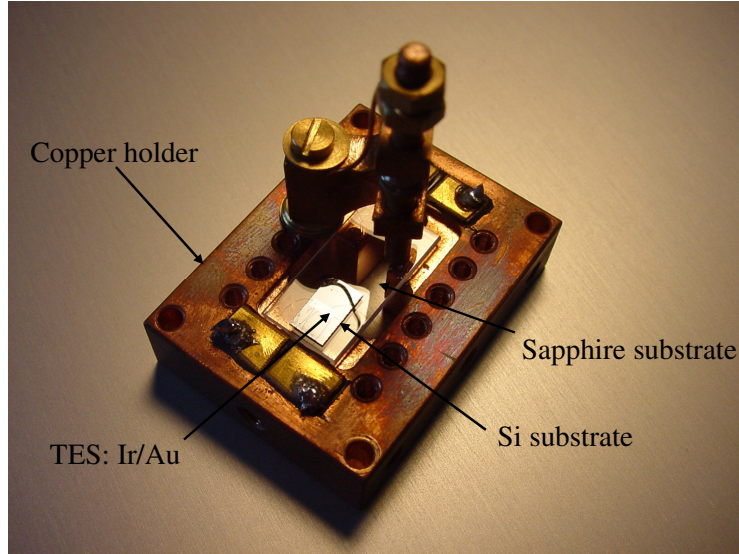
Copper holder

Sapphire substrate

Si substrate

TES: Ir/Au

Figure 5.4: Picture of the first realized composite detector si405c.

absorption efficiency of sapphire and silicon for the 122.1keV and the 136.5keV γ-lines, mainly the Compton edge at 39.4keV is visible. Apart from irradiating both substrates this measurement was also performed to investigate the possibility of external detector calibration (section 7.2).
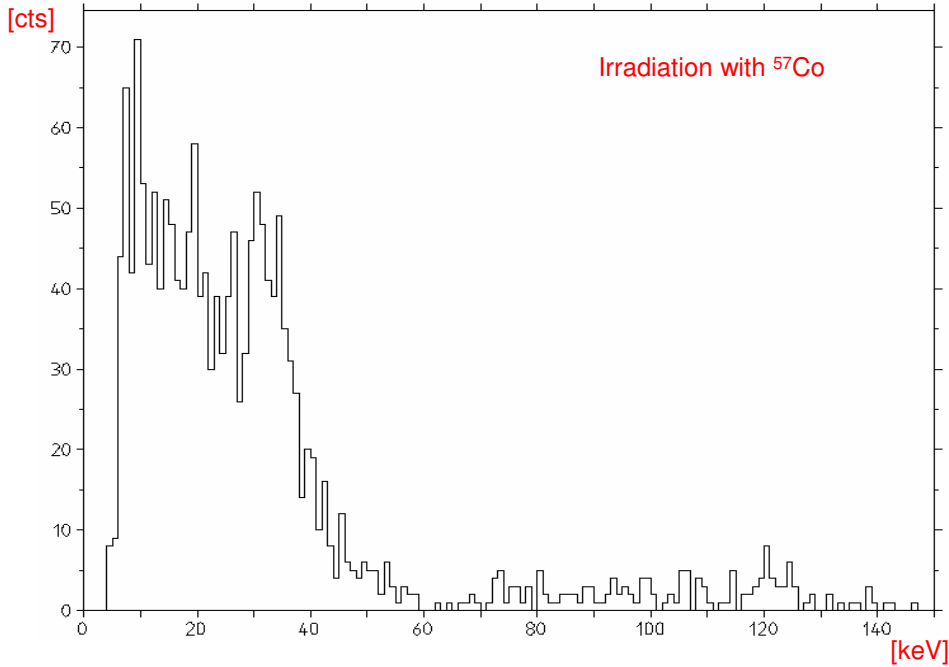

Figure 5.5: ^{57}Co spectrum recorded with the first composite detector. The spectrum clearly shows the Compton edge of the 122keV γ-line at $\sim$39.4keV and possibly a small indication of the photo peak at 122keV.

After analyzing the pulses produced by this detector irradiated with ^{57}Co, it became clear that there are two different categories of pulse shapes: fast and slowly decaying pulses that can be attributed to events ocurring in the sapphire and the silicon absorber, respectively. This is demonstrated in figures 5.6 and 5.7 which show pulses with decay times of $\sim$2ms (from the silicon substrate) and $\sim$8ms (from the sapphire substrate), respectively.

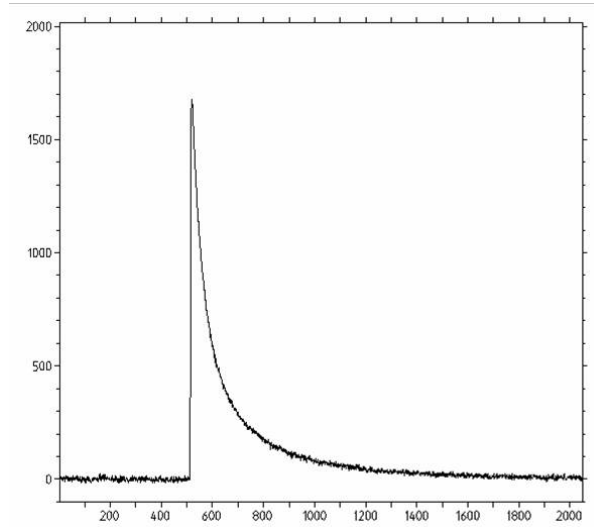This classification of the pulses was also confirmed by a Monte Carlo simulation which

Figure 5.6: Pulse originating from the silicon substrate, the decay time is ∼2ms.
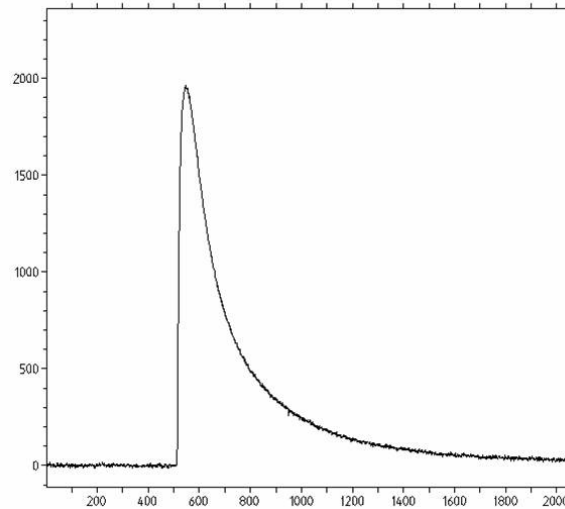
Figure 5.7: Pulse originating from the sapphire substrate, the decay time is ∼8ms.

predicted the eventually measured event rates in the silicon and sapphire substrates. Further, the ratio of slow and fast pulses, experimentally determined, corresponds to the ratio of the volumes of the sapphire and the thermometer substrates. In addition, it was found that the pulses attributed to the sapphire exhibited not only two decay components (see chapter 3), but needed a third one to fit the further progression of the signal. This longer decay time with respect to events from the silicon substrate, as depicted in figure 5.7, is attributed to the glueing point, which in this case was of the order of $\sim 100\mu$m in diameter and acts as a 'bottle-neck' for phonons produced in the sapphire. A more detailed description of this transmission phenomenon is given in section 3.4.1. The conclusion of this pulse shape analysis is that energy absorption in different components leads to different pulse shapes and therefore to a determination of where the detected event took place. In other words, one might think of a geometrical arrangement of cryogenic detectors or absorbers, where the localisation of events could be utilized as a means of background suppression. Also a setup allowing directional determination might be conceivable.

The results gained with si405c were very satisfactory, especially since it was also the proof of feasibility of this new type of detector. Cryogenic detectors exhibiting the features of si405c would be desirable for a solar run in in gallium experiments: The three main decay channels of ^{71}Ge would have been well separated. Furthermore a strive for much higher energy resolutions with Ir/Au TESs is highly promising as described in chapter 8.

5.3 4π-Efficient Detection Design for GNO

It has been mentioned earlier that the introduction of cryogenic detectors in GNO was discussed under the assumption that a highly efficient ($\sim 100\%$) detection of ^{71}Ge can be achieved, thus increasing the overall sensitivity of the GNO experiment. This order of efficiency can only be reached, if the detection is performed in a 4π full solid angle geometry. In the PhD thesis of S. Wänninger [84] such a geometry was realized to prove the principle and the efficiency of this detection technique. Later the results were cross-checked by means of Monte Carlo simulations [84].

Figure 5.8 is an illustration of the detector set up designed for 4π detection. Basically, the information of two individual detectors is used to obtain a ~ 100 efficiency. To avoid energy losses, it is always the summed energy of detectors A and B that is considered ($E_{tot}=E_A+E_B$). A Monte Carlo simulation for this detector geometry gives a lower limit of $\sim 98\%$ for the detection efficiency. A loss of $\sim 1.9\%$ is mainly due to the energy threshold (~ 230eV, [84]) of the detector, which in [84] did not permit the measurement of the M-capture at 160eV. The mutual distance of the detectors, which in this case was ~ 1mm
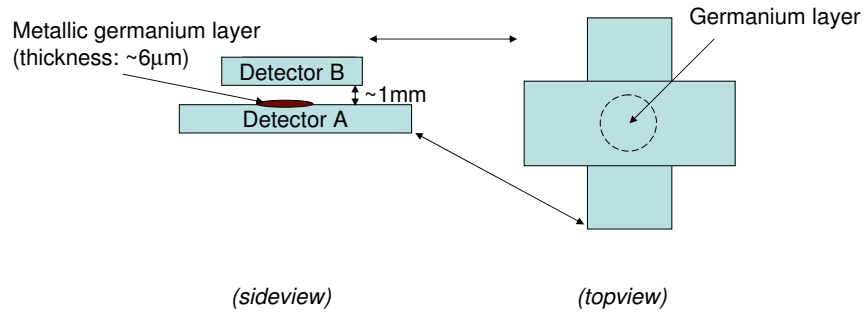
Figure 5.8: Geometrical setup of two detectors to realize a 4π efficient detection [84].

[84], is responsible for a loss of ∼0.1%. X-rays and/or Auger electrons from the surface of the germanium layer can escape the detector via this slit. Bringing the detectors closer together, which was done in the set up described in section 5.3.1 and a low energy threshold, can then increase the detection efficiency close to 100%. For these reasons the depicted geometry was maintained in the present thesis. Nevertheless, also a different type of 4π detection set up, using a single detector consisting of a Roman lead absorber of 5x7x4mm^3 and a TES on a silicon substrate, was tested and is described in section 7.4.

5.3.1 Design of a Low-Background Holder and Shielding for the 4π Detector

With the aim to replace the 4π detector holder used for the first feasibility studies of ^{71}Ge measurements [84] and at the same time to create a shielding for the detector against natural radioactivity, a new detector holder was designed. Also various aspects regarding handling and reliability, if introduced in GNO, were taken into account before construction.

First, suitable materials have to be investigated. In the case of cryogenic detectors the use of copper, due to its attractive thermal properties, is common. Second, the material surrounding the detector should be suited for low level counting. Luckily, we had access to ultrapure copper mainly used for the CRESST experiment and stored in our underground laboratory (15m.w.e.) in Garching. Prior to its further treatment the copper was analyzed by a low level germanium detector to investigate intrinsic radioactive impurities. These measurements, which are reported in section 5.4, proved that the quality of the copper, in terms of radio purity, was excellent.

Since the detectors are operated at temperatures in the mK range the copper must be annealed to guarantee homogeneous cooling of the holder. For this pupose a new insert for the annealing oven of our crystal laboratory was constructed. The insert is a cylindrical quartz recipient (diameter: 127mm, length: 1300mm) to which a double flange can be attached. The recipient can then either be flushed continuously with gas, e.g. argon, or be evacuated to ∼5x10^{-6}mbar after one hour of pumping with a turbo molecular pump. The dimension of the recipient were chosen such that it can host also bigger pieces of copper than commonly used annealing facilities. The annealing oven in which the insert is placed can generate 3 different temperature zones of ∼30cm length along the recipient. The following procedure was applied for annealing various copper parts used during construction of the detector holder and the internal shielding of the cryostat (see below and section 5.3.2):

- All copper parts were cleaned with ultrapure aceton (Fa. MERCK) to remove dirt or thin oxydation layers. The copper parts were placed in the recipient which was also previously cleaned.

- The heat up time from room temperature to 700°C, was 7h; all three temperature zones in the oven were at the same temperature during the whole procedure.

- 7h at 700°C

- Cooldown, again 7h from 700°C to room temperature. The vacuum during the whole annealing procedure was 5x10^{-6}mbar.

Also longer annealing times and higher temperatures have been considered for copper. However, we found that the recipe mentioned above guarantees a homogeneous cooldown of the holder without weakening the copper too much in terms of mechanical strength. Some of the copper parts forming the detector holder had later to be retreated mechanically and should therefore be not too 'soft'.

It was mentioned earlier that the efficiency of the 4π detection geometry slightly depends on the distance between the two detectors. Therefore, special care was given to reduce the slit to ~1mm. First, an aluminium dummy was constructed which allowed to check all the required features like handling, mounting in the ultrasonic welding machine for electrical and thermal contacting of the eventual detector.

Figures 5.9 and 5.10 are schematic drawings of the holder; figure 5.11 shows a picture of the final detector holder with detectors mounted inside. This 4π detector system was later used for many cooldowns and measurements. It is designed in such a way that each of the two individual detectors can be placed in a separate holder. After thermal and electrical contactation is finished, the two halves of the holder are placed on top of each other with the two detectors forming an angle of 90° with respect to each other, see figure 5.8. After locked by screws, the two halves are forming a completely closed volume around the detectors. A way had to be found to account for efficient evacuation of the holder once the detector is mounted in the IVC (=inner vacuum chamber) of the cryostat, where the pressure prior to nitrogen cooldown is ~5x10^{-5}mbar. The schematic drawing of the detector holder depicted in figure 5.10 shows how this problem was overcome by L-shaped holes which prevent radiation to interact with the detector directly.

The electrical contacting was designed such that the detectors can be bonded directly inside the holder. As can be seen schematically in figure 5.10, two copper pads (5mmx5mm) were glued with epo-tek onto the copper to decouple it electrically from the
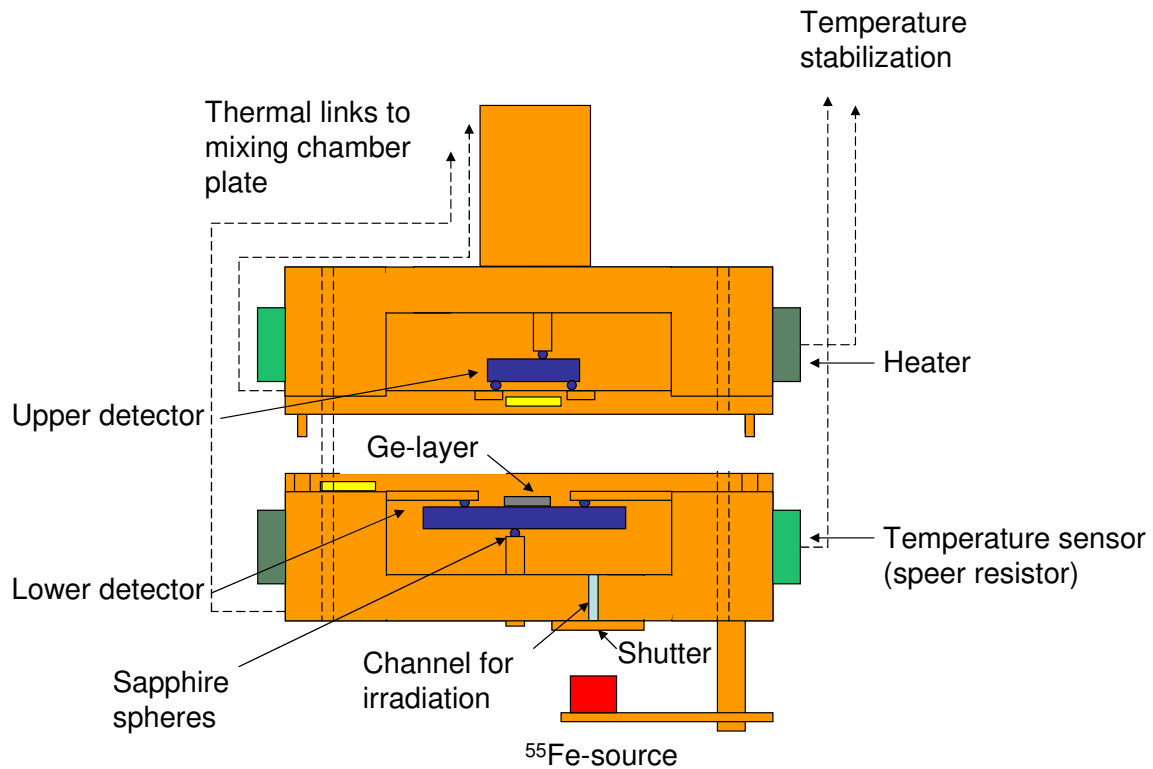
Figure 5.9: Schematic drawing (sideview) of the 4π holder showing the electrical and thermal contacts. Both detectors can be irradiated e.g. by a [55]Fe source outside the holder.

Insulated Cu-pads
for electrical contactation

External electrical contactation
points for SQUID read-out

Aluminium bonding
wires

Gold bond wire for
thermal contactation

Ge-layer

~60mm

Hole for ^{55}Fe
calibration

Sapphire
absorber

Silicon substrate
with Ir/Au TES

L-shaped holes for
evacuation

(lower detector)
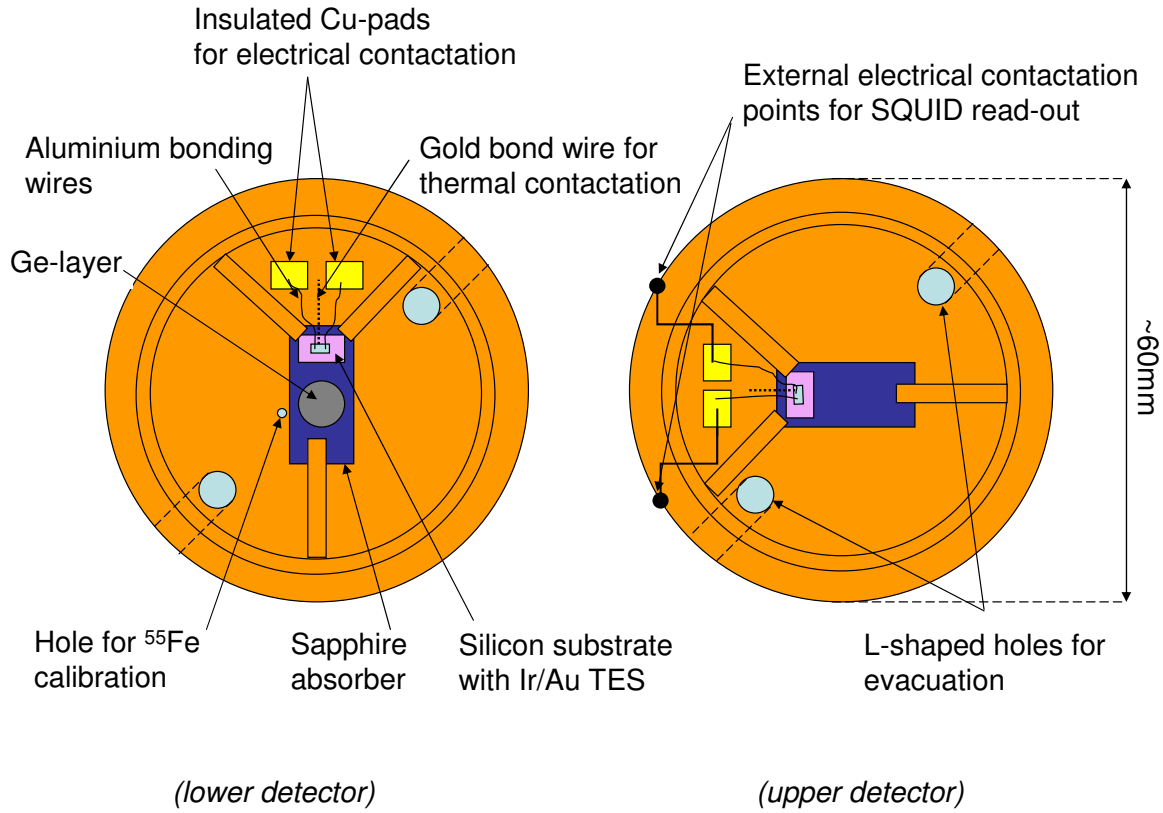
(upper detector)

Figure 5.10: Schematic drawing (topview) of the 4π holder showing the electrical and thermal contacts. The detectors can be bonded directly inside the holder. Two copper pads are glued to the copper holder for electrical insulation.
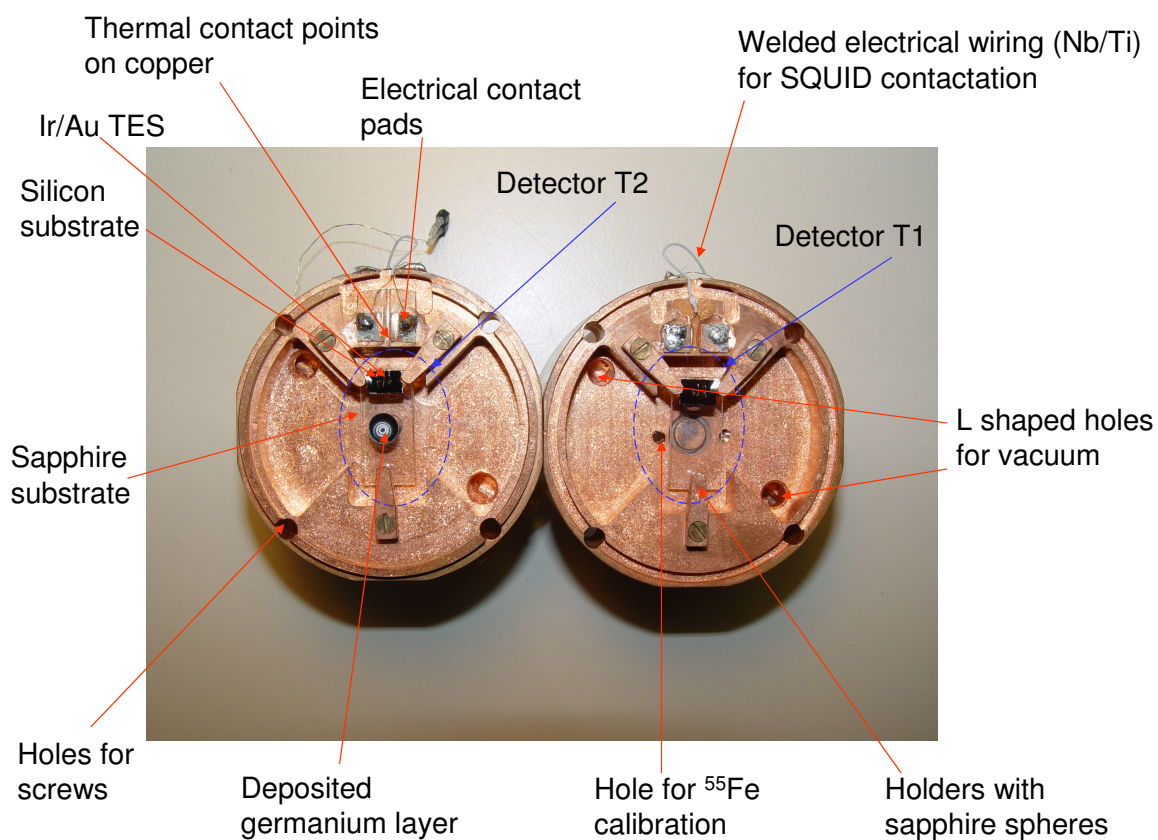
Figure 5.11: Picture of the 4π holder opened with two detectors mounted inside. On one sapphire substrate (left) the deposited Ge film containing the ^{71}Ge activity can be recognized.

holder itself. Epo-tek was utilized again, since it is located in the close surroundings of the detector and its features concerning radio purity had been analyzed before-hand as discussed in section 5.4. From these two pads two electrical wires are brought outside where they are again welded onto two glued copper pads finally serving as contacts for the SQUID read-out (see section 3.7.2). Special care was given to the feed through of the wiring, which was designed such that no direct irradiation of the detector from the outside is possible, the wires are always led around two corners. In figure 5.11 the deposited germanium can be seen on the sapphire absorber of detector T2. In the upper part of T1 and T2 the silicon substrates with the Ir/Au sensors can be seen. The bottom of the 4π holder (detector T1) exhibits a small hole (∼1mm in diameter) for ^{55}Fe calibration.

Before mounting the detectors in the 4π holder, it has to be cleaned. For this the two holder parts as well as all screws and parts used inside the holder have to be etched to remove impurities from the copper surface. This was done according to the following procedure:

- First, all parts are immerged in a recipient filled with ultrapure aceton (Fa. MERCK). The recipient is then placed in an ultrasonic bath for 15min.

- After removing the parts from the aceton bath, they are flushed with nitrogen gas.

- Finally, the copper parts are placed in another recipient filled with a 10% HNO$_3$ solution, which is kept at a temperature of 80°C on a heater plate. It has to be juged by eye when the etching should be stopped. After 10 to 15min the copper surfaces become very clean and shiny, whereas the solution turns slowly blue. At this point the etching can be aborted. If the etching procedure is applied for too long a time, the copper will start to disintegrate, especially the fine mechanical parts like small screws etc. can no longer be used. Also the repeated cleaning of the same detector holder should be performed with care.

5.3.2 Mounting of the Detector in the Cryostat

Once the 4π detector is fixed and contacted in its holder, it is put into an exsiccator and is taken from the cleanroom to the underground laboratory to be mounted into the cryostat. The setup of the cryostat including the data acquisition is described in detail in section 7.1. Figure 5.12 shows a picture of the bottom end of the cryostat insert. The mixing chamber plate of a ^{3}He/^{4}He dilution refrigerator is the stage where the base temperature (i.e. minimal temperature) is reached. In our case the base temperature is

~10mK; the lowest temperature ever reached with the full setup of internal shielding and 4π detector was 9.1mK. Underneath the mixing chamber an internal shielding consisting of low activity lead (<5Bq/kg, Fa. PLOMBUM, Poland; see section 5.4 for further details) and ultrapure copper, was attached. As mentioned before, this internal shielding was designed to protect the detector from radiation originating from the various inner parts of the cryostat. The weight that can be attached at the mixing chamber is limited to ~3kg. Therefore the internal shielding could not be made thicker and thus more effective in terms of shielding. Prior to this internal shielding design, the lead was not yet segmented and used as one single piece with one copper plate (diameter: 80mm, thickness: 5mm) on top and one at the bottom (diameter: 80mm, thickness: 10mm) of the lead block. During a test cooldown the lead shielding which was then attached thermally to the mixing chamber plate did not cool down. In fact, the whole insert could not be cooled lower than ~300mK. The explanation found was that both copper plates then attached to the lead cooled probably faster than the lead itself, which became superconducting at ~7.2K and therefore decreased drastically in thermal conductivity leaving the middle part of the lead block as a heat leak. After this unsuccessful cooldown, the lead was segmented into 2 cylindrical pieces (diameter: 80mm, length: 23mm) separated again by a copper plate (diameter: 80mm, thickness: 5mm) in the middle. Furthermore we decoupled the internal shielding from the mixing chamber plate with a 40mm long SINTIMID rod and attached the lead as well as the copper plates of the shielding thermally via 8 copper wires to the cold plate of the dilution refrigerator which has a temperature of ~100mK. From then on the cryostat did reach again its usual base temperature of ~10mK.

Most important, the 4π-detector holder has to be at base temperature. To achieve this, the detector holder was again decoupled thermally from the internal shielding by a 40mm SINTIMID rod. Both parts of the 4π-detector were then thermally connected to the mixing chamber plate via 4 copper wires (see figure 5.12). Measurements with this setup proved to be very successful and are described in detail in chapter 7.

5.3.3 Detector Calibration

To calibrate the detectors and in order to find suitable working points it is common to use an ^{55}Fe source for irradiation. Since the 4π holder was designed in a way that the detectors are shielded from outside radiation, a way had to be investigated to allow illumination by the ^{55}Fe source without causing to much background in the detector. This was realized by a 1mm hole in the bottom of the holder (see figures 5.9- 5.11) that can be closed if not required or opened for common irradiation of both detectors with a preferably weak radioactive source. Figure 5.13 shows two ^{55}Fe spectra obtained during simultaneous ir-

~300 mm

mixing chamber @ ~10mK

shunt boxes (SQUID read out)

thermal decoupling (SINTIMID)

thermal links to 100mK plate

Pb/Cu shield @ ~100mK
(clean Cu; Pb$_{pol}$, A < 4.2 Bq/kg)

thermal decoupling (SINTIMID)

thermal links to mixing ch.

4π detector holder and shielding
(clean Cu)

temperature stabilisation (heater/speer)

holder for ^{55}Fe calibration source
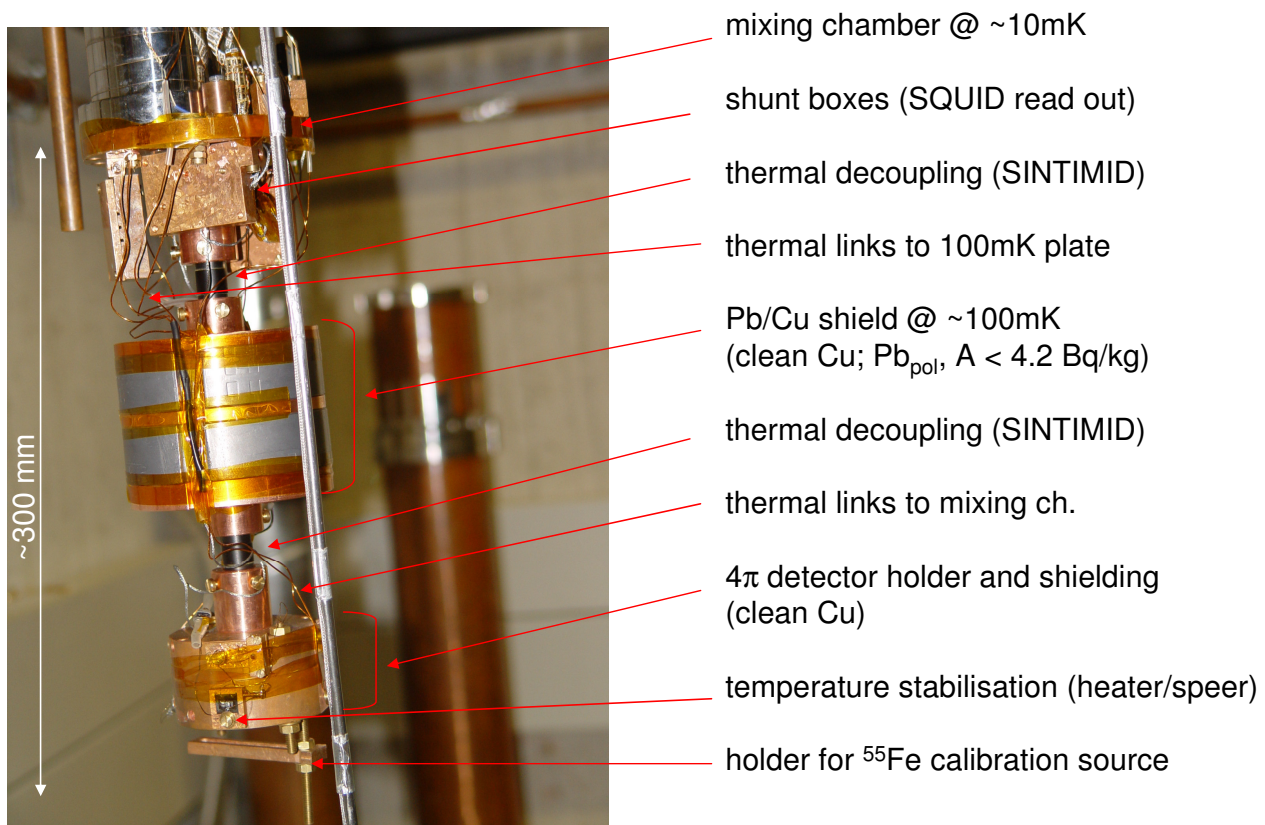
Figure 5.12: Setup of the internal shielding and the 4π-detector.

radiation of both detectors. In this case, we made feasibility tests with tungsten TESs as they are used in the CRESST experiment, instead of our iridium-gold TESs. Since the two TESs differed in their critical temperatures by ∼15mK, it was challenging to find a common working point for these two detectors. Once a temperature was found for the TES exhibiting the lower transition temperature, the other TES had to be stabilized using a much higher bias current to heat it up separately from the other detector. For this test the whole detector holder, i.e. both halves were equipped with only one heater and one temperature sensor (speer resistor) for temperature stabilization (see section 7.1 for more details). Figure 5.9 illustrates also the schematic set up and especially the positioning of the ^{55}Fe source with respect to the two detectors. Using two individual but identical data acquisition systems (Fa. National Instruments, PXI Bus) we were able to determine online the best common working point for the two detectors by analyzing the 'real time' energy resolution at ∼6keV. For the two detectors an energy resolution of 235eV (FWHM) and 220eV (FWHM) has been achieved, although the bias currents were very different: 32μA and 170μA (see figure 5.13). In the left spectrum of figure 5.13 the 'shoulder' on the left side of the 5.9keV peak originates from pile up due to the close geometrical position of the lower detector with respect to the source. Ideally, the holder (or the source) should have a shutter mechanism to open or close the source periodically during operation of the detector(s). The Milano cryogenic group for instance developed such a device for their neutrino mass experiment [88], [14].
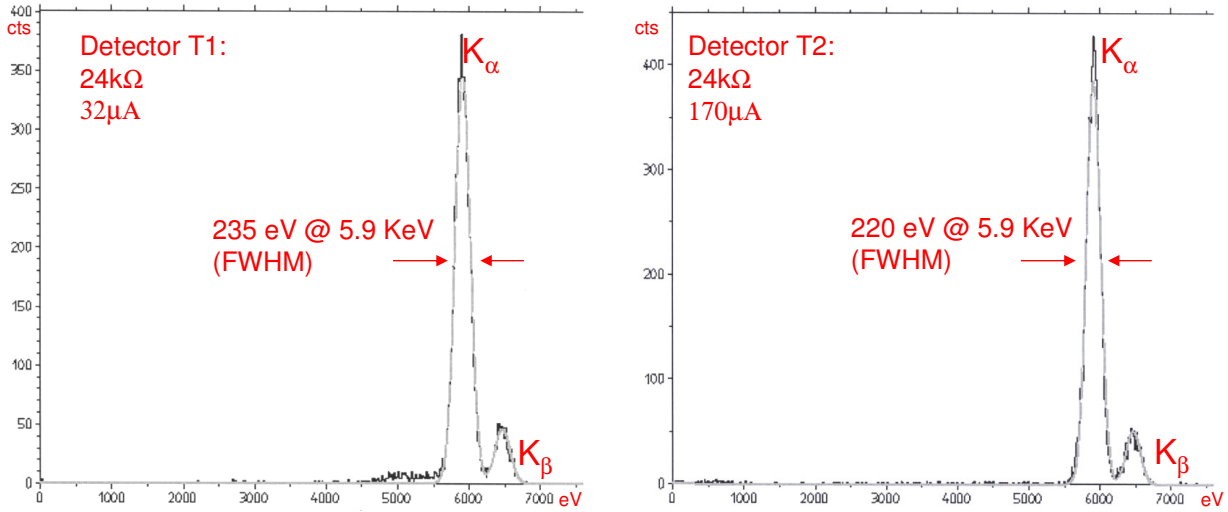
Figure 5.13: ^{55}Fe calibration spectra recorded during the simultaneous irradiation of the two detectors via a small hole in detector holder T1 (see figures 5.9 and 5.10).

5.4   Material Analysis

Before the new 4π detector holder and the internal shielding of the cryostat were fabricated, as presented in section 5.3 of this chapter, copper and lead used for these parts were analyzed by means of low-background γ-spectroscopy in the UGL (15m.w.e.) Garching. Especially the effiency of cleaning with HNO_3 acid of the copper surfaces of the 4π detector holder was investigated.

5.4.1   Experimental Setup for γ-Spectroscopy
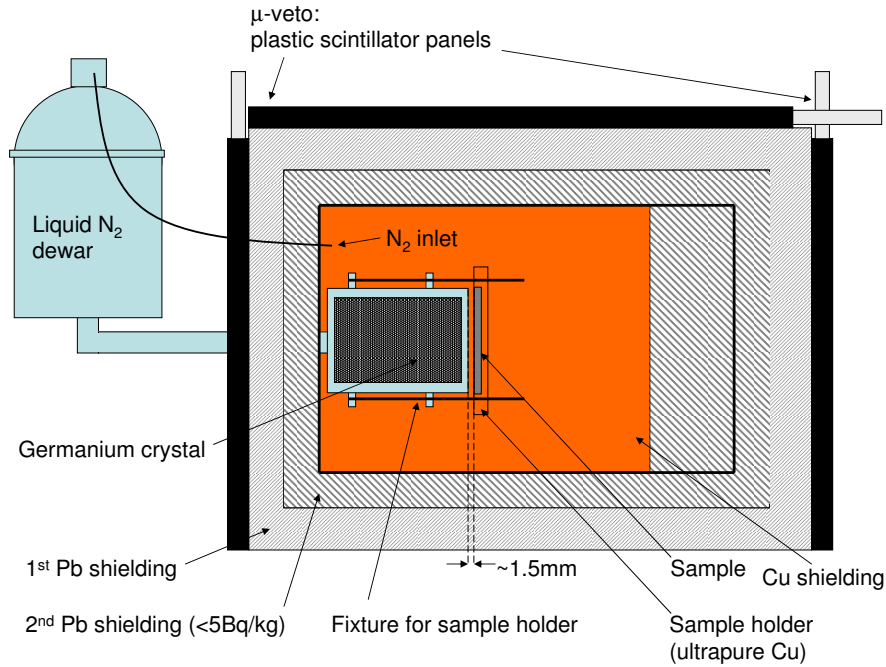
Figure 5.14: Schematic experimental setup of a germanium detector in the underground laboratory Garching used for material analysis.

The germanium detector (Fa. Ortec LOAX) used for γ-spectroscopy consists of a high-purity germanium crystal, which is cooled by liquid nitrogen contained in a dewar outside the detector housing. It is shielded, as depicted in figure 5.14, against natural radioactivity and muon induced radiation. The innermost shielding is realized by 5mm

copper plates, which are followed by 50mm thick lead bricks (Fa. PLOMBUM) with a low intrinsic ^{210}Pb activity. This low-activity lead shielding is further surrounded by a 100mm thick lead shielding using 'normal' (in terms of intrinsic activity) lead bricks. To allow rejection of muon induced background contributions the whole detector setup is surrounded by 6 plastic scintillator panels which are operated in anticoincidence to the germanium detector. In order to remove radon, the whole detector shielding is constantly flushed with nitrogen gas evaporating from the liquid nitrogen dewar.

The samples investigated were measured as depicted in figure 5.14. For all the measurements performed, a copper disk (120mm in diameter, thickness 5mm, made from ultrapure copper stored in our UGL) was mounted on a rail-fixture (see figure 5.14), so that the sample can be moved as close to the germanium detector as possible. The distance of the sample to the carbon entrance window of the detector was ∼1.5mm, whereas the copper disk covered the whole area of the window.

5.4.2   Results for Copper and Lead Components Used for the Internal Shielding of the Cryostat

First measurments performed with the setup described in section 5.4.1 were dedicated to the analysis of the ^{210}Pb activity in low-activity lead (Fa. PLOMBUM) and ancient Roman lead, since materials exhibiting both, a high Z value and a low intrinsic activity are ideally suited to shield low-background detectors. Figure 5.15 illustrates the decay of the unstable lead isotope ^{210}Pb. With a probability of 81% the decay occurs via β-decay that is followed by a γ-emission of 46.5keV, which can be monitored in the germanium detector.

The low-activity lead as used, e.g., in the shielding of the germanium detector was measured to check the nominal activity of ≤5Bq/kg given by Fa. PLOMBUM. The sample was 2mm thick and ∼100mm in diameter and placed in the copper disk see figure 5.14. The absolute activity of ^{210}Pb was measured to be 4.22Bq/kg, thus confirming the nominal activity of ≤5Bq/kg given by PLOMBUM. Also two samples of Roman lead depicted in figure 5.16 and figure 5.17 originating from different sources (one sample was found underwater, the second ∼1.5m underground) were analyzed using the same setup as described above. In both cases, after subtraction of a two weeks background data, only an upper limit of ∼3mBq/kg for the ^{210}Pb activity can be given. This is due to the fact that the part of the germanium detector connected to the liquid nitrogen dewar cannot be completely shielded with copper against the 46.5keV ^{210}Pb background originating from the PLOMBUM lead shielding. From these measurements the motivation arose to investigate the absolute activity determination by means of composite cryogenic detectors
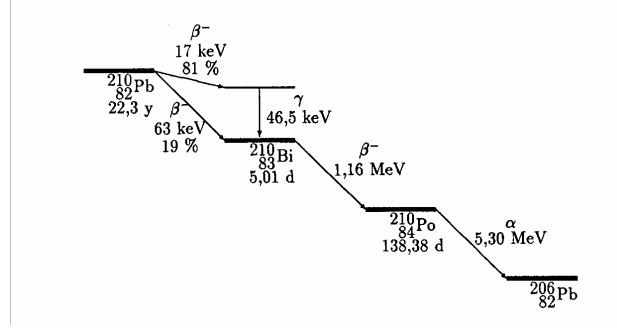
Figure 5.15: Decay of the lead isotope ^{210}Pb.

using Roman lead as absorber. Measurements using a macroscopic piece of polycrystaline lead (5x7x4mm^3) as absorber with a TES on a silicon substrate attached to it, are presented in section 7.4. Unfortunately, the energy threshold of this composite detector was too high to record the 46.5keV γ-line. However, using a smaller lead absorber with a microcalorimeter TES in analogy to the measurements described in chapter 8, where the energy threshold was low and the energy resolution excellent, the absolute avtivity might be determined cryogenically.

For the construction of the new 4π detector holder, ultrapure copper stored in the UGL was analyzed next. The spectra depicted in figure 5.18 and figure 5.19 were both recorded over a period of two weeks. The spectra show the same piece of copper once without surface treatment (figure 5.18) and once after 10min of etching in a 10% HNO$_3$ acid solution, heated up at 60°C (figure 5.19). Both spectra are depicted without background subtraction, however, the impact of the cleaning procedure applied can be recognized when comparing the two spectra. The spectrum shown in figure 5.18 exhibits several known background lines (see [95]), the energies of which are labeled in the figure itself. Two main backgound contributions can be distinguished: i) Contributions originating from the implantation of radon and its unstable daughter nuclei in the copper surface. ii) A contribution at 1460.86keV due to the primordial ^{40}K$\rightarrow^{40}$Ar decay which can be induced by perspiration of the human body, which contains - for biochemical reasons - a relatively large amount of potassium. The only remaining visible contributions in figure 5.19 after etching the surface of the copper for 10min with HNO$_3$ at 60°C, are the muon induced

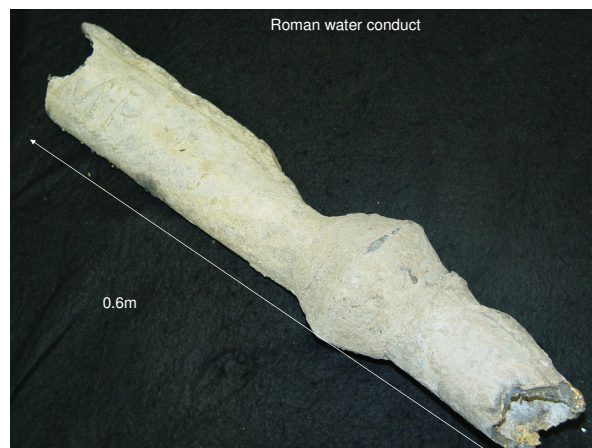Figure 5.16: Roman lead sample from a broken 'dolium', found underwater in Corsica.

Figure 5.17: Roman water conduct found on a contruction site from ~ 1.5m underground.

fluorescence lines of lead (72.81keV, 74.97keV, 84.94keV, 87.30keV) resulting from muon interactions in the lead of the detector shielding, which cannot be fully suppressed due to a small part at the back of the germanium crystal which is uncovered by copper and due to a reduced efficiency of the muon-veto. Furthermore, the annihilation line at 511keV can be seen which is present in every germanium detector measurement.

On the basis of these measurements the ultrapure copper measured was utilized for the fabrication of both, the 4π detector holder and the internal shielding (see section 5.3). The originally dicussed use of a Roman lead shielding inside the 4π detector holder was abandoned since the low-energy fluorescence lines at 10.55 keV and 10.45 keV of lead are too close to the 10.37keV signature of ^{71}Ge. The lead from PLOMBUM was used for the internal shielding since its ^{210}Pb activity is comparably low, furthermore the copper plates segmenting the lead as well as the 4π copper detector holder itself efficiently absorb the residual radiation of 46.5keV.
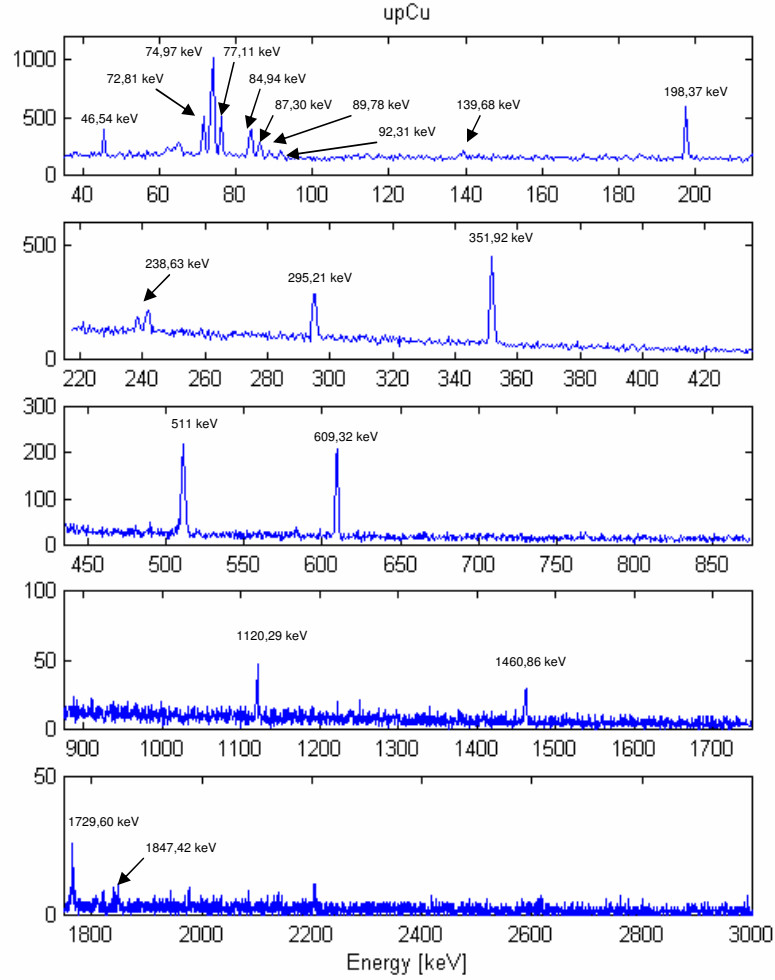
Figure 5.18: Spectrum of an ultrapure copper sample recorded over a period of two weeks, with no cleaning procedure applied. The energies of the background lines are given; for further information on the nature of these contributions see [95].
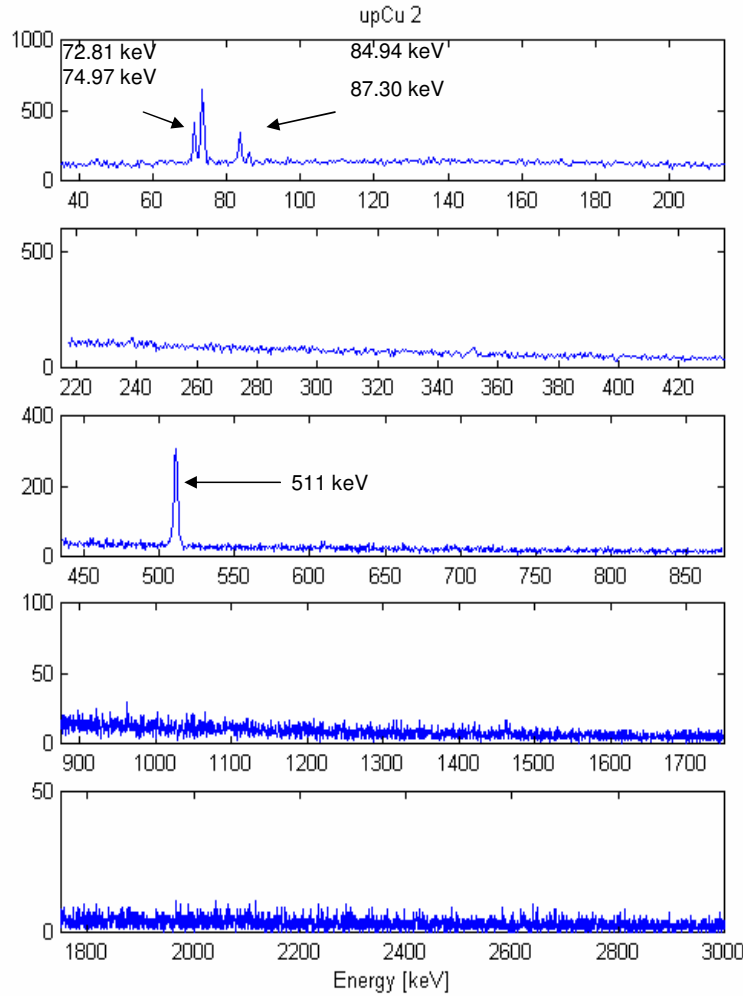
Figure 5.19: Spectrum of the ultrapure copper sample depicted in figure 5.18 recorded over a period of two weeks, after the application of surface etching with HNO_3 at 60°C for 10min. Apart from muon-induced Pb fluorescence lines at 72.81keV, 74.97keV, 84.94keV and 87.30keV and the positron-electron annihilation line at 511keV, no further background contributions are visible.

Chapter 6

Thermal Deposition of Germane Gas onto a Sapphire Substrate

To measure the decay of ^{71}Ge which was produced by solar neutrinos or by neutron activation in a reactor [32] with our cryogenic detector, germane gas (GeH$_4$) has to be thermally deposited onto an absorber, which in this case is sapphire (Al$_2$O$_3$). In analogy to the evaporated iridium-gold film, the germanium layer must be deposited in such a way that good thermal contact with the absorber substrate is guaranteed. In order to gain experience for the procedure and to demonstrate its feasiblity, a test deposition system was installed in Garching and is described in detail in [90] and [32]. The efficiency of the overall system could be increased to almost 100%, which is an important prerequisite if cryogenic detectors are to be implemented in GNO, where the efficiency has to be at least 95%.

The chemical vapour deposition (=CVD) GeH$_4\rightarrow$ Ge + H$_2$ occurs at temperatures $\geq$ 280°C and is performed according to the following steps:

- GeH$_4$ is synthesized in a chemical reaction where GeO$_2$ and NaBH$_4$ have been mixed. The reaction occurs at a temperature of $\sim$90°C.

- The gas is then moved stepwise through the system, which is shown schematically in figure 6.1.

- The deposition system is constantly purged with helium gas which acts on the one hand as a carrier for GeH$_4$ and on the other hand as a flushing medium for the overall apparatus prior to the CVD.
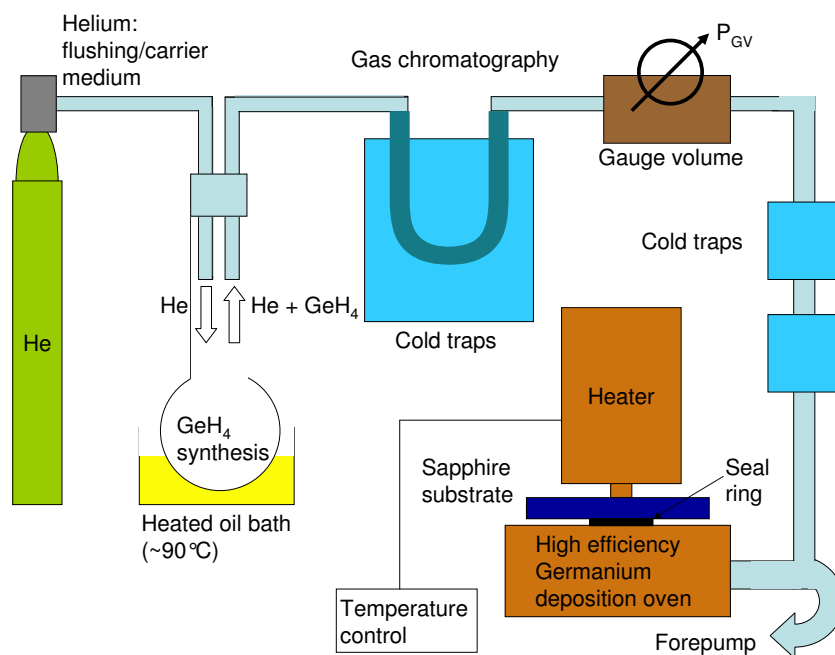
Figure 6.1: Schematic drawing of the germanium deposition system

- The first cold trap through which the germane gas is passed, is at a temperature of -50°C (the temperature is created by mixing aceton and liquid N_2) in order to freeze out water.

- Cold traps, ranging from -196°C (liquid nitrogen) to 0°C (ice water, or again aceton mixed with liquid nitrogen), are used to freeze out GeH_4 at certain points in the system to collect it there efficiently, and offer also the possibility to operate them as 'cryopumps' within the system.

- Gas chromatography is used for purification of the germane gas prior to its introduction into a gauge volume (=recipient of defined volume), in order to determine the exact amount of germane gas.

- The deposition itself is realized at temperatures of $\sim$400°C in the 'deposition oven', where a copper stamp heats the substrate on one side to produce - due to the favourable thermal properties of sapphire - a hot surface on the opposite side to which the germanium can stick easily. It is the geometry of this device that mainly determines the efficiency of the germanium vapour deposition onto the substrate [90]. The thermal deposition lasts for $\sim$3h.

The CVD of germane gas is described in full detail in [90] and [32].

Chapter 7

Results of Measurements with Composite Detectors in the Underground Laboratory in Garching

7.1 Experimental Setup

The underground laboratory (UGL) in Garching is located in the former 'Flugzeittunnel' of the accelerator laboratory and has a shielding of 15 meter water equivalent (= m.w.e.) corresponding to an earth overburden of ∼5m. This underground facility has also been equipped with a ∼2m deep pit designed for the implacement of a cryostat for low-level measurements, especially for feasibility studies concerning the use of cryogenic detectors in the solar neutrino gallium experiment GNO. The setup of an OXFORD KELVINOX 100 cryostat has now been completed after many steps of optimization, described in the following sections. The experimental setup of this cryostat now has the potential to test cryogenic detectors for various kinds of applications from neutrinoless double beta decay measurements, e.g. with ^{150}Nd, to high energy resolution TESs for various applications in the X-ray and γ-energy range, but also for measurements under low background conditions as is, e.g., the case for the CRESST experiment. A well designed internal and external shielding as well as a muon-veto [32] that can be operated in anticoincidence with the cryogenic detector inside of it, also allows to perform important tests and development of experimental equipment for an eventual use in an ultralow background laboratory, for instance in the Gran Sasso tunnel (3600m.w.e.). The setup, as well as the first measure-

94

ments including longterm campaigns to test the feasibility of cryo-GNO, are presented. Figure 7.1 shows a picture of the experimental setup around the cryostat. The gas handling system, as well as the electronic rack and the data acquisition system (DAQ) can be seen in the picture. The cryostat, surrounded by the muon-veto and the lead shielding is located in a pit in the corner of the laboratory and cannot be recognized on this picture, the dashed arrow, however, shows the implacement.

7.1.1   The Cryostat

The KELVINOX 100 (Fa. Oxford Instruments) is a cryostat of the ^{3}He/^{4}He dilution refrigerator type. It has a cooling power of 140μW (at 100mK) and reaches a base temperature of 6.6mK with no thermal load attached to the mixing chamber plate. The addition of internal shieldings and new detector holders has led to a best base temperature of 7.8mK. The creation of these low temperatures allows not only measurements with iridium-gold TES based detectors commonly operated in the 20-100mK range, but also with superconducting tungsten monolayers, as used in the CRESST experiment, which need at least 10mK of base temperature for stable performance.

Figure 7.2 shows a schematic drawing of the final setup of the UGL cryostat KELVINOX 100. The cryostat is located in a 2m deep pit and surrounded by a lead shielding of 10-15cm thickness. For muon anticoincident measurements, the cryostat is equipped with a muon-veto consisting of 15 plastic scintillator panels placed around and on top of the lead shielding. The setup offers also the possibility to insert a γ-source in a channel between the cryostat and the lead shielding to allow calibration of the detectors inside the cryostat. After the calibration is finished, the source can be removed to avoid unwanted activity around the cryostat and the lead shielding as well as the muon-veto is closed. Thus, conditions are created for low-background measurements.

Our cryostat is equipped with a comfortable gas handling unit that can be read-out and controlled via an interface to a PC. All valves, including needle valves for fine flux regulations of the ^{3}He/^{4}He mixture, are operated electronically from a control panel. In the case of longterm measuring campaigns where only a daily parameter check is necessary, the whole cryostat can be monitored or operated via a remote computer equipped, e.g., with PcAnywhere (Fa. Symantec).

The cooldown of the cryostat is performed in several steps, which are reflected by the itemized list below (some of the steps can be performed in a semi-automated mode):

- Pumping of the inner vacuum chamber (IVC): 5x10^{-5}mbar

- Nitrogen cooldown, T=77K
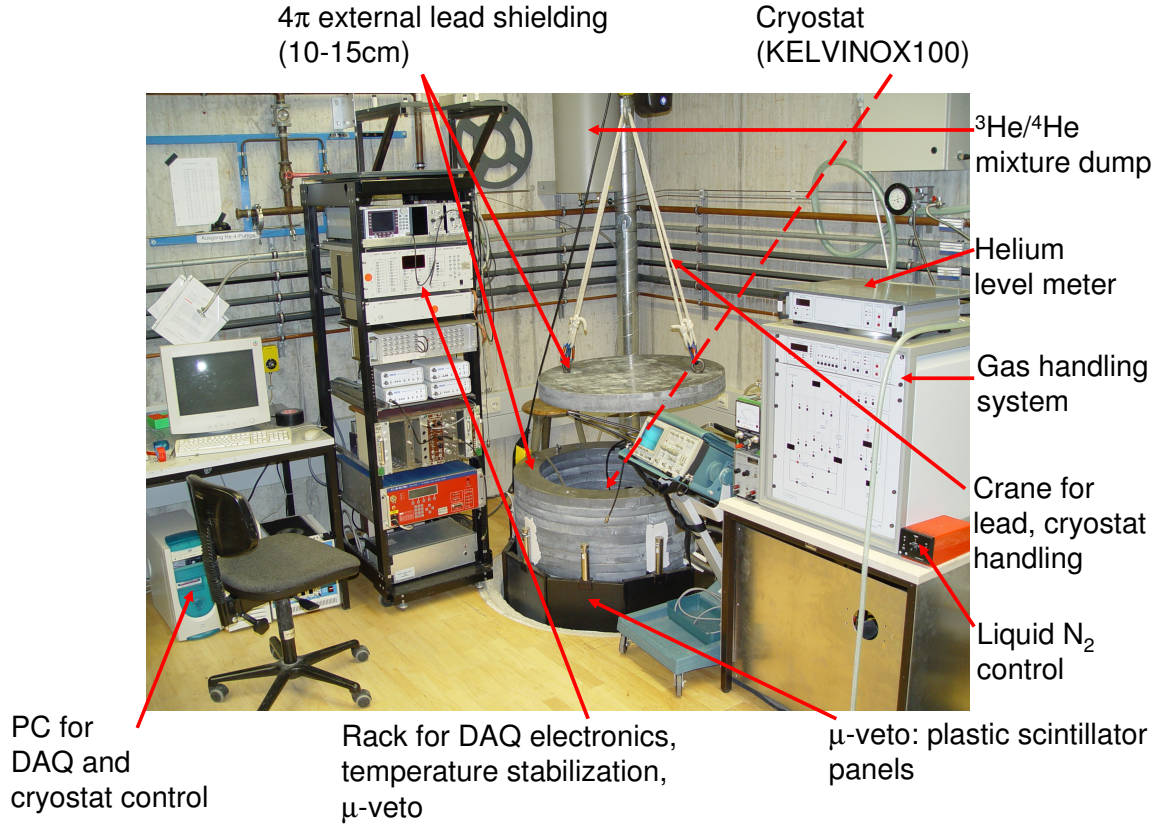
Figure 7.1: Experimental setup around the ^{3}He/^{4}He dilution refrigerator in the underground laboratory in Garching (15m.w.e.). Gas handling system for the cryostat, electronic rack and DAQ are placed around the lead-shielded cryostat. Between the lead shielding and the walls of the circular pit a muon veto, consisting of plastic scintillator panels can be seen. The lead shielding can also be closed on top with two cylindrical lead plates (thickness: 2x5cm). Also the muon-veto can be closed on top by six additional scintillator panels above the two lead plates.

- Helium cooldown, T=4.2K

- Helium pumping at 1K-pot, T∼1.6K

- 'condense in' procedure: ^{3}He/^{4}He gas mixture is introduced via 2 cold traps, one at 77K (liquid N$_2$) and one at 4.2K (liquid helium), into the closed circulation loop and condensed in the mixing chamber (it is advantageous to start this procedure by manual regulation and to leave it operated by a PC routine).

- 'circulation': the circulation of the condensed 2-phase ^{3}He/^{4}He mixture is gradually augmented by opening a needle valve; also this procedure can be performed in a semi-automated way.

- The time required to perform a cooldown from room temperature to ∼10mK severely depends on the thermal load attached to the mixing chamber plate. It varies from ∼12h to ∼48h.

- Once the cryostat has reached its base temperature of ∼10mK it can be operated continuously apart from liquid helium refills which are necessary every ∼5 days. Longest operating time up to now: 45 days in a row.

For details of cryogenic cooling techniques and a variety of applications refer to [91], [92], [93].

7.1.2 Electronics

The electronics required to operate cryogenic detectors can be divided into two categories: 1) Temperature measurement and stabilization, 2) SQUID read-out of the TES. A detailed description of this setup is given in [32]. Figures 7.3a and 7.3b illustrate the electronic setup realized inside and outside the cryostat. Since the cryogenic detector must be kept at a constant temperature level during operation, a fine-tunable resistance bridge along with a heater control (PID) is necessary. Once a suitable working point is found for the detector, the resistance bridge is constantly measuring the actual temperature and comparing it to the set value of a calibrated speer or RuO$_2$ resistor. The difference between the two values determines the amount of power transmitted to the heater. Another application of the resistance bridge is the progressive scanning of the transition curve R(T) of the TES, where the temperature of the heat bath (detector holder) is gradually augmented or decreased while the resistance of the TES is recorded (examples of such transition curves are given in the sections 3.2 and 8.3.

Muon veto,
15 plastic scintillator
panels

Cryostat insert

Cryostat dewar (OVC)

External lead shielding,
thickness: 15cm
at the upper part: 10cm

Liquid helium

Channel for external
γ-sources

Electrical contactation
ports

Helium pumping
lines

Internal shielding:

Sintimid
Cu   5mm
Pb   23mm
Cu   5mm
Pb   23mm
Cu   10mm
Sintimid

Detector
holder

Inner vacuum
chamber (IVC)

³He/⁴He mixing
chamber (~10mK)
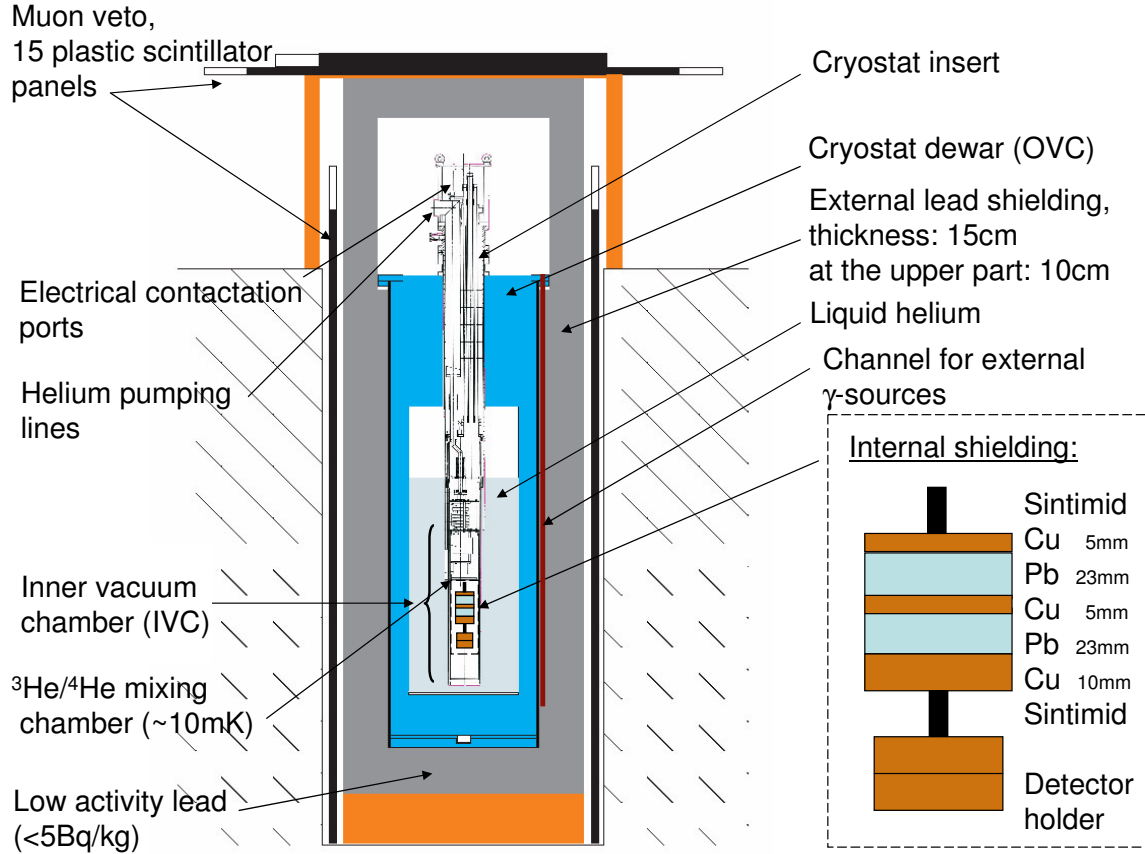
Low activity lead
(<5Bq/kg)

Figure 7.2: Experimental setup of the cryostat (KELVINOX 100, Fa. Oxford Instruments) in the underground laboratory in Garching (15m.w.e.). The cryostat is located in a 2m deep pit and surrounded by a lead shielding of 10-15cm thickness. The cryostat is equipped with a muon-veto consisting of 15 plastic scintillator panels placed around and on top of the lead shielding. The setup offers also the possibility to insert γ-sources between the cryostat and the lead shielding (channel for external γ-sources) to allow calibration of the detectors inside the cryostat. The internal shielding mounted below the mixing chamber, consisting of segmented lead and copper cylinders, as described in section 5.3.2 is also shown in a magnified view on the right. The 4π holder is attached below with a SINTIMID rod.

Temperature stabilization

For the measurements described in this chapter an AVS-47 (Fa. Picowatt, Finland) resistance bridge was used. Figure 7.3a shows the schematic wiring required to achieve temperature stabilization. The temperature sensor, in this case a calibrated RuO_2 resistor glued on top of the 4π detector holder, is first electrically connected via Nb/Ti twisted pair wires to the electrical filtering unit at 4.2K. The low pass filter in use has a cut-off frequency of 80kHz. From there, the wiring is thermally attached to each temperature stage inside the dilution refrigerator to prevent thermal load on the mixing chamber from the wiring at room temperature outside the cryostat. The cryostat is equipped with several 'speer' channels which can be connected individually to the resistance bridge via a distribution box. If required, an additional AVS-47 resistance bridge and PID controler can be introduced e.g., when two detectors are to be operated at the same time, but at different working points.

The heater resistance which is screwed to the 4π holder is also connected to the PID controler via Nb/Ti twisted pair wires, which are again thermally connected to the various stages of the cryostat. The PID heater control unit is connected via an interface to the AVS-47 resistance bridge and can also be computer controlled, e.g. for R(T) measurements.

SQUID read-out and TES biasing

As was already mentioned in section 3.7.2 the TES necessitates a voltage or current biasing. This setup is realized as depicted in figure 7.3b. A constant bias current I_0 is branched according to the ratio of the shunt (R_S) and TES (R_{TES}) resistance values. If a variation of R_{TES} occurs, the resulting change of current induces a magnetic field in the inductivity L which is measured by the SQUID and translated into a voltage signal for further processing. The wiring is again realized with Nb/Ti twisted pair wires, filtered at the 4.2K stage twice by a low pass filter (cut-off frequency at 160kHz).
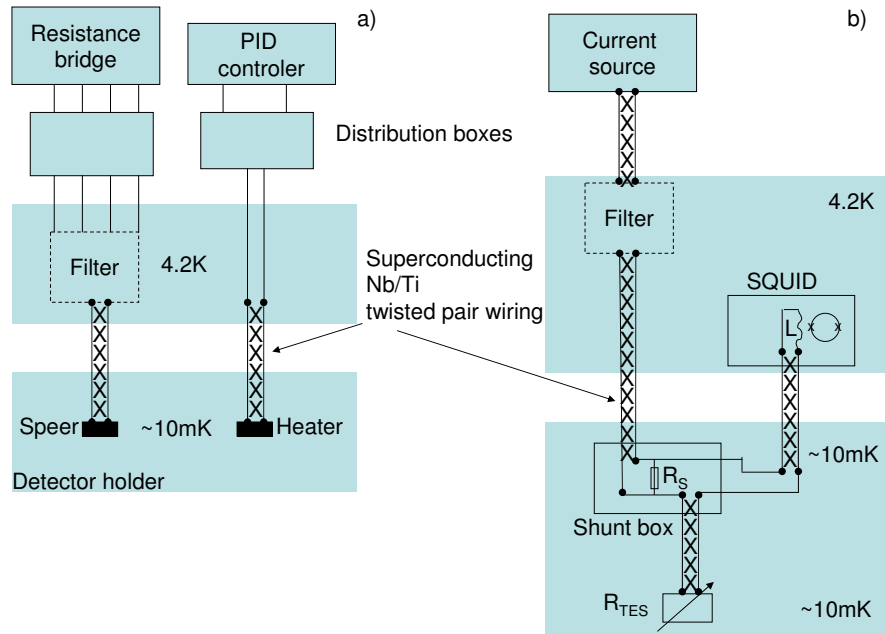
Figure 7.3: a) Electronic setup for temperature stabilization of the cryogenic detector. b) TES biasing and SQUID read-out.

7.2 Background Measurement with Cryogenic Detectors

7.2.1 Background Measurement with a Composite Detector

The same composite detector (Si405c) and setup as described in section 5.2 was used to record the first background spectrum in our underground laboratory in Garching. At the time this measurement was taken, the outer shielding of the cryostat as depicted in figure 7.2 was not yet realized. Only half the height of the cryostat pit (see figure 7.2) was filled with common lead bricks that - compared to Roman lead - still have a high intrinsic ^{210}Pb actvity that cannot be fully absorbed by the relatively thin heat and vacuum shields of the cryostat. Since the working point of the TES was known from prior measurements no ^{55}Fe calibration source, as depicted in figure 5.2, was necessary. Figure 7.4 shows a ∼30h background measurement. Apart from constant background contributions between 0 and ∼230keV, two peaks are clearly visible in the spectrum, one at ∼8keV and one at ∼46keV. The more protuberant peak at ∼8keV is due to muon induced copper fluorescence generated in the close surroundings of the detector as for instance in the copper holder or the radiation shields of the cryostat, also made of copper. The event rate was determined to be 2570cts/d. The relatively bad energy resolution of the Cu K_α line at ∼8keV was due to induced instabilities in the SQUID read-out circuit, which, at that time, was not yet optimized for longterm measurements (see section 7.3). The second peak with an event rate of 247cts/d can be attributed to the 46.5keV γs emitted during the decay of the ^{210}Pb isotope. The background rate between 100 and 200 keV was evaluated to be ∼0.22cts/keV/d. Apart from giving first hints on the nature of the background contributions, the composite detector Si405c was also tested concerning its thermal cyclability and longterm stability.

7.2.2 Background Measurement after Improvement of External Shielding and Activation of μ-Veto

The background measurement described in the previous section was repeated, after three important changes had been made: a) the external shielding had been improved, b) the muon-veto had been activated, and c) this time a 10x20x1mm^3 sapphire substrate had been used with a tungsten TES directly evaporated onto it. Apart from a further background investigation, the motivations for using tungsten monolayer TESs were to test the potential of the cryostat to perform measurements with CRESST detectors in the future
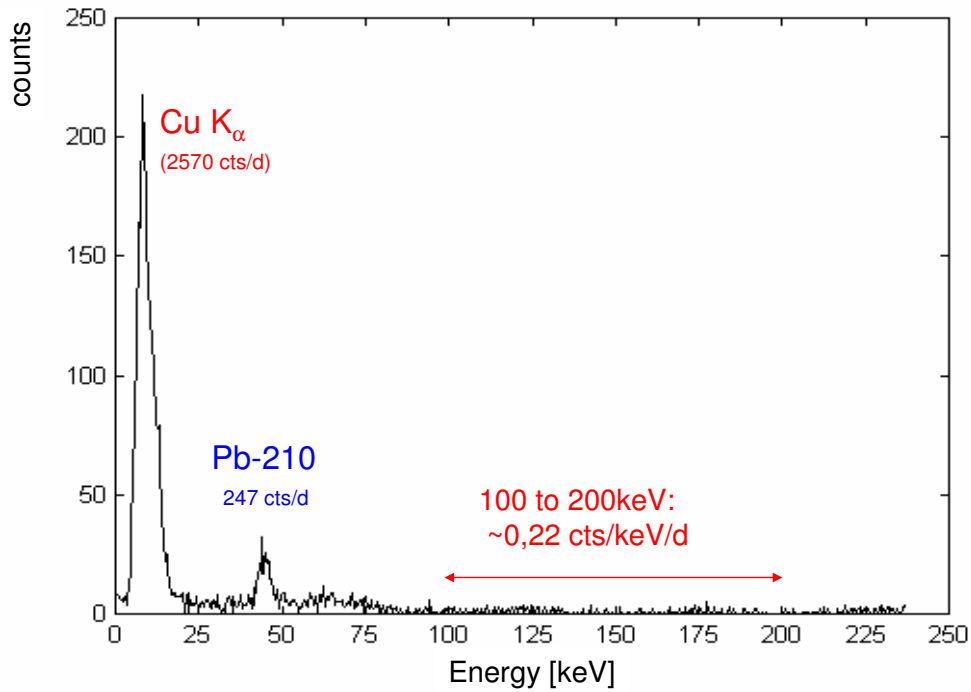
Figure 7.4: First background spectrum recorded with the composite detector si405c (Al_2O_3, 10x20x1mm^3) in the cryostat of the underground laboratory in Garching. Two peaks dominate the background in the energy range between 0 and 50 keV. One at $\sim$8keV with an event rate of 2570cts/d is due to μ-induced Cu K_α fluorescence. The other, smaller peak (247cts/d) is generated by γ-radiation from the intrinsic ^{210}Pb activity of the lead shielding outside the cryostat. A slight bump in the spectrum in the energy region between 60 and 75keV might be due to muon induced fluorescence in the lead of the external shielding.

and to investigate a possible use of tungsten TESs also in GNO.

In order to reject μ-induced background like the copper fluoorescence shown in figure 7.4, a μ-veto was set up around the cryostat. It is described in detail in [32]. Also the external lead bricks filling only half the cryostat pit were replaced by a custom made lead shielding of reduced intrinsic ^{210}Pb activity (Fa. JL Goslar) as illustrated in figure 7.2. From the top to the bottom of the helium dewar the cryostat is shielded by 15cm of lead; the upper part of the cryostat is shielded by 10cm of lead. The volume inside the lead shielding can be flushed with nitrogen to remove radon gas in analogy to the low-level germanium detectors described in section 5.4.1. For calibration or for finding an appropriate working point of the cryogenic detector, an external γ-source can be moved in a channel between the lead shielding and the helium dewar. The source can be moved along the whole cryostat to find the best position for irradiation.
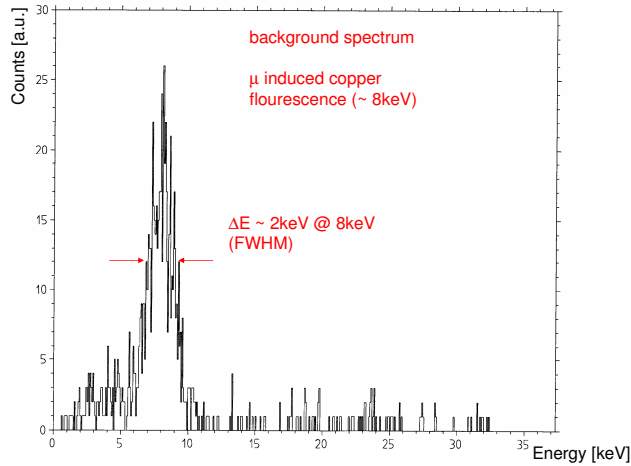

Figure 7.5: Background spectrum recorded over 18h. Apart from continuous background contributions over the whole energy range depicted in this figure, the main contribution is due to muon induced copper fluorescence at $\sim$8keV.

Figure 7.5 shows a background spectrum recorded with one of the two tungsten TES based detectors. The time of measurement was $\sim$18h. This time the spectrum only exhibited one clearly visible peak at $\sim$8keV with an energy resolution of $\sim$2keV (FWHM), the second at 46.5keV was no longer present. For this measurement also the μ-veto was activated. Figure 7.6 is an example of a coincident detector pulse and muon signal; the DAQ is triggered by the detector channel and both the muon and the detector channel
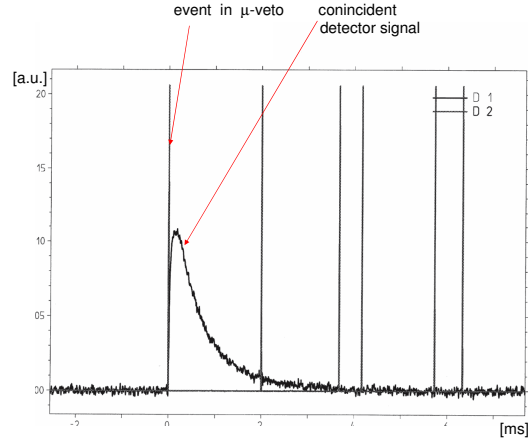
Figure 7.6: Coincident detector pulse and muon event. Events of that kind can be removed from the spectrum after data analysis.
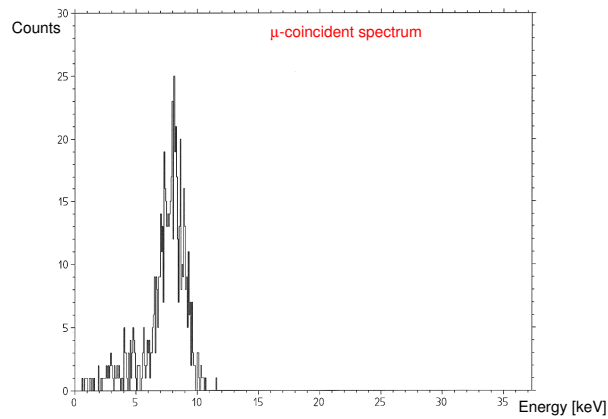

Figure 7.7: Spectrum resulting from coincident events as depicted in figure 7.6. The spectrum is clearly dominated by muon induced copper fluorescence.
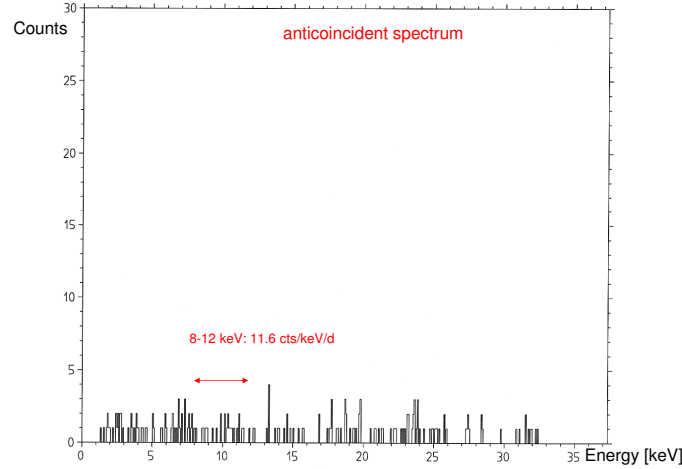
Figure 7.8:   Background spectrum obtained after subtraction of muon coincident events.   The remaining background rate in the energy range between 8 and 12 keV is ∼11.6cts/keV/d .

are recorded simultaneously. During data analysis all coincident events can be flagged, the resulting energy spectrum is shown in figure 7.7. It is clearly visible that the main contribution to the background in the energy window between 1 and 10 keV, is indeed the copper fluorescence peak at 8keV and can be rejected due to the muon-veto. Figure 7.8 shows the energy spectrum after subtraction of muon coincident events. The remaining background in the energy region between 8 and 12keV is ∼11.6cts/keV/d.

7.2.3   Background Measurement after Improvement of Internal Shielding

The same measurement as described in the previous section was performed again, this time with the detectors mounted inside the new 4π holder (see section 5.3). The muon anticoincident energy spectrum shows no relevant peaks. After subtraction of the muon coincident events the obtained energy spectrum looked again like in figure 7.8, only that the background was decreased by a factor of ∼2 to 5.5cts/keV/d in the energy region between 8 and 12keV.

7.3 ^{71}Ge Measurement in 4π Geometry with Two Composite Detectors

In this section results from the first longterm (35d) ^{71}Ge measurement are presented. Following the procedure described in chapter 6, a sample of reactor activated germanium was deposited onto a 10x20x1mm^3 sapphire substrate. Four Ir/Au TESs were produced on a 10x20x0.25mm^3 silicon substrate. Two of the 1x3mm^2 TESs were cut out in our crystal laboratory. The size of the silicon substrate bearing one TES was $\sim$5x7mm^2. Once the sapphire substrate with the ^{71}Ge activity deposited onto it was mounted in the holder depicted in figures 5.9, 5.10, and 5.11, a composite detector was realized by glueing the silicon substrate with the TES onto the sapphire substrate; this detector is called T2. The opposite detector, with which the 4π efficient detection geometry is realized, was produced in analogy to T2 also using the glueing technique: a second 1x3mm^2 TES on a $\sim$5x7x0.25mm^3 silicon substrate was glued to another 10x20x1mm^3 sapphire substrate; this detector is called T1.

Both detectors were bonded inside the 4π holder. Each contactation, i.e. 2 electrical contacts (25μm Al wire) and 1 thermal contact (25μm Au wire) was realized twice for redundancy reasons. Both halves of the detector holder were closed and screwed tightly. In order to realize a temperature stabilization as described in section 7.1.2 a RuO$_2$ resistor was glued to the top half of the 4π holder as a temperature sensor and a heater was screwed outside to the lower part of the holder. The closed holder was taken to the underground laboratory and mounted in the cryostat as depicted in figures 5.12 and 7.2. Due to the thermal load caused by the internal Cu/Pb shielding (see figure 5.12) the cool down of the cryostat took longer, i.e. $\sim$2d instead of 1d when no additional load is attached to the mixing chamber. However, a base temperature of $\sim$9mK could be reached with no bias current applied to the detectors.

Though both TESs originate from the same evaporation charge and even from the same substrate, the transition temperatures of T1 and T2 from the normal to the superconducting state differed by 11mK. The critical temperature T$_c$ of detector T1 was measured to be 56mK, the transition temperature of T2 was measured as 45mK. In order to find a suitable working point for both detectors a ^{60}Co source was placed outside the cryostat to generate pulses in both detectors. While monitoring the pulses on an oscilloscope and the DAQ system, the temperature of the 4π holder along with the bias currents of T1 and T2 were tuned to obtain good pulses in terms of signal to noise ratio. Since the 4π holder represents the heat bath for both detectors its temperature was finally stabilized at 33mK, whereas the additional heating of T1 and T2 was realized by augmenting the bias current. T1 was biased with 256μA and T2 with 140μA; the difference in bias current

reflects the different critical temperatures of T1 and T2.

Both detectors were then operated for 35 days in a row to measure the decay of ^{71}Ge. This measuring campaign was aimed at recording the decay curve of ^{71}Ge and by this to indicate the feasibility of longterm cryogenic measurements as required for an application in solar neutrino gallium experiments. During the whole time of measurement the base temperature was kept constant at ~10.2mK, the temperature stabilization, as well as the SQUID read-out both working satisfactorily. The only dead time of measurement was inferred by liquid helium refills of the cryostat which induced drifts of the bias current in one of the SQUIDs due to temperature drifts. However, this problem can be overcome by placing the SQUID as well as its wiring at a different position in the cryostat with less temperature variation.

To check the stability of the measurement test pulses were generated every 20s by a function generator and applied to the bias current sources of both detectors T1 and T2. Since the response of the SQUID signal depends on the ratio of the shunt resistor R_S and the TES resistance R_{TES}, a change in temperature can be recognized by a modification in the form of the testpulses. The determination of the lifetime of the DAQ system from these test pulses is described in detail in [32]. The average value of the life time was 99.1% taking into account the interruptions due to liquid-helium refills of the cryostat (see figure 7.9).

Figure 7.9 shows a plot of pulse height versus the whole measuring time of 35 days. Three lines are clearly visible. They correspond to K-capture and L-capture events (see below). The K-region exhibits a double structure since energy absorption in the germanium layer and the sapphire absorber leads to different pulse height conversions. As discussed below, L-capture events with an energy release of 1.30keV are only absorbed in the germanium layer, therefore these events are represented by a single line. Figure 7.9 demonstrates the superb stability of the pulse height during the whole measuring period of 35 days. The fading of the three lines reflects the decay of ^{71}Ge. From our 35 day measurement the half-life of ^{71}Ge was determined to 11.3±1.5d which is in good agreement with the known value of 11.4d [94]. For more detail see [32]. The interruptions of the plot are due to liquid helium refills of the cryostat; the Kelvinox 100 needed refilling every 4-5 days.

In order to interpret correctly spectra produced by the two detectors forming the 4π efficient detection setup, a detailed knowledge of the decay possibilities of ^{71}Ge is required. Table 7.1 shows the various possible decay channels of ^{71}Ge. The electron capture process can occur in the K, L, and M shells. The dominant decay channel is the K-capture with a probability of 88%. In 41.5% an energy of 10.37keV is taken away by an Auger-electron.
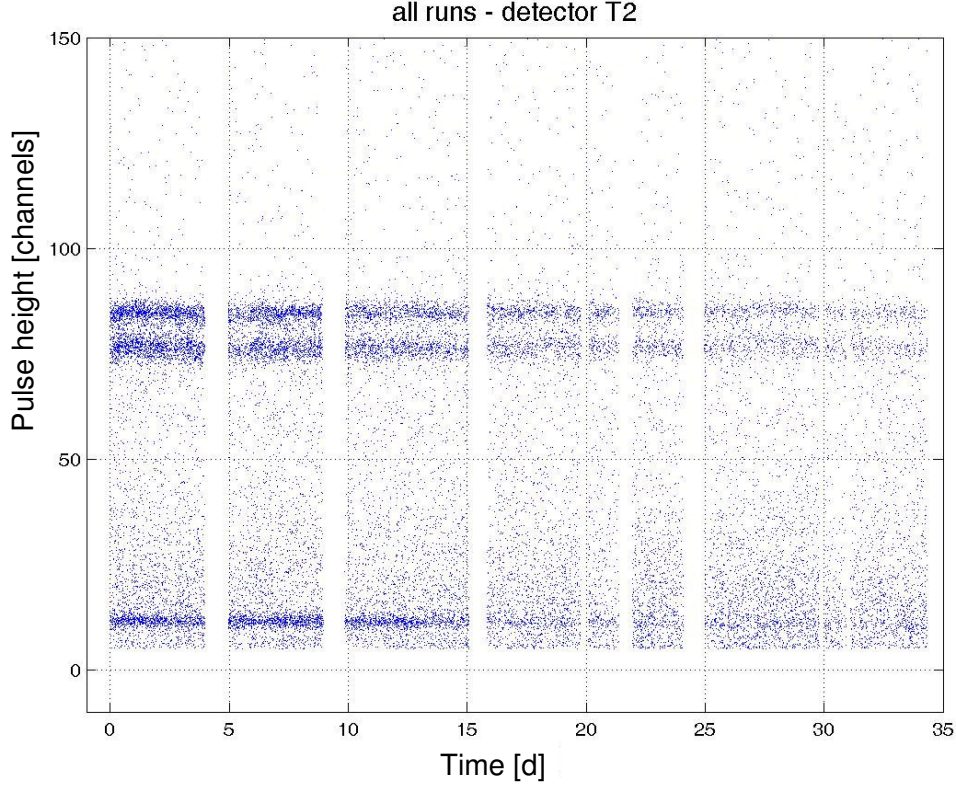
Figure 7.9: Stability of the pulse height of detector T2 (bearing the germanium layer) over the whole measuring time of 35 days. The plot shows K and L-capture events. The K-event region exhibits a double structure due to different pulse height conversions in sapphire and germanium. The fading of the K and L regions indicates the decay of ^{71}Ge. The interruptions in the plot are due to liquid-helium refills of the cryostat.

Capture from	Probability [%]	Emission	Probability [%]	Energy [keV]
K-shell	88	only Auger-e$^-$	41.5	10.37
		Ga-K$_\alpha$ + e$^-$	41.2	9.25 + 1.12
		Ga-K$_\beta$ + e$^-$	5.3	10.26 + 0.11
L-shell	10.3	only Auger-e$^-$	10.3	1.30
M-shell	1.7	only Auger-e$^-$	1.7	0.16

Table 7.1: Decay channels of ^{71}Ge.

7.3 ^{71}Ge Measurement in 4π Geometry with Two Composite Detectors

In 41.2% of the cases the total energy release of 10.37keV is emitted in form of an X-ray photon with an energy of 9.25keV and an Auger-electron with 1.12keV. Only in 5.3% the energy is by a 10.26keV X-ray photon and an Auger-electron with 0.11keV. L and M capture result only in Auger electron emissions with an energy of 1.30keV and 0.16keV, respectively.

The pulse height spectrum depicted in figure 7.10 was recorded with detector T2 (detector bearing the germanium layer). The spectrum shows the complete measurement over 35d. Three peaks are visible, the lower one at ~1.3keV is not only due to L-capture events (1.30keV), but also to Auger-electrons (1.12keV) from the K-capture process (see table 7.1). The energy resolution of 361eV (FWHM), however, was not sufficient to separate these two lines. In principle this separation is feasible (see section 5.2.2, but due to the longterm measuring conditions the energy resolution was pejorated. The energy resolution obtained for the K-capture in germanium is 573eV (FWHM) and 507eV (FWHM) for the K-capture absorption in sapphire.

The energy spectrum of detector T1 (upper detector without germanium layer) depicted in figure 7.11 originates from escape events of the lower detector T2. 9.25keV and 10.26keV X-rays (Ga-K$_\alpha$ and Ga-K$_\beta$) are recorded by detector T1 as well as Auger-electrons emitted from the upper part of the germanium layer which form a continuous distribution to the left of the 9.25keV peak. Since both TESs used for T1 and T2 differed by ~11mK concerning their critical temperature T$_c$, the working point of detector T1 was not ideal and resulted in an energy resolution of 1.45keV (FWHM) at 9.25keV. If both detectors are temperature stabilized individually, this energy resolution can be optimized (see section 5.2.2).

Figure 7.12 shows the 4π-scatterplot obtained when the pulse height of detector T1 is plotted versus the pulse height of detector T2. The complicated structure of the plot can be understood when taking into account the various decay channels of ^{71}Ge shown in table 7.1:

- **K-capture:** according to table 7.1 the K-capture with a probability of 88% is the predominant decay channel. The energy of 10.37keV can be released via a single Auger-electron with 10.37keV, or two combinations of Auger-electron and Ga-K$_\alpha$ or Ga-K$_\beta$ X-rays, respectively. Depending on the location of the decaying ^{71}Ge atom in the germanium layer and the direction of emission of the Auger-electrons, either the total amount of energy can be deposited in the lower detector T2 or a fragment of the energy resides in the germanium and the residual energy of the electron is detected by T1. This fact leads to the band structure of the K-capture region in
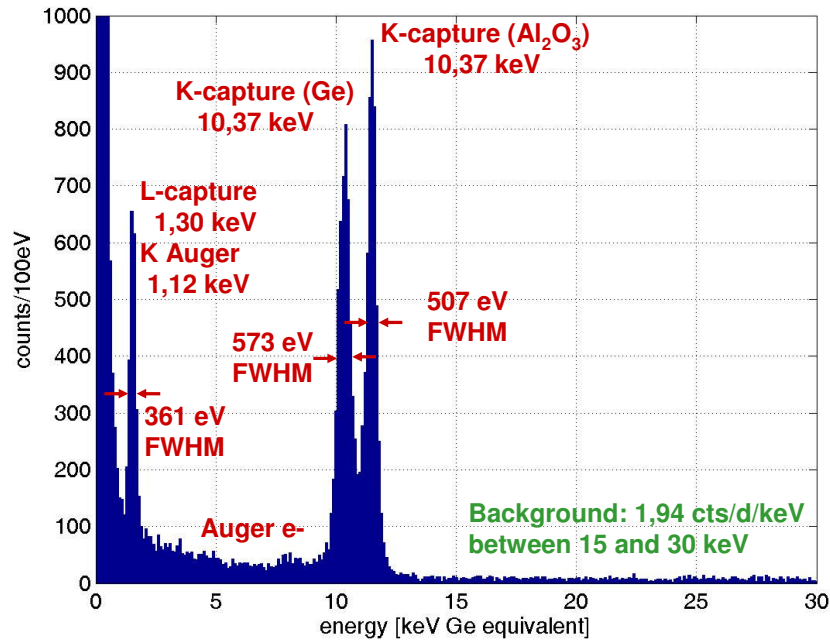
Figure 7.10: Pulse height spectrum of detector T2. The three visible peaks correspond to L and K capture events. The lower peak at ∼1.3keV is due to the full absorption of the released energy after L-capture and to 1.12keV Auger electrons from the K-capture process. The K-capture, with an energy release of 10.37keV produces two peaks which originate from different pulse height conversions if absorbed in sapphire or in the germanium layer itself. The x-axis has been scaled according to the K-capture (10.37keV) in germanium.
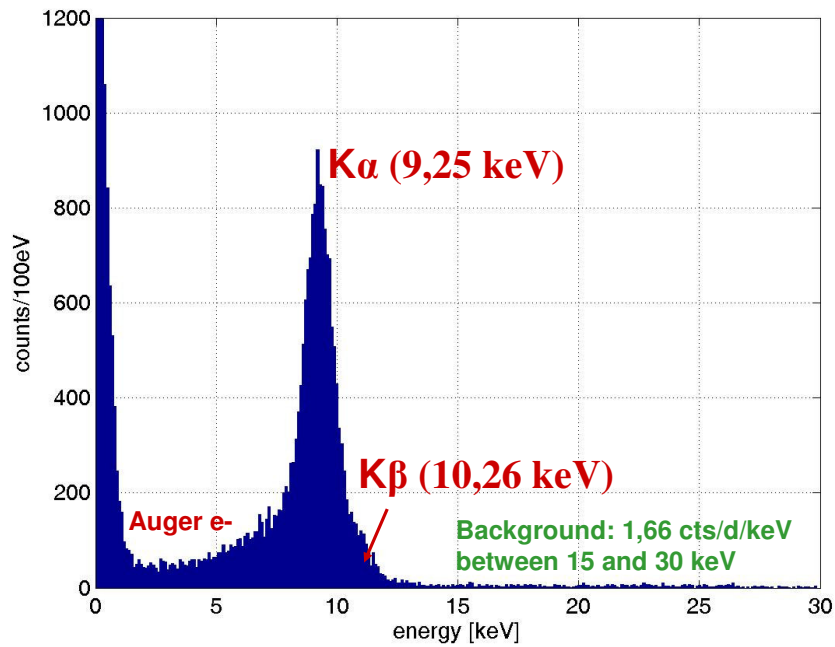
Figure 7.11: Pulse height spectrum of the composite detector T1. The dominant peak at 9.25keV originating from the Ga-K$_\alpha$ X-rays (see table 7.1) could be resolved with an energy resolution of 1.45keV (FWHM). The tailing of the 9.25keV peak to the left is due to Auger-electrons escaping the germanium layer from detector T2. The shoulder on the right-handside of the peak is the unresolved peak originating from the Ga-K$_\beta$ X-rays (10.26keV) emitted from the germanium layer on detector T2.

the plot. Since the K-band is straight and does not exhibit any curvature, it can be deduced that no loss processes occur, the sum energy of 10.37keV always remains the same. The intersection of the K-band on both axes is at 10.37keV.

Events located in the energy window K1 originate from K_β escape events, where the X-ray of 10.26keV is only 'seen' by detector T1. If the total energy release occurs in detector T2 the window K2 contains all events either absorbed in the germanium itself or in the sapphire absorber, which is reflected by a different pulse height conversion. The LK window contains all events where only the K_α X-ray escapes detector T2, whereas the Auger electron is absorbed in the metallic germanium layer on detector T2. The location of this window projected on the x-axis is therefore 1.12keV and 9.25keV if projected on the y-axis.

- **L-capture:** only Auger-electrons with an energy of 1.30keV are emitted. Assuming an average thickness of 5μm for the germanium layer on detector T2 virtually all Auger-electrons are absorbed in the germanium itself leading to all the events located in the window labeled L1. In principle some Auger-electrons could escape from the top part of the germanium layer and deposit part of their energy in the lower and upper detector. This would result in a band parallel to the K-band. However, due to the small number of these events, only events in detector T2 are visible in figure 7.12.

- **M-capture:** only Auger-electrons with an energy of 0.16keV are emitted in this process. The energy threshold of detector T2 was ∼230eV which inhibited the detection of this decay channel; the ensuing loss in efficiency is therefore ∼1.7%. As shown in section 5.2.2 it is principally possible to fabricate composite detectors with an energy threshold of ∼100eV. The resulting detection efficiency is then close to 100%.

In figure 7.12 the windows in green contain rejectable background events. For further details concerning background considerations, see [32].

Figure 7.13 shows the summed pulse height spectrum of detector T1 and T2, where E=E_{T1}+E_{T2}. The spectrum is dominated by the energy resolution of detector T1 that was, as already observable in figure 7.11, not as good as achievable due to the not-so-well suited working point and excess noise in the SQUID read-out. The ratio of K to L-captur events, however, is of 9:1 which corresponds to the expected branching ratio of the ^{71}Ge decay. Due to escape effects and inhomogeneous detector response this feature is for instance not obtainable with miniaturized proportional counters.
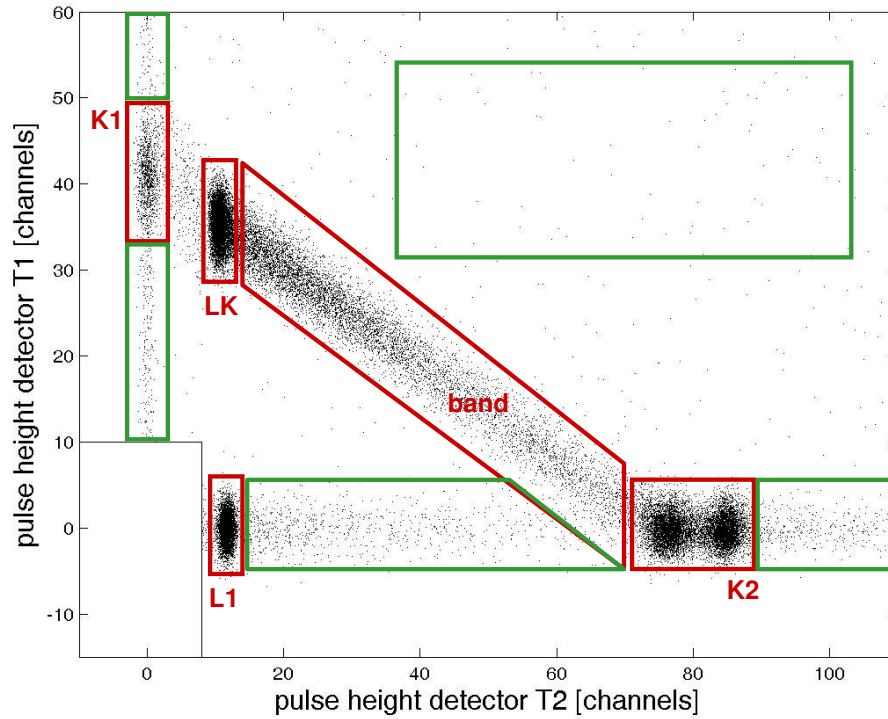
Figure 7.12: Scatterplot of the pulse height of detector T1 over pulse height of detector T2 for the whole measuring time of 35 days. The complex structure of the plot is due to the various decay channels of ^{71}Ge (see table 7.1). The regions corresponding to L and K-capture events are marked. Since the energy threshold of detector T2 ($\sim$230eV) was above 160eV, the M-capture could not be recorded. The signal windows (acceptance windows) are marked in red. The events marked in green are background events and can be rejected. For further details concerning background discussion, see [32].

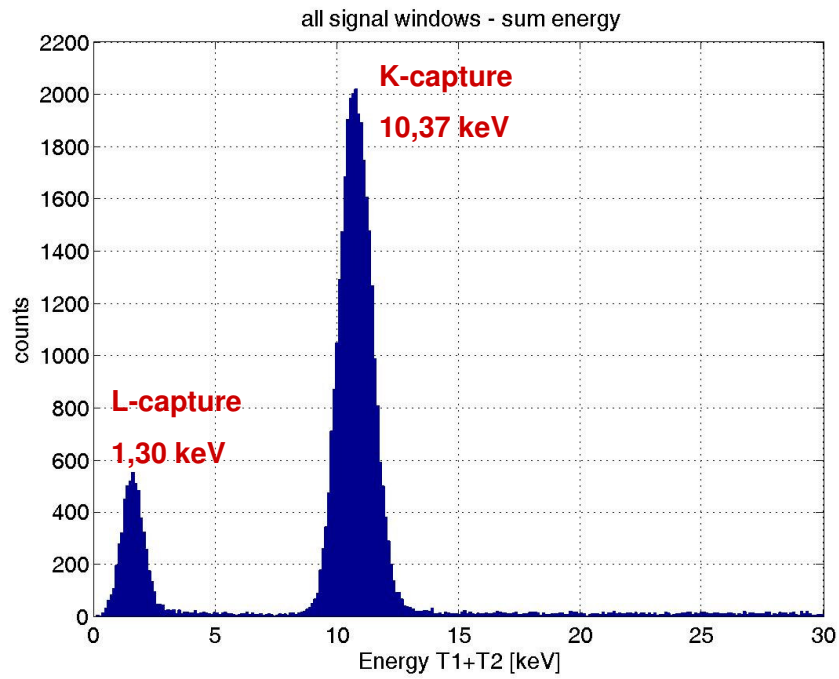Figure 7.13: Summed pulse height (E_{tot}=E_{T1}+E_{T2}) spectrum of detector T1 and T2 over the 35d period of measurement.

7.4 Feasibility Studies for an Alternative 4π-Design Using Roman Lead as Absorber

7.4.1 Motivation

The use of superconducting absorbers with, at the same time, high Z values for efficient energy absorption like lead (Pb, Z=82) is common in the design of high resolution cryogenic detectors, e.g. in the production of superconducting tunnel junctions [96]. As was already pointed out in section 3.3, a superconducting material exhibits only a negligible contribution to the heat capacity. As a consequence, the superconducting absorbers can be increased in size without affecting severely the sensitivity of the detector. Another example for superconducting absorbers are the measurements presented in section 8.3. In this case, a small piece of tin (Sn) foil was used as a superconducting absorber for ^{55}Fe irradiation. Also the neutrino mass measurements performed by the cryogenic groups of Genova and Milano use superconducing rhenium absorbers containing the unstable isotope ^{187}Re [83], [14].

During the development of cryogenic detectors for the solar neutrino gallium experiment GNO, the question arose whether a highly efficient and 4π solid angle detection could also be realized with a single detector, e.g., by introducing the ^{71}Ge activity inside a lead absorber with a TES later glued onto it - in analogy to the first composite detector si405c described in section 5.2. A further point of motivation was that a high performance cryogenic detector with a macroscopic lead absorber offers the potenial for efficient absorption of higher energies especially in γ-radiation measurements as will be discussed in section 8.4. A cryogenic detector exhibiting a combination of high energy resolution and high absorption efficiency for radiation in the MeV range would be an extremely powerful tool for future measurements, not only in astrophysics (see section 8.4), but also for a multitude of other applications in particle physics.

Apart from this first conceptional idea, also the efficient detection of intrinsic radioactive impurities, for example the ^{210}Pb activity, was an issue discussed. The potential of measuring μBq/kg to mBq/kg activities of a given material, e.g. lead, would significate a great improvement in selecting suitable materials, e.g. for upcoming ultra-low background experiments (e.g. EUREKA).

7.4.2   Detector Concept

Figure 7.14 shows the concept for a thermal germane gas deposition (CVD) into a $\sim$5x5x5mm^3 lead absorber. The germane gas (GeH$_4$) would be introduced via a thin crystal tube which has a 90° bend to allow direct optical contact between the lead absorber and a laser beam. If the lead is cooled from outside for instance in a small water or liquid nitrogen cooled copper recipient, the laser can be used to heat the lead only locally ($\sim$1mm^2) to perform a highly efficient germanium deposition (CVD). The schematic drawing on the right in figure 7.14 illustrates the realized composite detector consisting of the lead volume as absorber to which an iridium-gold TES on a silicon substrate is attached.
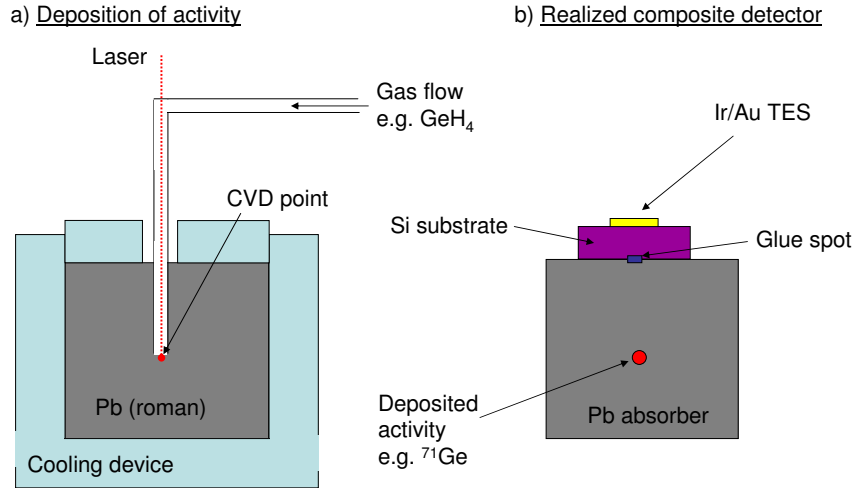
Figure 7.14: Concept and feasibility study to realize one single 4π efficient detector for ^{71}Ge measurements. The left illustration shows how the CVD of Ge could be achieved, the right illustration is the schematic setup of the realized composite detector depicted in figure 7.15.

The realized detector PbSi369c shown in figure 7.15 consisted of a 4x5x7mm^3 polycrystalline Roman lead absorber - which is considered to be of high radioactive purity - and a 5x7x0.25mm^3 silicon substrate bearing a 1x3mm^2 Ir/Au TES. Not only was the

lead absorber large in terms of cryogenic detectors, but also intentionally melted and cut out of a larger block. The idea was to simulate the conditions if such a detector could really be used for ^{71}Ge measurements after the CVD procedure described in figure 7.14a.
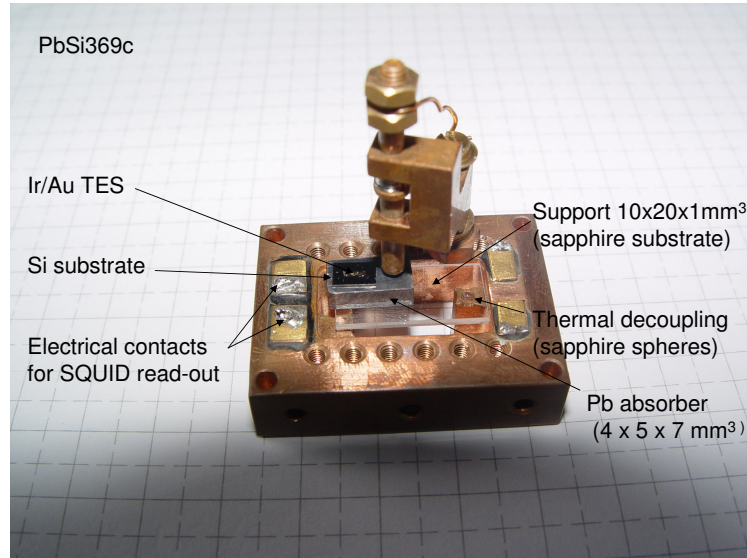
Figure 7.15: Realized composite detector with a 5x7x0.25mm^3 silicon substrate bearing a 1x3mm^2 Ir/Au TES and glued with cryo-resin (EPO-TEK 301-2) to a 4x5x7mm^3 polycrystalline Roman lead absorber. The lead was first melted and then a small block was cut out.

The composite detector PbSi369c was placed on a sapphire substrate, which was itself decoupled by sapphire spheres from the copper holder. After electrical and thermal contactation of the TES the detector was mounted in the cryostat.

7.4.3   Results of Measurements with a Composite Lead Detector

For the irradiation of the detector, a ^{22}Na source was placed outside the cryostat (see figure 7.2). The best position of the source along the cryostat was determined by monitoring the event rate online with an oscilloscope. Once the point with the highest rate was found, the external lead shielding of the cryostat was closed and data acquisition was started

for an ~18h measurement. The obtained energy spectrum, however, was unsatisfactory. Though it exhibited clearly the Compton edge of ^{22}Na at ~1061keV and also an indication for the photo peak at 1275keV the ratio of the intensities of the photo peak and of the Compton edge was not as expected. The intensity of the photo peak at 1275keV was too low with respect to the Compton edge. This behaviour might be explained by the following facts:

- The dynamic range of the detector already biased with a low current of $1\mu A$ was too small to record the full intensity of the photo peak at 1275keV. This could be seen during data analysis where a great number of pulses in the peak region were 'cut' on top due to a surpass of the superconducting transition region of the TES. A limitation of the dynamical range, especially at such high energies, can also result in a non-linear behaviour of the detector.

- The thickness of the lead absorber with respect to the geometrical positioning of the source was not sufficient to fully absorb 1275keV. The absorption efficiency for γ-photons in lead of ~5 to 10mm thickness is roughly 50% [97].

Figure 7.16 shows a plot of pulse height over live time of the measurement. The stepwise changes in the pulse height over live time plot shown in figure 7.16 are due to instabilities which were induced in the SQUID read-out system by the broadcasting stations 'Voice of America' (1091kHz) and 'Bayern1' (801kHz). The unexpectedly bad energy resolution of ~15% at 1275keV of a test spectrum produced out of the part marked 'ROI' in figure 7.16 was probably due to inhomogenities, in the (melted and cut) lead. In addition to that also the continuous instabilities induced by the second radio station broadcasting on 801kHz ('Bayern1') deteriorated further the achievable energy resolution.
Due to an ensuing better grounding scheme involving the cryostat, pumping lines and various electronic devices, this problem has been solved. In particular, for the measurements described in sections 7.2.2, 7.2.3, and 7.3 these instabilities in the SQUID read-out system had already been eliminated and allowed from then on successful longterm measuring campaigns.
As already described in section 5.2.2, plotting pulse height over decay time led to two categories of events (pulse shapes), which could be attributed to events occurring in the silicon and those originating from the lead absorber. Furthermore, it could be shown that this kind of composite detector is principally realizable, but needs, indeed, further investigation for instance using smaller and/or single crystal absorbers.
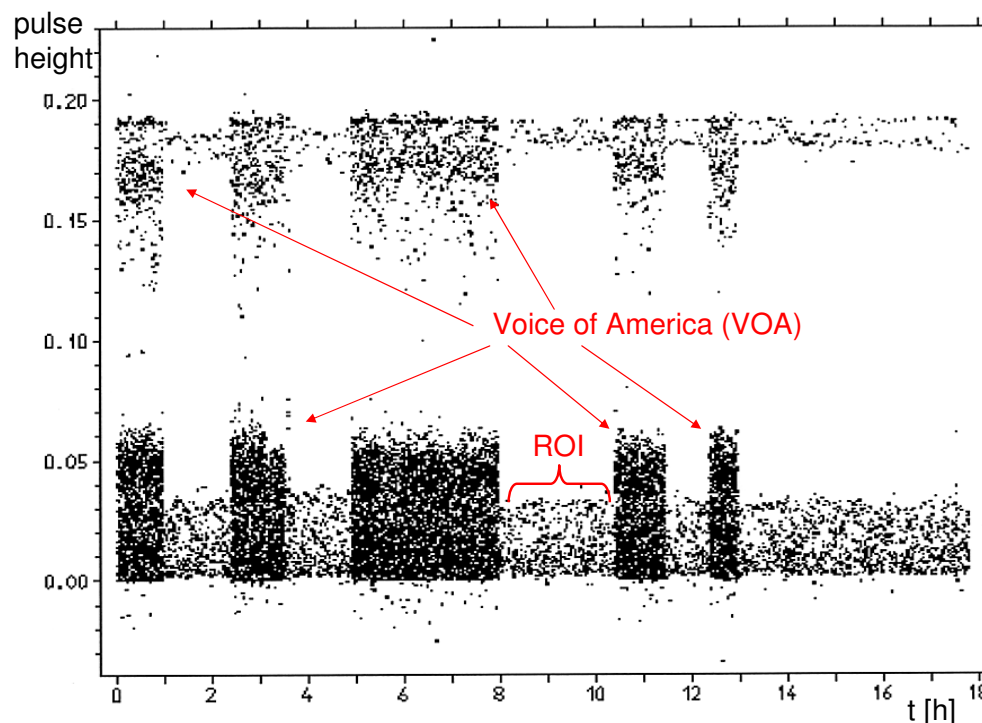
Figure 7.16: Plot of pulse height over live time. The protuberant parts marked VOA reflect instabilities induced by the nearby radio broadcasting station 'Voice of America' (1091kHz). Smaller modulations of the pulse height spectrum are due to another radio station broadcasting permanently on 801kHz ('Bayern1'). This measurement was an important hint for modifications concerning grounding schemes, electrical insulation points in the pumping lines and shielding, as well as the location of various electronic devices present in the laboratory.

Chapter 8

Strive for High Energy Resolution (Microcalorimeters) Using the Technique Developed for Composite Detectors

8.1 Motivation

Looking at recent results obtained with various types of high energy-resolution detectors [98], [96], where energy resolutions between 3.4eV and 12eV at 6keV were reached, one could pose the question whether such performances can also be achieved with iridium-gold TESs. In [99] an example is given where an energy resolution of 6.9eV at $\sim$6keV was measured with a microcalorimeter using a $200x200\mu m^2$ iridium-gold film evaporated onto a SiN membrane and illuminated by synchrotron radiation.

In the case of the cryogenic detectors developed for GNO the energy resolution obtained at 6keV was always $\sim$200eV for a TES evaporated directly onto $10x20x1mm^3$ sapphire substrates as well as for the composite detectors where an additional silicon substrate of $5x7x0.250mm^3$ was glued onto the above mentioned sapphire substrate (see section 5.2 and section 7.3 for details). For that kind of detector aimed at measuring the decay channels of ^{71}Ge (0.16keV, 1.30keV and 10.37keV X-rays and Auger-electrons) the energy resolution is absolutely satisfactory and mainly limited by the size and therefore the heat capacity of the detector system. The important aspects have been the reproducible performance, the redundancy and the longterm stability of each single detector. In addition, in order to produce two TESs to provide the required 4π geometry, it has been

a challenging task to fabricate them eventually exhibiting similar transition temperatures.

In 2004, in collaboration with the cryogenic group of Prof. F. Gatti in Genova/Italy, a large number of iridium-gold TESs were produced in one production step at our institute in Garching. They were fabricated with the intention to investigate their adaptability to a different kind of read-out effectuated in this case with a low-noise transformer, however requiring a matching of the impedances of the transformer input and the TES resistance. Ag/Al based TESs ([83], [100]) like the ones utilized by the Genova group do not exhibit a high enough resistivity prior to their superconducting phase transition. Calculations and experience gained from other TESs produced at our institute seemed promising since our TES sensors have typical resistance values of 1-5Ω in the normal conducting state. This kind of device would allow the read-out of large arrays of detectors on a less expensive scale than the commonly used SQUID read-outs as described in section 3.7.2. The Genova group has been interested in this kind of read-out since one of their main scientific goals has been the measurement of the beta-endpoint spectrum of ^{187}Re for direct neutrino mass measurement (MANU2, see [83] for details). In the MANU2 experiment an array of $\sim$300 detectors, each consisting of a polycrystalline rhenium absorber (0.3x0.3x0.3mm^3), and a TES on a silicon substrate, is foreseen to perform measurements in order to give an upper limit on the neutrino mass in the order of 1eV/c^2. The cryogenic detectors allow to perform a total energy dispersive beta spectroscopy, avoiding complex and model dependent corrections of the impulse dispersive spectra of tritium experiments. To achieve such a good limit, presently only established at <2.2eV/c^2 (95% confidence level) by the Troitsk [101] and Mainz [102] experiments, an excellent energy resolution and longterm stability of the detectors is of the utmost importance.

8.2   Fabrication of μm-sized TESs

In our laboratory in Garching we produced 280 TESs on a 2"-silicon wafer commonly used in the semiconductor industry (see figure 8.1). The prerequisite for the Genova experiment was a transition temperature in the order of 100mK. The individual thicknesses of the iridium-gold bilayer were 200$\mathring{A}$ gold and 1000$\mathring{A}$ iridium (evaporated on a 50$\mathring{A}$ adhesion layer of iridium) where past experience had shown that for this partitioning of the film, a critical temperature of slightly below 90mK should be expected.

After the evaporation onto the silicon wafer in the system described in section 4.1, the

Material	Thickness of layer	Evaporation temperature
Iridium	$50\overset{\circ}{A}$	300°C
Gold	$200\overset{\circ}{A}$	150°C
Iridium	$1000\overset{\circ}{A}$	~25°C

Table 8.1: Parameters used for the evaporation of the iridium-gold bilayer.

Photolithography	
Photoresist	ma-P215
Spinner	1000rpm (30s)
Bake out	100°C (5min)
UV exposure	20s (soft mode)
Developer	ma-D330 (~50s)

Table 8.2: Parameters used for the photolithography of the TESs

substrate was processed photolithographically in the clean room. The difficulty in this case was the extremely small snakelike TES structures in the 5-20μm range (see figure 8.2). Careful attention was given to the shape of the borders of the TES structure: Processing was stopped when the borders were sharply edged. Thereafter the wafer was placed in an argon ion etching plasma, twice for 18min. The reason for this double exposure was the big size of the 2" substrate compared to a relatively small plasma beam of ~30mm of diameter, see figure 8.1 for illustration. In order to cover well the TES structure especially in the middle region where the structures were etched twice, the thickness of the photo resin for photolithography was increased. Details of the evaporation and ensuing photolithographic and sputtering processes can be found in tables 8.1, 8.2 and 8.3.

After termination of the TES production the 2" silicon wafer bearing 280 TESs was taken back to Genova for further processing and measurement. The individual TESs are usually cut out with a sharp knife or a scalpel according to the crystal orientation of the silicon wafer. After that a tin absorber of 0.43x0.43x0.025μm^3 [83] was cut from a poly-

Structurization (plasma etching)	
Argon atmosphere	$3.2\text{x}10^{-4}$mbar
acceleration voltage	650V
ion current	25mA
exposure time	2 x 18min
temperature	water-cooled copper plate

Table 8.3: Parameters used for the structurization of the TESs
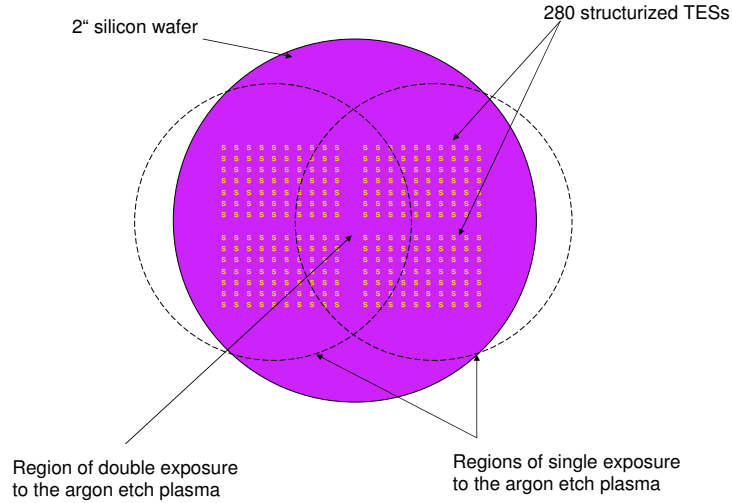
Figure 8.1: 2" silicon wafer bearing four different shapes of TESs (see figure 8.2). Repeated ion etching for 18min each was applied. The resulting overlap of the plasma beam(s) in the middle is illustrated.
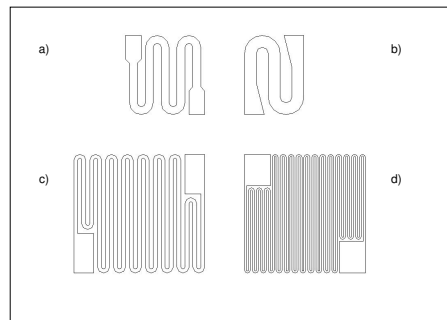
Figure 8.2: TES structures produced on a 2" silicon wafer. Four different patterns were produced by UV-photolithography: (a) length=1.1mm, width=10μm, (b) length=0.7mm, width=30μm, (c) length=5mm, width=10μm, (d) length=7.8mm, width=5μm. The larger surfaces at the extremities of the meander are the areas for bonding, i.e. electrical and thermal contactation.

crystalline foil and glued onto the backside of the remaining piece of silicon onto which the TES had been evaporated. The glue (resin) used by the Genova group is, like in the case of our composite detectors, Epo-Tek 301-2 and applied similarly. After contacting the TES with two aluminium bond wires, the detector is hanging freely being only suspended by its electrical contact wires which act at the same time as a thermal link to the heat bath. This way of contactation is sufficient for the typically small masses used in microcalorimeters. For our cryodetectors of larger mass we always introduce a thermal link to the heat bath via a gold bond wire as described in section 4.4. The microcalorimeter was then mounted along with a weak ^{55}Fe source in a cryostat for measuring. The experimental setup is shown in figure 8.3.

8.3   Results

The structure of the TES used for this experiment is shown in figure 8.2b. The superconducting transition temperature was measured to be 83.2mK and thus exactly in the temperature region required. Figure 8.4 shows the transition curve of one Ir/Au TES. The width of the transition was 0.5mK, i.e., in terms of TESs very steep, resulting usually in high sensitivity. Furthermore, as can be seen by eye, the shape of the curve is very smooth which indicates an excellent film quality. The transition was measured with a bias current of 0.49μA. The normal state resistance was $\sim2.5\Omega$ and the residual resistance in the superconducting state $38m\Omega$. These measurements were performed with a SQUID (Fa. Jena) [83].

The energy spectrum depicted in figure 8.5 was obtained by irradiation of the detector with a weak ^{55}Fe source. An energy resolution of 5.9eV at 5.9keV was obtained [83]. This was so good that the K_α line at 5.9keV could be resolved as $K_{\alpha1}$ and $K_{\alpha2}$. It is, although preliminary, the best result obtained during the development of MANU2 thermal sensors [83]. It is also the best result ever achieved with a temperature sensor fabricated in our laboratory. This energy resolution, if confirmed also with a rhenium absorber would permit to improve the sensitivity to neutrino mass determination to $1eV/c^2$. For comparison: upcoming big experiments for neutrino mass determination like the tritium experiment KATRIN could discover a neutrino mass of $0.35eV/c^2$ with a 5σ significance; a neutrino mass of $0.30eV/c^2$ would be discovered with a 3σ significance [103].
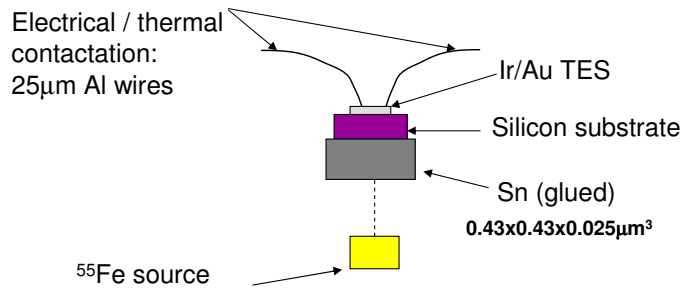
Figure 8.3: Experimental setup of the measurement performed with a tin absorber (0.43x0.43x0.025μm^3) glued to the silicon substrate bearing the iridium-gold TES. The whole detector is only suspended by two 25μm thick aluminium wires, welded onto both extremities of the TES and on the contact pads of the detector holder. The irradiation with an ^{55}Fe source was performed from below illuminating the Sn absorber [83].

.
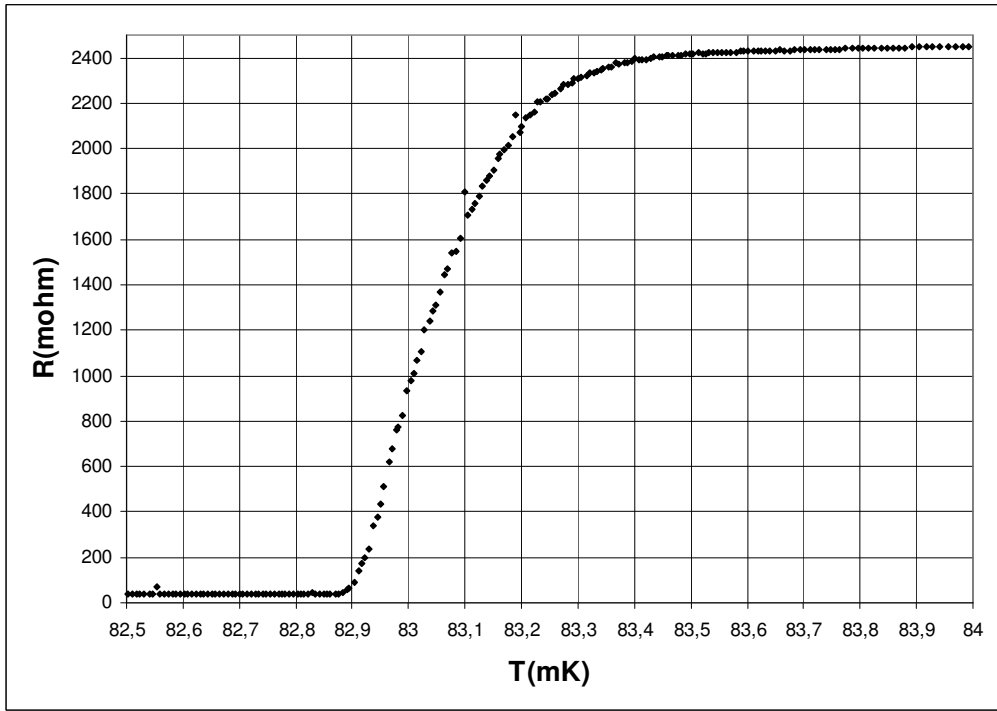
Figure 8.4: Transition curve of one Ir/Au TES for a microcalorimeter measured by the Genova cryogenic group [83]. The transition width for a bias current of 0.49μA is 0.5mK and the superconducting transition temperature is $\sim$83mK. The structure of the TES used for this measurement is depicted in figure 8.2b.

Figure 8.5: Energy spectrum of a ^{55}Fe source used for irradiation of the tin absorber attached to the TES [83].

8.4 Further Conceivable Applications for Iridium-Gold TESs Using the Technique of Composite Detectors

The first results obtained with iridium-gold TESs on a silicon substrate with an attached superconducting absorber (e.g. Sn) look extremely promising and have, most of all, shown that we are able to p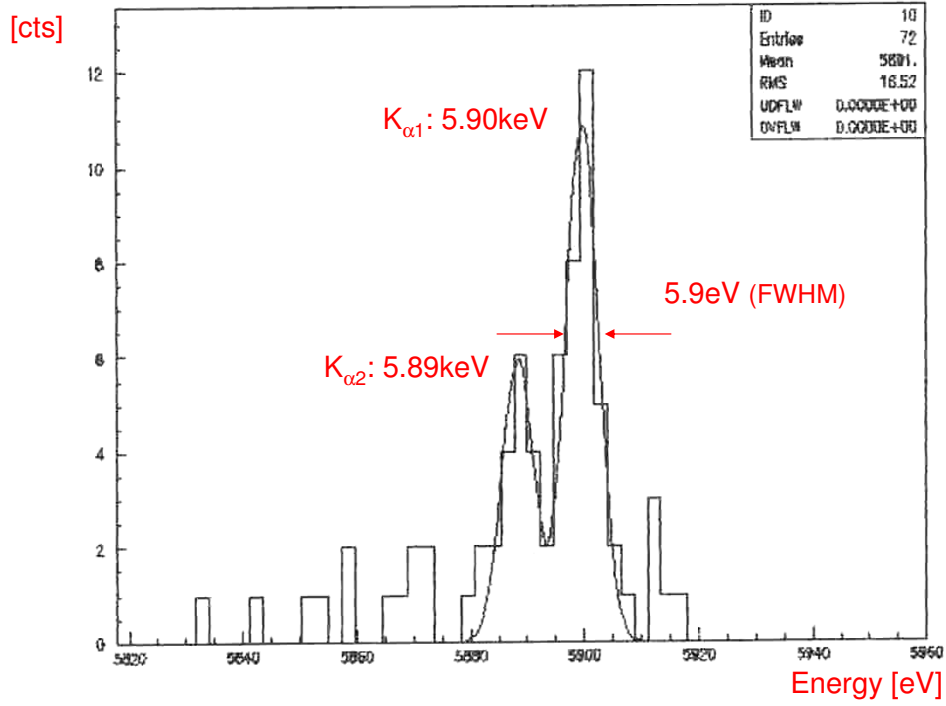roduce TESs in our laboratory in Garching that can compete with the best in the world. Of course, further inquiries have to be performed concerning stability, electronic noise and reproducible production of the iridium-gold proximity layers. In any case, the production of 280 TESs in one single production process could be the key to a successful operation of large-array experiments like MANU2. Not only could this kind of devices serve as neutrino mass detectors, but might also be conceivable for other applications where a large number of high resolution detectors is needed, e.g., for high angular resolution as is for instance the case when observing gamma ray bursts (GRBs). For this kind of detection where a broad energy band in the γ range from 1 to several MeV has to be covered, the use of superconducting lead absorbers for higher absorption efficiency seems a promising and scientifically relevant task.

Apart from the design and production of large array-detectors, such high-resolution TESs could also be utilized for a variety of other applications:

- Each cryogenic detector modul used in the CRESST experiment consists of two detectors. One is a phonon detector, measuring the total energy of a particle interaction with a $CaWO_4$ single crystal; the other is a light detector, measuring the light emitted by this $CaWO_4$ crystal in the same event. Both kind of detectors are operated with TESs. The simultaneous measurement of phonons and scintillation light originating from the $CaWO_4$ crystal due to particle interaction, allows a powerful separation of undesired γ and electron induced background from nuclear recoil events. For a highly efficient background suppression the light detectors have to be extremely sensitive, i.e. the energy threshold should be as low as possible ($\sim$60eV). A possibility to increase the sensitivity is the use of Neganov-Luke amplification [104], [105]. In this context a silicon drift detector (SDD) produced by KETEK [107] was equipped with a TES using the glueing technique as described in 5.2.1. The TES in this case was of the same geometry and size and also from the same evaporation charge like the ones used for the ^{71}Ge longterm measurements described in section 7.3. In this way the SDD acts as a Neganov-Luke amplifier,

whereas the thermal signal is measured by the TES (also produced on a silicon substrate). In this case the advantage of the glueing technique is that the introduction of the TES consisting of iridium and gold does not interfere with the high-purity production process of the SDD itself. A first test of this concept has already been performed and proved the principle to be realizable since pulses from a ^{55}Fe source placed underneath the SDD could be detected in the TES. Ground loops caused by the electrical wiring of the SDD inside the cryostat did not allow to check the gain in sensitivity due to Neganov-Luke amplification of this composite detector, but further tests using this technique will be performed.

- Energy dispersive X-ray spectroscopy (EDS) is a standard technique for element identification in material analysis and especially in the semiconductor industry. The POLARIS spectrometer which has been successfully codesigned by INFINEON, VeriCold and our institute is operated at the failure analysis lab FA5 at Infineon Technologies AG, Munich. Presently, the POLARIS system is equipped with microcalorimeters on membrane substrates which allow good separation of the X-ray lines emitted by the analyzed sample [108]. Still, also in this case the use of a composite detector with e.g. a lead absorber for higher absorption efficiency also at higher energies is conceivable.

- Absolute-activity measurements of low-energy emitting radioisotopes necessitate a highly efficient detection geometry and an excellent energy resolution. An example of such measurements is given in [109] where an ^{55}Fe source was embedded in the gold absorber of a magnetic microcalorimeter [98]. A similar setup with a cryodetector might again be conceivable using a small superconducting lead or tin absorber, where the activity to be measured could be deposited inside the absorber by means of chemical vapour deposition (CVD) as illustrated in section 7.4. Such a detector operated in a cryostat designed for longterm measurements like the setup in our underground laboratory in Garching would also allow the measurement of low-activity sources.

Chapter 9

Conclusions

The main focus of this thesis was the realization of a cryogenic detection concept for radiochemical solar neutrino experiments like GNO and SAGE which use gallium as target material. Gallium experiments measure the capture rate of electron neutrinos on ^{71}Ga nuclei via the reaction ^{71}Ga + $\nu_e \rightarrow ^{71}$Ge + e$^-$. ^{71}Ge is unstable and decays back to ^{71}Ga (half-life: 11.43d). A highly efficient and highly resolved detection of the ^{71}Ge decay signature consisting of X-rays and Auger-electrons (0.16 to 10.37keV) is required to further improve the sensitivity of gallium experiments essentially. Also in the context of a more precise determination of the electron neutrino capture cross section on ^{71}Ga, using an artificial neutrino source (e.g. ^{37}Ar or ^{51}Cr), highly efficient cryodetectors could enhance the accuracy considerably.

Gallium experiments like GNO and SAGE have been of great importance to obtain insight into a stellar interior and, in particular, they are the only ones capable of probing the predominant low-energy pp-neutrino branch of the solar fusion cycles. Both experiments measured a deficit in the expected total ν_e interaction rate on gallium. The neutrino deficit can now be explained as a consequence of massive neutrinos undergoing flavour transitions, via so-called neutrino oscillations. Data from all solar neutrino experiments combined with data obtained from the reactor neutrino experiment KamLAND favour the large mixing angle solution (LMA) for the parameters θ_{12} and Δm_{12}^2 in the 12-sector of the Pontecorvo-Maki-Nakagawa-Sakata matrix (PMNS). The higher energy part of the solar neutrino spectrum for the LMA solution is distorted in shape by the MSW effect due to ν_e interaction with matter resulting in a further suppression of the expected ν_e flux on earth.

The energy production mechanism in the sun, resulting finally in a fusion of 4 protons into helium, occurs via several sub-cycles: the pp, ^{7}Be, pep, ^{8}B, hep and CNO cycle. Gallium experiments are especially important if pp and ^{7}Be flux are to be separated using informa-

tion provided by other experiments like, e.g., KamLAND, the upcoming BOREXINO [39] or the proposed LENA [44] detector. Gallium measurements have provided up to now the only experimental data from which a limit for the CNO-cycle contribution to the overall energy production in the sun can be derived. The continuation of gallium measurements is also essentially important for further analysis of time dependencies regarding the solar pp-neutrino flux.

The introduction of cryogenic ^{71}Ge detection in gallium experiments necessitated the development of a composite detector concept. Commonly used Ir/Au Transition Edge Sensors (TESs) are destroyed during chemical vapour deposition (at $\sim$400°C) of germane gas (GeH$_4$) onto the sapphire absorber (Al$_2$O$_3$; 10x20x1mm^3) of the cryodetector. The separate fabrication of the TES on a smaller silicon substrate (Si; 5x5x0.25mm^3) and the deposition of the metallic germanium layer containing the ^{71}Ge activity was successfully realized. It was demonstrated that an energy resolution, mainly limited by the size of the dielectric sapphire absorber, of 187eV at 6keV and an energy threshold of 100eV can be reached, thus increasing the detection efficiency due to the detectability of the M-capture process, which was previously not possible with the miniaturized proportional counters utilized in GNO. Concerning a reproducible fabrication of composite detectors a particularly critical issue is the glueing of the two detector components, where the amount and shape of the glue drop (two-component epoxy-resin) plays an important role for the detector's eventual performance.

Since the detection of ^{71}Ge has to be highly efficient, the detection geometry must cover the full (4π) solid angle. This is realized by using the information provided by two individual detectors. Detector A bears the metallic germanium layer containing the ^{71}Ge activity and detector B is placed above. The separation between the two detectors is $\leq$1mm. Thus a detection efficiency close to 100% has been reached, which is only limited by the detector's energy threshold, determining the detectability of the M-capture at 160eV.

To operate this double (4π) detector a special holder had to be designed taking into account aspects like: fast handling, redundancy, shielding capability for creating low background conditions, radiopurity, temperature cyclability from room temperature to $\sim$10mK and longterm stability. In order to reduce the intrinsic radioactive background the selection of materials for the construction of the holder was based on low-level γ-spectroscopy indicating the quality of materials in terms of radiopurity like copper, antique lead, or the sapphire and silicon substrates themselves. The 4π detector housing made from copper with a minimum thickness of 5mm all around the detectors acts also as part of the internal shielding inside a ^{3}He/^{4}He dilution refrigerator. The holder can be attached to a $\sim$70mm thick, segmented copper and lead shielding below the mixing chamber of the

cryostat. Thus the detectors are shielded from radioimpurites originating from the parts of the refrigerator itself.

To investigate the feasibility of cryodetectors for gallium experiments, a ^{3}He/^{4}He dilution refrigerator was set up in the underground laboratory (15m.w.e.) in Garching, which is described in detail in [32]. The cryostat is located in a $\sim$15cm lead shielding which itself is surrounded by a plastic scintillator based muon-veto that can be operated in anticoincidence to the cryodetector. Together with the muon-veto the background rate was lowered to 5.5cts/keV/d in the energy region between 8 and 12keV.

Using this experimental setup and the double (4π) detector of the composite type Al$_2$O$_3$/Si + Ir/Au TES, a successful 35d longterm measurement was performed to prove the feasibility of cryodetectors for gallium experiments by recording the decay curve of ^{71}Ge. The longterm stability of the measurement was excellent. Reduction of excess noise especially in one of the SQUID read-out channels could further improve the obtainable energy threshold.

In addition to the Al$_2$O$_3$/Si-type also different versions of composite detectors have been investigated in this thesis: a silicon substrate (5x7x0.25mm^3) bearing a 1x3mm^2 Ir/Au TES was glued to a macroscopic piece of lead (5x7x4mm^3). First measurements with an external ^{22}Na source (γ-energies: up to 1.27MeV) proved the increased absorption efficiency for high-energy γ-rays, but also showed large local dependences probably due to the size and the polycrystalline nature of the lead. However, future experiments, e.g. with single-crystal lead absorbers might help to overcome this problem. The development in this direction looks very promising.

In a collaborational work with the cryogenic detector group of the INFN (Istituto Nazionale di Fisica Nucleare) Genova (Prof. F. Gatti) a large number (280) of Ir/Au TESs on a 2-inch silicon wafer was produced in one production step at our institute in Garching. The TESs were investigated concerning their potential for implementation in the neutrino mass experiment MANU2, which will be measuring the end-point of the ^{187}Re β-spectrum. First measurements with a composite detector of the microcalorimeter type consisting of a 0.43x0.43x0.25μm^3 Sn absorber and a silicon substrate with the TES were extremely successful. An energy resolution of 5.9eV (FWHM) at 5.9keV was achievd; this result is to the day the best obtained with Ir/Au TESs worldwide. If used in an experiment like MANU2 the neutrino mass sensitivity would be of $\sim$1eV/c^2. This excellent energy resolution of the composite Sn/Si detector also indicates the feasibility of high-resolution cryogenic detectors using other superconducting absorbers with high absorption efficiency such as lead.

Bibliography

[1] W. Pauli: Letter to Tübingen Conference, December 4, 1930, translated by L.M. Brown, Phys. Today 23, Sept. 1978.

[2] F. Reines and C. L. Cowan: *Neutrino Physics*, Phys. Today 10N8 (1957) 12.

[3] F. Reines et al.: *Detection of the Free Anti-Neutrino*, Phys.Rev. 117 (1960) 159.

[4] F. Reines: *The Neutrino: from Poltergeist to Particle*, Nobel Lectures, Physics 1991-1995, World Scientific Publishing Co., Singapore (1997).

[5] C. S. Wu et al.: *Experimental Test of Parity Conservation in Beta Decay*, Phys. Rev. **105** (1957) 1413

[6] M. Goldhaber et al.: *Helicity of Neutrinos*, Phys. Rev. 109 (1958) 1015

[7] J. Steinberger: *Experiments with High-Energy Neutrino Beams*, Nobel Lectures, Physics 1981-1990, World Scientific Publishing Co., Singapore (1993).

[8] K. Kodama et al. [DONUT Collaboration]: *Observation of Tau-Neutrino Interactions*, Phys. Lett. B 504 (2001) 218.

[9] K. Hagiwara et al. [Particle Data Group Collaboration]: *Review of particle physics*, Phys. Rev. D 66 (2002) 010001.

[10] V. M. Lobashev: *Study of the Tritium Beta-Spectrum in Experiment Troitsk Nu-Mass*, Prog. Part. Nucl. Phys. 48 (2002) 123.

[11] K. Eitel: *Direct Neutrino Mass Experiments*, Nucl. Phys. B (Proc. Suppl.) 143 (2005) 197 (see also references contained in the article).

[12] A. Osipowicz et al.: KATRIN: *A next generation tritium beta decay experiment with sub-eV sensitivity for the electron neutrino mass*, hep-ex/0109033.

[13] A. Nucciotti et al.: *How to improve the sensitivity of future neutrino mass experiments with thermal calorimeters*, Nucl. Instr. Meth. A 520 (2004) 148.

[14] M. Sisti et al.: *New limits from the Milano neutrino mass experiment with thermal microcalorimeters*, Nucl. Instr. Meth. A 520 (2004) 126.

[15] S. Hannestad: *Neutrino Mass Bounds from Cosmology*, Nucl. Phys. B (Proc. Suppl.) 145 (2005) 313.

[16] H.V. Klapdor-Kleingrothaus: *First Evidence for Neutrinoless Double Beta Decay - and World Status of Double Beta Experiments*, Eleventh International Workshop on Neutrino Telescopes, Venezia, February 22-25, edited by Milla Baldo Ceolin, Edizioni Papergraf (2005) p.215 (see also references contained in the article).

[17] V. Lazarev, private communication (2005).

[18] H. Bethe and C. Critchfield: *The Formation of Deuterons by Proton Combination*, Phys. Rev. 54 (1938) 248.

[19] H. Bethe: *Energy Production in Stars*, Phys. Rev. 55 (1939) 434.

[20] J. N. Bahcall et al.: *Solar models: Current epoch and time dependences, neutrinos, and helioseismological properties*, Astrophys. J. 555 (2001) 990.

[21] J. N. Bahcall et al.: *New solar opacities, abundances, helioseismology, and neutrino fluxes*, Astrophys. J. 621 (2005) L85.

[22] S. Turck-Chièze et al.: *Surprising Sun*, Phys. Rev. Lett. 93 (2004) 211102.

[23] M. Koshiba: *Observational Neutrino Astrophysics*, Phys. Rept. 220 (1992) 229

[24] J. N. Bahcall and M. H. Pinsonneault: *Solar models with helium and heavy element diffusion*, Rev. Mod. Phys. 67 (1995) 781.

[25] V. N. Gavrin et al.: *Measurement of the solar neutrino capture rate in SAGE*, Nucl. Phys. B (Proc. Suppl.) 118 (2003) 39.

[26] M. Nakahata: *Super-Kamiokande's Solar Neutrino Results*, Nucl. Phys. B (Proc. Suppl.) 143 (2005) 13.

[27] B. Aharmim et al. [SNO Collaboration]: *Electron energy spectra, fluxes, and day-night asymmetries of B-8 solar neutrinos from the 391-day salt phase SNO data set*, submitted to Phys. Rev. C, Feb. 25, 2005.

[28] J. N. Bahcall et al.: *New solar opacities, abundances, helioseismology, and neutrino fluxes*, astro-ph/0412440.

[29] S. Fukuda et al.: *Determination of solar neutrino oscillation parameters using 1496 days of Super-Kamiokande-I data*, Phys. Lett. B 539 (2002) 179.

[30] B. Pontecorvo: *Neutrino experiments and the question of leptonic-charge conservation*, Sov. Phys. JETP 26 (1968) 984.

[31] V. N. Gribov and B. Pontecorvo: *Neutrino astronomy and lepton charge*, Phys. Lett. B 28 (1969) 493.

[32] T. Lachenmaier: *Messungen mit untergrundarmen Tieftemperaturdetektoren zum hocheffizienten Nachweis des ^{71}Ge-Zerfalls*, PhD thesis, TU München, 2005.

[33] L. Wolfenstein: *Neutrino Oscillations in Matter*, Phys. Rev. D 17 (1978) 2369.

[34] S. P. Mikheyev and A. Smirnov: *Resonant Amplification of Neutrino Oscillations in Matter and Solar-Neutrino Spectroscopy*, Nuovo Cimento 9C (1986) 17.

[35] K. Eguchi et al. [KamLAND Collaboration]: *First Results from KamLAND: Evidence for Reactor Anti-Neutrino Disappearance*, Phys. Rev. Lett. 90 (2003) 021802.

[36] S.N. Araki et al. [KamLAND Collaboration]: *Measurement of Neutrino Oscillation with KamLAND: Evidence of Spectral Distortion*, Phys. Rev. Lett. 94 (2005) 081801.

[37] J. W. F. Valle: *Neutrino Oscillations and New Physics*, Nucl. Phys. B (Proc. Suppl.) 145 (2005) 141.

[38] O. G. Miranda et al.: *Are solar neutrino oscillations robust ?*, hep-ph/0406280.

[39] C. Galbiati et al. [BOREXINO collaboration]: *Current Status of the BOREXINO Experiment*, Nucl. Phys. B (Proc. Suppl.) 143 (2005) 21.

[40] T. Nakaya: *K2K Results*, Nucl. Phys. B (Proc. Suppl.) 143 (2005) 96.

[41] S. Brice et al.: *Summary of the Neutrino Oscillation Physics Working Group at NuFact04*, Nucl. Phys. B (Proc. Suppl.) 149 (2005) 111.

[42] K. Kumericki and Ivica Picek: *On Distinguishing Non-Standard Interactions from Radiative Corrections in Neutrino–Electron Scattering*, arXiv:hep-ph/0204072.

[43] S. Schönert: *Low Energy Neutrino Detection and Direct Dark Matter Search*, Proceedings of the International Conference on the Seesaw Mechanism, edited by J. Orloff, S. Lavignac and M. Cribier, World Scientific Publishing Co. Pte. Ltd. (2005) p.195.

[44] L. Oberauer et al.: *A large liquid scintillator detector for low-energy neutrino astronomy*, Nucl. Phys. B (Proc. Suppl.) 138 (2005) 108.

[45] F. Ardellier et al.: *Letter of Intent for Double CHOOZ: a Search for the Mixing Angle* θ_{13}, (2004) http://doublechooz.in2p3.fr/0405032.pdf.

[46] A. Bueno et al. [ICARUS collaboration]: *The ICARUS Project*, Nucl. Phys. B (Proc. Suppl.) 143 (2005) 262.

[47] D. Autiero et al. [OPERA collaboration]: *Status of the OPERA experiment (CNGS1)*, Nucl. Phys. B (Proc. Suppl.) 143 (2005) 257.

[48] K. Hochmuth: *The Angular Distribution of Geoneutrinos and their Detection with LENA*. Diploma Thesis, Technische Universität München (2005).

[49] P. Anselmann et al. [GALLEX Collaboration]: *Solar neutrinos observed by GALLEX at Gran Sasso*, Phys. Lett. B 285 (1992) 376.

[50] P. Anselmann et al. [GALLEX Collaboration]: *GALLEX solar neutrino observations: complete results of GALLEX II*, Phys. Lett. B 357 (1995) 237.

[51] W. Hampel et al. [GALLEX Collaboration]: *GALLEX solar neutrino observations: Results for GALLEX III*, Phys. Lett. B 388 (1996) 384.

[52] W. Hampel et al. [GALLEX Collaboration]: *GALLEX solar neutrino observations: results for GALLEX IV*, Phys. Lett. B 447 (1999) 127.

[53] C. Allende Prieto et al. [GNO collaboration]: *Complete results for five years of GNO solar neutrino observations*, Astrophys. J. 573 (2002) L137.

[54] M. Altmann et al. [GNO Collaboration]: *GNO solar neutrino observations: results for GNOI*, Phys. Lett. B 490 (2000) 16.

[55] J. Bahcall et al.: *Where do we stand with solar neutrino oscillations*, Phys. Rev. D 58 (1998) 096016.

[56] T. Kirsten: *Solar neutrino experiments: results and implications*, Rev. Mod. Phys. 71 (1999) 1213.

[57] V. Berezinsky et al.: *Vacuum oscillations and exess of high energy solar neutrino events observed in Superkamiokande*, Astroparticle Physics 12 (2000) 299.

[58] M. Altmann et al.: *Solar neutrinos*, Rep. Prog. Phys. 64 (2001) 97.

[59] J. N. Bahcall: *Solar Models: An Historical Overview*, Nucl. Phys. B (Proc. Suppl.) 118 (2003) 77.

[60] C. Cattadori: *Results from radiochemical experiments with main emphasis on the gallium ones*, Nucl. Phys. B (Proc. Suppl.) 143 (2005) 3.

[61] J. Bahcall and C. Pena-Garay: *Solar models and solar neutrino oscillations*, New J. Phys. 6 (2004) 63.

[62] G. Alimonti et al. [BOREXINO Collaboration]: *Science and technology of Borexino: a real-time detector for low energy solar neutrinos*, Astropart. Phys. 16 (2002) 205.

[63] B. Cleveland, et al.: *Measurement of the Solar Electron Neutrino Flux with the Homestake Chlorine Detector*, Astrophys. J. 496 (1998) 505.

[64] S. Couvidat et al.: *Solar Seismic Models and the Neutrino Predictions*, Astrophys. J. 599 (2003) 1434.

[65] T. Kirsten [GNO Collaboration]: *Progress in GNO*, Nucl. Phys. B. (Proceed. Suppl.) 118 (2003) 33.

[66] L. Pandola et al.: *Neural network pulse shape analysis for proportional counter events*, Nucl. Instr. Meth. A 522 (2004) 521.

[67] S. Ahmed et al. [SNO Collaboration]: *Measurement of the Total ^8B Active Solar Neutrino Flux at the Sudbury Neutrino Observatory with Enhanced Neutral Current Sensitivity*, Phys. Rev. Lett. 92 (2004) 181301.

[68] J. Bahcall and M. Pinsonneault: *What Do We (Not) Know Theoretically about Solar Neutrino Fluxes?*, Phys. Rev. Lett. 92 (2004) 121301.

[69] P. de Holanda and A. Smirnov: *Homestake result, sterile neutrinos, and low energy solar neutrino experiments*, Phys. Rev. D 69 (2004) 113002.

[70] A. Friedland et al.: *Solar neutrinos as probes of neutrino-matter interactions*, Phys. Lett. B 594 (2004) 347.

[71] A. Junghans et al.: *Precise measurement of the $^7Be(p,\gamma)^8B$ S factor*, Phys. Rev. C 68 (2003) 065803.

[72] A. Formicola et al. [LUNA Collaboration]: *Astrophysical S-factor of $^{14}N(p,\gamma)^{15}O$*, Phys. Lett. B 591 (2004) 61.

[73] T. Araki et al. [KamLAND Collaboration]: *Measurement of Neutrino Oscillations with KamLAND: Evidence of Spectral Distortion*, Phys. Rev. Lett. 94 (2005) 081801.

[74] M. Altmann et al. [GNO Collaboration]: *Complete results for five years of GNO solar neutrino observations*, Phys. Lett. B **616** (2005) 174.

[75] J.E. Ruhl et. al: *Improved Measurement of the Angular Power Spectrum of Temperature Anisotropy in the CMB from Two New Analyses of BOOMERANG Observations*, Ap. J. (2002).

[76] Ch. Kittel: *Einführung in die Festkörperphysik*, (11. Auflage) Oldenburg Verlag München Wien (1996).

[77] F. Pröbst et al.: *Model for Cryogenic Particle Detectors with Superconducting Phase Transition Thermometers*, J. Low Temp. Phys. 100 Nos. 1/2 (1995) 69.

[78] D. T. Chow et al.: *Gamma-ray spectrometers using a bulk Sn absorber coupled to a Mo/Cu multilayer superconducting transition edge sensor*, Nucl. Instr. Meth. A 444 (2000) 196.

[79] M. Kurakado: *Possibility of high resolution detectors using superconducting tunnel junctions*, Nucl. Instr. Meth. 196 (1982) 275

[80] N. R. Werthamer: *Theory of the Superconducting Transition Temperature and Energy Gap Function of Superposed Metal Films*, Phys. Rev. 132 (1963) 2440.

[81] M. Sisti: *CRESST - a Cryogenic Experiment for Dark Matter Search*, PhD thesis, LMU München (1999).

[82] L. Holland: *The Vacuum Deposition of Thin Films*, Chapman and Hall Ltd., London (1956).

[83] L. Gastaldo: *Sviluppo di rivelatori criogenici microcalorimetrici per decadimenti beta a bassa energia (Development of cryogenic detectors for low energy beta decays)*, PhD thesis, Cryogenic Detectors Group, I.N.F.N., Genova, Italy (2004).

[84] S. Wänninger: *Development of Cryogenic Detectors for the Solar Neutrino Experiment GNO*, PhD thesis, TU München (2000).

[85] Manual for Mighty MAK Magnetron Sputtering Cathodes (2001).

[86] S. Pfister, Diploma thesis in preparation, TU München.

[87] G. W. Fraser: *On the nature of superconducting to normal transition in transition edge sensors*, www.src.le.ac.uk/instrumentation/solidstate/TESresistance.pdf (2004).

[88] A.Nucciotti et al.: *The Milano neutrino mass experiment with arrays of AgReO$_4$ microcalorimeters*, American Institute of Physics, AIP Conference Proceedings (Ninth International Workshop on Low Temperature Detectors), Vol. 605 (2002) 453.

[89] J. Höhne: *Strahlungsnachweis mit supraleitenden Iridium Gold Phasenübergangsthermometern*, PhD thesis, TU München (1998).

[90] T. Lachenmaier: *Hocheffiziente Germaniumdeposition auf Kryodetektoren für das Sonnenneutrino-Experiment GNO*, Diploma thesis, TU München (2000).

[91] O.V. Lounasmaa: *Experimental Principles and Methods Below 1 K*, Academic Press, New York (1974).

[92] F. Pobell: *Matter and Methods at Low Temperatures*, Springer-Verlag, Berlin (1992).

[93] Ch. Enss, S. Hunklinger, *Tieftemperaturphysik*, Springer-Verlag, Berlin (2000).

[94] W. Hampel and L.P. Remsberg: *Half-life of ^{71}Ge*, Phys. Rev. C 31 (1985) 677.

[95] R. von Hentig: *Spurenanalyse primordialer Radionuklide für das solare Neutrinoexperiment BOREXINO*, PhD thesis, TU München (1999).

[96] G. Angloher: *Supraleitende Tunneldioden als Detektoren für Röntgenstrahlung*, PhD thesis, TU München (2000).

[97] K. Kleinknecht: *Detektoren für Teilchenstrahlung*, 3. durchges. und erw. Aufl. - Stuttgart, Teubner (1992).

[98] A. Fleischman et al.: *Metallic magnetic calorimeters (MMC): detectors for high-resolution X-ray spectroscopy*, Nucl. Instr. Meth. A 520 (2004) 27.

[99] Y. Kunieda et al.: *Microscopic observation of operating Ir/Au-TES microcalorimeter by low-temperature scanning synchrotron microscopy*, Nucl. Instr. Meth. A 520 (2004) 267.

[100] M. Razeti: *Studio di rivelatori microcalorimetrici per misure di massa di neutrino con sensibilita' dell' eV/c² (Study on microcalorimetric detectors for neutrino mass measurement with sensitivity in the eV/c² range)*, PhD thesis, Genova, Italy (2001).

[101] http://www.inr.troitsk.ru/ trdat/results.html

[102] http://http://www.physik.uni-mainz.de/exakt/neutrino/de_experiment.html#ergebnisse

[103] http://www-ik.fzk.de/katrin/motivation/sensitivity.html

[104] B.Neganov and V.Trofimov, USSR patent no 1037771 (1981); Otkrytia i izobreteniya 146 (1985) 215.

[105] P.N.Luke: *Voltage-assisted calorimetric ionization detector*, J. Appl. Phys. 64 (1988) 6858.

[106] Ch. Isaila et al.: *Scintillation light detectors with Neganov-Luke amplification*, to be published in Nucl. Instr. Meth. A, Proceedings of the 11th international workshop on low temperature detectors (LTD-11), Tkyo, Japan.

[107] KETEK Company, www.ketek.net (2005).

[108] Ch. Hollerith, PhD thesis in preparation, TU München.

[109] M. Loidl et al.: *Feasibility study on absolute activity measurement with metallic magnetic microcalorimeters*, Nucl. Instr. Meth. A 520 (2004) 73.

Danksagung

An dieser Stelle möchte ich mich bei allen bedanken, die mich auf dem Weg meiner Promotion bei E15 geleitet und begleitet haben:

Meinem Doktorvater, Herrn Prof. Franz von Feilitzsch, möchte ich für die Überlassung des vielseitigen Themas meiner Promotionsarbeit und dem damit verbundenen Vertrauen von ganzem Herzen danken. Sein kontinuierliches Interesse am Fortschreiten der Arbeit, wie auch seine motivierende und unermüdliche Art in schwierigen Situationen, haben nicht nur zum Gelingen dieser Arbeit, sondern auch zu meinem eigenen Reifeprozess wesentlich beigetragen.

Herrn Dr. Walter Potzel möchte ich dafür danken, mir den Facettenreichtum der Physik in einer Weise näher gebracht zu haben, die nicht perfekter hätte sein können. Sein Engagement auf vielen Ebenen war bewundernswert, seine Hilfsbereitschaft und Geduld, so auch bei der Durchsicht dieser Arbeit, ohne gleichen. Die Notwendigkeit häufiger und intensiver Diskussionen wurden mir aufgezeigt, wie auch die richtige 'Ziehzeit' von grünem Tee. Nie werde ich unsere zahlreichen Italien- und anderen Konferenzfahrten vergessen, bei denen wir auch ausnahmsweise mal Cappucino genossen. And now guess who's number one ?!

Meinem Kollegen Dr. Tobias Lachenmaier möchte ich für die Jahre der guten Zusammenarbeit an unserem Projekt, wie auch für die außerinstitutlichen Aktivitäten, die nicht zuletzt zum Erwerb von Navigationsfähigkeiten zu Wasser beigetragen haben, danken. Ich hoffe, wir können nun bald auch die Leinen mal gemeinsam auf dem Meer losmachen. Ahoi nach Tübingen und viel Erfolg beim Betakeln und Segeln Deines neuen Schiffes !

Herrn Prof. Eckehart Nolte möchte ich nicht nur für sein immerwährendes Interesse bei Institutsvorträgen, seine wertvollen Ratschläge und Anregungen danken, sondern auch für seinen exemplarischen Lebensmut, den ich niemals vergessen werde. Mit ihm ist nicht nur ein hervorragender und dabei so bescheidener Physiker von uns gegangen, sondern auch ein großartiger Mensch.

Herrn Prof. Lothar Oberauer möchte ich für viele Diskussionen und die Möglichkeit Chemikern und Chemikerinnen Physik in Übungen und Vorlesungen näher bringen zu dürfen danken.

Acknowledgements

Herrn Dipl.-Ing. Eckhard Kellner verdanke ich all mein Wissen, was den Aufbau, die Reparatur und Optimierung von Vakuumanlagen angeht. Seine humorvolle und engagierte Art, wie auch seine profunde Menschenkenntnis sind einzigartig. Ich hoffe, wir werden weiterhin die Möglichkeit zu vielen Kaffee- und Diskussionsrunden haben !

Für die Einführung in die HF Technik, wie auch das Aufspüren von radioinduzierten Störungen mittels 'Voodoo-Zauber' gilt mein ganz besonderer Dank Herrn Dipl.-Ing. Hermann Hagen, da ohne ihn langzeitstabile Messungen im UGL bis heute noch auf sich warten ließen.

Für die hochprofessionelle Erledigung zahlreicher Auf- und Umbauarbeiten, wie auch das Anfertigen zahlreicher Konstrukte, die nicht zuletzt zum Gelingen dieser Arbeit beigetragen haben, möchte ich unserer Werkstattsmannschaft Harald Hess, Erich Seitz und Thomas Richter großen Dank aussprechen.

Mein ganz besonderer Dank gilt unseren beiden Institutssekräterinnen Beatrice van Bellen und Alexandra Füldner. Ohne diese beiden Institutsseelen wären viele Termine nicht eingehalten worden, Dienstreisen vor Antritt schon gescheitert und Telefonrechnungen vielleicht nie bezahlt worden. Ihr seid beide Spitze, und vielen Dank für Eure Nachsicht bei Dingen, die ich 'verbockt' habe !

... und nun zu den Weggefährten

Borexinesen:

Dr. Christian Grieb gilt nicht nur mein Dank für die Zeit der Diplomarbeit und Promotion, sondern auch für die vorangegangenen Studienjahre, die wir gemeinsam erlebt haben und in denen er mir so oft nicht nur ein guter Freund, sondern auch eine grosse Stütze war.
Dr. Christian Lendvai, sowie Dr. Ludwig Niedermeier danke ich für die beispiellose Kameradschaft und Freundschaft, die sich in unserer gemeinsamen Zeit bei E15 eingestellt hat. Auch mein Geburtstagsessen zum 30. mit Euch in Aachen wird mir immer in teurer Erinnerung bleiben !
Bei Frau Dr. Marianne Göger-Neff möchte ich mich für die kompetente Netzwerkbetreuung und die moralische Unterstützung in den letzten Tagen dieser Arbeit danken.
Davide d'Angelo danke ich für das Erlernen des italienischen Kaffeemachens und die Möglichkeit am Gran Sasso in seinem Nachbarzimmer Klavier spielen zu können.

142

Cresstianer:

Der, uns GNOmen artverwandten CRESST-Gruppe, möchte ich für zahlreiche Unterstützungen im Labor, wie auch bei der Datenanalyse danken. Dr. Wolfgang Rau, Dr. Michael Stark, Wolfgang Westphal, Chiara Coppi, Christian Isaila waren immer zu Diskussionen (aber auch zu anderen Schandtaten) bereit. Gerade in der Phase der Fertigstellung dieser Arbeit haben sie mich durch gutes Zureden und zahlreiche Kaffeetassen unterstützt. Jetzt bin ich soweit, dass auch ich Senseo-Kaffe zu schätzen gelernt habe !

Unserem Diplomandenneuzugang Sebastian Pfister möchte ich an dieser Stelle großes Lob für sein selbstständiges und erfolgreiches Arbeiten in der Zeit meines Schreibens aussprechen und ihm für reichliche Kalorienzufuhr für nächtliches Arbeiten in Form von selbstgebackenem Schokoladenkuchen danken. Weiter so (nicht mit dem Kuchen, sondern mit der Diplomarbeit) !

Der LENA Manschaft, Kathrin Hochmut, Teresa Marrodan und Michael Wurm, möchte ich ebenfalls für die gute und extrem kameradschaftliche Atmosphäre danken. Das lässt nur eine Schlussfolgerung zu: wir brauchen ganz ganz viele LENE !

Schliesslich möchte ich meiner Familie und insbesonders meinen Eltern für die vielen Jahre der finanziellen wie moralischen Unterstützung, des Rückhalts und des Vertrauens von tiefstem Herzen danken, ihnen ist diese Arbeit gewidmet.